Quantifying recent thermokarst changes in the Northwest Territories, Canada and Alaska, USA using ArcticDEM

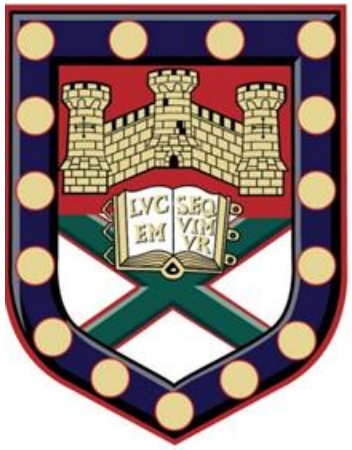

Submitted by Charlotte Alicia Pearson to the University of Exeter as a thesis for the degree of MSc by Research in Geography in May 2020.

Declaration

I certify that all material in this thesis which is not my own work has been identified and that any material that has previously been submitted and approved for the award of a degree by this or any other University has been acknowledged.

Signature: *C. A. Pearson* (Candidate) Date: 15/05/2020

Abstract

Due to Arctic amplification, impacts of surface warming are significantly observed at higher latitudes. Positive feedbacks between periglacial environments and climate have increased thermokarst extent and associated landforms. Subsidence rates depend on active layer sensitivity which controls the geothermal heat balance between the Earth's surface and interior. Carbon release is important, both gradually as the active layer seasonally thaws and deepens, and more notably as abrupt thaw mobilises deep soil organic carbon (SOC). Hillslope processes responsible for abrupt thaw are less well studied using remote sensing due to detection difficulties. Using high-resolution elevation data, this study increases understandings of relationships between topographic settings and climatic forcings by quantifying rates and magnitudes of geomorphic change for features identified within previous studies. Digital elevation model (DEM) differencing techniques are applied to ice wedges at three sites on Garry Island (Canadian High Arctic), where research has historically been limited to in-situ measurement. The aim is to assess the capabilities of ArcticDEM. Results detected rates of vertical change comparable to field studies. Patterns of positive elevation change were explored through hydrological network analysis and snowblow modelling. The differencing method is applied to mass movements (active layer detachment slides (ALDS) and retrogressive thaw slumps (RTS)) at four sites in the Alaskan Brooks Range. Abrupt thaw events on north facing slopes increased in magnitude, with length exhibiting the most significant rate of change in both features. Semi-automated delineation techniques developed using ArcGIS Model Builder, aided the mapping of five previously undetected features and facilitated carbon release estimates. As the Arctic warms, permafrost will continue to thaw, and hillslopes will become more unstable, impacting spatial extents of periglacial landforms. This thesis uses repeat elevation data at high resolutions in a method which could be implemented across the High Arctic to provide contributions to studies of periglacial environments.

Acknowledgments

Special thanks to Professor Christopher Burn of Carleton University whose insight and knowledge into the subject matter provided the inspiration for this research. This input and the opportunity to engage in Arctic fieldwork has provided me with a wealth of experience that brings a unique perspective to the thesis.

I would like to thank the following people from the University of Exeter, without whom it would not have been possible to undertake this research:

I am deeply indebted to my supervisor Dr. Steven Palmer whose dedicated support, unwavering guidance and constructive criticism have been invaluable throughout this project. The wealth of knowledge he imparted in the field of remote sensing is the linchpin of this thesis.

I am extremely grateful to my supervisor Dr. Alastair Graham for his profound belief in my abilities and continuously providing me with encouragement and insightful suggestions, particularly with regards to the geomorphological analysis.

I would also like to extend my deepest gratitude to my supervisor Dr. Anne Le Brocq for guiding me through her Snowblow Model which became an integral part of the analysis of Garry Island.

Thanks also go to Mr David Hein-Griggs for providing technical support and to the CCoRDS Research Group for affording the opportunity to share and discuss aspects of my research.

I would like to say a heartfelt thank you to Dr Oliver Bartlett who went above and beyond his remit in enthusiastically and diligently offering support and assistance throughout the period of research.

Last but by no means least, thank you to the many people who have helped and supported me throughout the research period. Without them, the completion of this thesis would not have been possible.

Table of Contents

List of Figures

List of Tables

List of Equations

List of Appendices

List of Abbreviations

ALDS	Active Layer Detachment Slides
DEM	Digital Elevation Model
GE	Google Earth
ICESat	Ice Cloud and land Elevation Satellite
IW(s)	Ice Wedge(s)
MAGT	Mean Annual Ground Temperature
NWT	Northwest Territories
PCF	Permafrost Carbon Feedback
RTS	Retrogressive Thaw Slumps
SOC	Soil Organic Carbon
SOCC	Soil Organic Carbon Content

Chapter 1

Introduction

1.1. Global Context and Rationale

Arctic temperatures have increased by a magnitude of 5ºC per century and are vulnerable to future warming as Arctic amplification links solar surface warming with snow and ice retreat, creating a positive feedback (Anisimov et al., 2001; Bowden, 2010). Warming has become the focus of much research, with a 75% decrease in Arctic sea ice volume since the 1980s and an increased likelihood of a seasonally ice-free Arctic Ocean by 2050 (Overland et al., 2014). This will result in feedbacks which will cause global temperatures to continue rising as well as economic and ecological impacts (Overland et al., 2014). In addition, there are complex feedbacks between terrestrial ecosystems and environmental conditions which vary in magnitude across Arctic regions as vegetation zones shift, altering levels of productivity and the capacity for carbon storage (Callaghan and Jonasson, 1995). In contrast with temperate environments, circumpolar regions are underlain by relict ground ice preserved within permafrost which can result in waterlogged vegetation as permafrost degrades and precipitation regimes change (Callaghan and Jonasson, 1995; Kokelj et al., 2017).

Interest in permafrost degradation has intensified since the 1980s in concordance with increasing surface temperatures (IPCC, 2013). Indeed ~24% (22.79×10^6 km^2) of the Northern Hemisphere is underlain by near-surface (within the top 1m of soil) permafrost (Figure 1.2; Zhang et al., 1999; Pastick et al., 2015). Of the ~11 million km^2 of permafrost, only 1 million km^2 is expected to remain by 2100 (Lawrence and Slater et al., 2005). The High Arctic, including the Canadian Arctic Islands, Greenland and Svalbard, is defined by ecological shifts and mean summer temperatures below 5ºC (Groendahl et al., 2007; Douglas and Smol, 2010). Across the High Arctic lowlands, near-surface ground ice is vulnerable to rapid degradation (Farquharson et al., 2019). This is due to receiving low levels of thermal buffering whereby the sparse vegetation cover does not sufficiently

buffer the underlying permafrost against warming air temperatures in the way in which thick moss can buffer permafrost at lower latitudes (Walker et al., 2005; Farquharson et al., 2019). This has been observed within cold permafrost in the Canadian High Arctic where active layer (seasonally thawed surface soil layer) thickness is increasing on an annual basis (Hinzman et al., 1991; Farquharson et al., 2019). However, while the greatest thaw subsidence is at high latitudes where soils are thin, the greatest carbon storage is in Arctic tundra soils where the thicker buffer layer slows decomposition (Hobbie et al., 2000). Hence the impact of thaw subsidence and annual soil carbon release can vary in magnitude as a result of temperature, permafrost, substrate quality and biological activity (Hobbie et al., 2000).

Ground ice depth is increasingly in disequilibrium with the climate (Farquharson et al., 2019). As summer temperatures rapidly increase, thawing causes near-surface subsidence which creates an imbalance with the geothermal heat reaching the base of the permafrost (Riseborough, 2007; Farquharson et al., 2019). During the thaw season, precipitation is also an important element which interacts with air temperature to alter moisture conditions (Kokelj et al., 2015). Consequently, as permafrost thaws and active layer thickness increases, subsidence-driven thermokarst landforms become evident as slump soils are destabilised by rainfall (Jorgenson and Osterkamp, 2005; Kokelj et al., 2015). These landforms reflect the changing environmental conditions of the permafrost landscape in terms of hydrological and ecological feedbacks and subsequently alter the geomorphological footprint (Kokelj and Jorgenson, 2013; Kokelj et al., 2017).

The impacts of degrading permafrost at high latitudes hold huge implications for the release of terrestrial organic carbon to the atmosphere since the Arctic permafrost landscape stores ~67% of carbon at the near-surface level (Schuur et al., 2008; Liljedahl et al., 2016). CO_2 release to the atmosphere equals that stored within the land and oceans to create a balanced budget between net sources and carbon sinks (Houghton, 2007). However, analysis of this global carbon budget invariably does not account for the contributions of high latitude reservoirs contained within permafrost (Zimov et al., 2006). As such, regional estimates of this soil organic carbon (SOC) are poorly constrained which impact the prediction of future CO_2 concentrations (Houghton, 2007; Hugelius et al.,

2014). Since permafrost storage at high latitudes is double the atmosphere's capacity, the gradual and catastrophic release of thaw-induced greenhouse gases will become problematic as organic carbon is increasingly exposed to microbial decomposition through activation of the "soil carbon pool" (Lawrence and Slater, 2005: 1; Schuur et al., 2008; Schuur et al., 2015). As plant growth increases with climate warming, response times from vegetation to permafrost warming are estimated to be more rapid than soil carbon pools, leading to soil carbon inputs (Natali et al., 2011; Schaphoff et al., 2013). However, under RCP4.5, the metres of soil impacted by abrupt thaw is predicted to offset processes of carbon uptake by ecosystems from gradual thaw (Turetsky et al., 2020). Beyond 2020, 42-88% of the carbon sink will be cancelled out by effects of the permafrost carbon feedback (PCF) in enhancing respiration rates (Koven et al., 2011; Schaefer et al., 2011).

In the upper 3 metres, thermokarst terrain stores 30% of the total SOC within the region (Olefeldt et al., 2015). However, PCF models often fail to account for abrupt thaw release (Vonk and Gustafsson, 2013). By 2300, one third of carbon losses via abrupt thaw will be due to active layer detachment slides (ALDS), despite these only characterising 3% of the terrain (Turetsky et al., 2020). The consequences of this have been observed within Arctic catchments where SOC derived from permafrost thaw and thermokarst failures has entered adjacent headwater streams and altered biogeochemical processes (Guo et al., 2007). The material is initially mobilised through meltwater pathways, increased snow accumulation within the track zone, and mudflows which collectively increase soil erosion (Lyon et al., 2009; Mithan, 2018). The resultant impact is dammed river channels upstream and the downstream formation of turbidity pools within the surface water, with short peaks associated with sediment fluxes during summer warming and longer term increases as air temperatures continue to warm (Lamoureux and Lafrenière, 2009; Jolivel and Allard, 2017). Along the Toolik River in the Alaskan Foothills, sediment delivered over two years in an adjacent catchment was exceeded by a thermokarst gully investigated in 2003 which delivered 18 times more sediment, despite a catchment 70% of the size (Bowden et al., 2008).

Recent research of the soil carbon pool within permafrost regions has focussed on certain aspects. Hillslope failures are important in terms of their threat to infrastructure and their impact on the terrestrial carbon cycle and sediment budget; reshaping the landscape due to soil movement (Bowden, 2010; Olefeldt et al., 2015). Approximately 17% of continuous permafrost terrain across a 1.27×10^6 km^2 area of northwestern Canada is thaw-slump affected, located in concentric swaths 60-100km-wide which correspond with past locations of the Laurentide Ice Sheet (Figure 2 in Kokelj et al., 2017). The increased frequency of such thermokarst processes under a warming Arctic will result in greater mobilisation of carbon stored within permafrost and organic matter decomposition as underlying permafrost is exposed to warmer summer temperatures (Cory et al., 2013).

1.1.1. Canadian High Arctic

Thermokarst development within the Canadian High Arctic has accelerated in recent years as a result of uncharacteristically warm summers (Farquharson et al., 2019). Between 2003 and 2016, thawing index values ~200% greater than the historical average (1979-2000) resulted in increased rates of subsidence during years with particularly warm summers (e.g. 2007, 2011 and 2012) (Farquharson et al., 2019). During these years, the IPCC RCP4.5 maximum thaw depth projections for 2090 were exceeded (Farquharson et al., 2019). In the western Arctic, ice wedges (IWs) are an abundant geomorphic expression of the impacts of thawing permafrost as the active layer deepens (refer to Chapter 1, Section 1.4.2) (Mackay, 1989; Burn and O'Neill, 2015). This causes the overlying ground to subside and the soil structure to deteriorate due to massive ground ice close to the surface (Burn and O'Neill, 2015; Farquharson et al., 2019).

The permafrost region underlays ~50% of Canada's land area and extends down to a mean annual air isotherm of -1°C to -4°C (Brown, 1970; Senneset et al., 1988). In the continuous permafrost zone, the southern limit is marked by temperatures of -5°C and a permafrost thickness of ~60m, whilst in the north, thickness increases to ~300m at -15°C (Brown, 1970). In the Northwest Territories (NWT), all zones of permafrost are present (refer to Chapter 1, Section 1.2.1), however differing climate, vegetation and geology impact its temperature and thickness (Figure 1.1.a.; Government of the NWT, 2014). Here, the continuous-discontinuous boundary is marked by the transition from subarctic

boreal to tundra vegetation (Government of the NWT, 2014). Measurable warming of permafrost within the western Arctic has occurred since the 1980s, 10 years earlier than those observed within the eastern and high Canadian Arctic regions (Smith et al., 2005; Brown and Romanovksy, 2008). Permafrost most vulnerable to thinning or disappearance is that with ground temperatures closest to 0ºC (above -2ºC) (Hannah et al., 1999; Smith et al., 2005).

Garry Island (study region 1, Chapter 3) typifies these conditions, with modelled mean annual ground temperature (MAGT) at the top of the permafrost (2000-2016) measuring -4ºC to -6ºC (Figure 1.1.b.). Doubling of CO_2 is predicted to cause air temperatures to increase by a maximum of 6ºC by 2050, which would cause 58% of the current permafrost to have positive ground temperatures (Hannah et al., 1999).

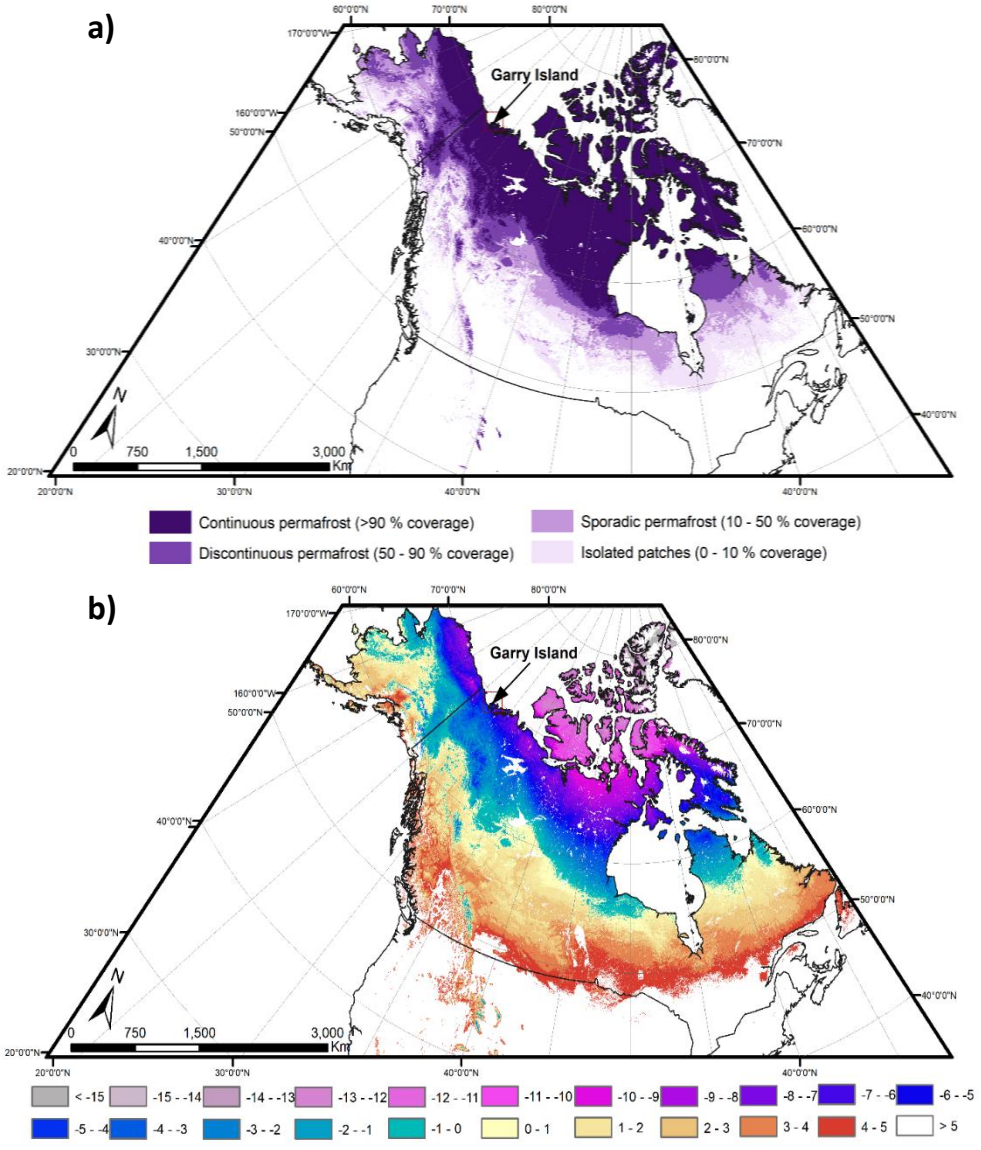

Figure 1.1: (a) Distribution of Canadian permafrost, showing Garry Island located in the continuous zone. (b) Mean annual ground temperatures modelled at the top of the permafrost, reporting -4ºC to -6ºC for Garry Island. Datasets from Obu et al (2018).

1.1.2. Northern Alaska

Since 1977, thawing of Alaskan permafrost has accelerated in response to state-wide warming air temperatures (Osterkamp, 2003). Studying thaw processes is important in relation to PCFs because reservoirs of SOC are mobilised and redistributed from near-surface soils, resulting in increased carbon emissions, which in turn leads to global climate warming (Grosse et al., 2011; Schaefer et al., 2014; Nitze et al., 2018).

ALDS are prevalent across moderate slopes of North America, Canada, Alaska, and Siberia and are characterised by a shallow failure plane as thawed soils detach from the underlying permafrost and rapidly slide downslope (refer to Chapter 1, Section 1.4.3) (Lewkowicz, 1990; Lewkowicz and Harris, 2005a). Retrogressive thaw slumps (RTS) are located on similar slopes and within similar regions, but along the shores of lakes and rivers which initiates their formation as ice-rich permafrost is eroded and mud flows downslope (refer to Chapter 1, Section 1.4.4) (Burn and Lewkowicz, 1990). These hillslope processes are important because of the regional redistribution of soil carbon which has global implications as sediment enters fluvial systems (Gooseff et al., 2009).

In Northern Alaska, drill holes conducted by the US Geological Survey indicate regional warming of 2^{o}C to 4^{o}C since the 1940s within 0.2m to 2.0m below the ground surface (Lachenbruch and Marshall, 1986). In the Brooks Range and neighbouring Foothills (study region 2, Chapter 4), total warming has occurred at 1^{o}C to 2^{o}C magnitude, as a result of warmer winter temperatures (Osterkamp, 2005; Osterkamp, 2007).

1.2. Underlying Concepts

1.2.1. Permafrost

Permafrost is defined as perennially frozen ground which for two consecutive years remains at or below 0^{o}C due to a long cold winter but short summer thaw period (Jenness, 1949; Farquharson et al., 2019). It is important since it underlies ~25% of land within the Northern Hemisphere (Figure 1.2; Anisimov and Nelson, 1997). The spatial extent of permafrost, and the depth to which it can penetrate below ground (tens to hundreds of metres), is determined by interactions between surface temperatures, latitude, altitude and continentality (French, 2007; Vincent et al., 2017). The continuity of permafrost varies laterally with continuous

coverage of frozen ground found in the far north (except beneath water bodies) (French, 2007). This transitions into discontinuous regions further south as areas of unfrozen ground increase to the point where permafrost only exists as isolated islands (French, 2007). Continuous permafrost at high latitudes is due to low solar incidence angles which result in a low surface energy balance (Dingman and Koutz, 1974). The boundary marking the northern limit of discontinuous permafrost occurs at mean annual air temperatures of -6°C and -8°C and is defined by changes in snow cover (Smith and Riseborough, 2002). At lower latitudes, discontinuous and sporadic permafrost develops at high altitudes as environmental lapse rates of 6.5°C km^{-1} cause decreasing air temperatures at higher elevations (Streletskiy et al., 2015).

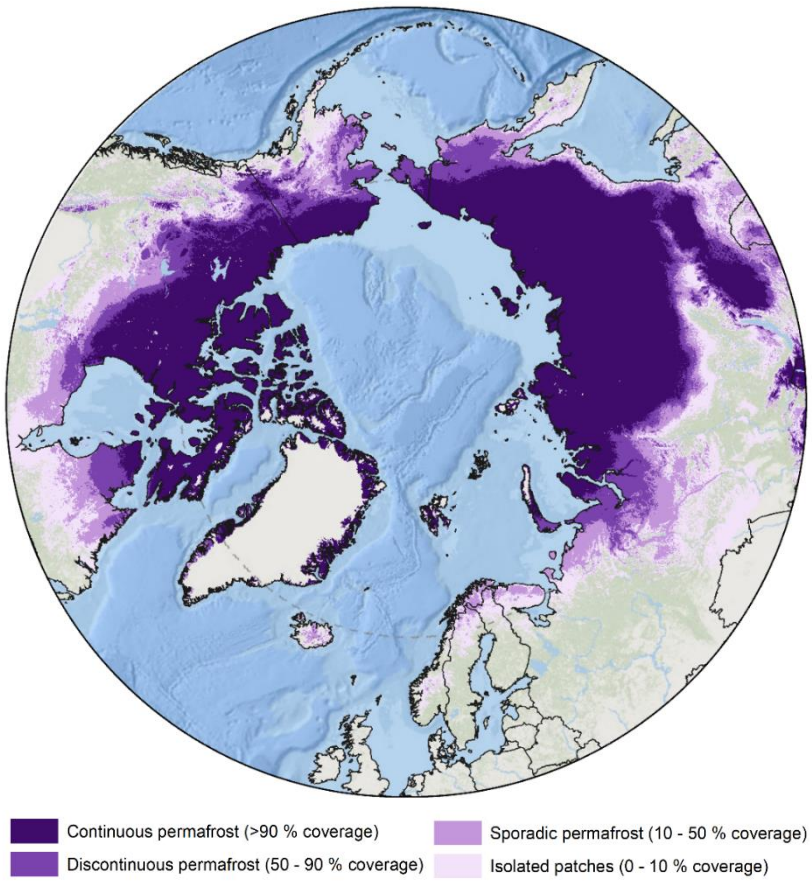

Figure 1.2: Shows the distribution of permafrost classifications in the Northern Hemisphere based on permafrost probability and modelled mean annual ground temperatures. Permafrost zonation shapefile provided by Obu et al (2018).

1.2.2. Surface Energy and Heat Balance

A negative heat balance controls the transition from continuous to discontinuous permafrost such that at higher latitudes winter energy loss from the surface exceeds summer internal gains within the soil, whilst the reverse is true of lower latitudes as the energy balance becomes more positive (French, 2007; Bowden, 2010). The balance between the soil's heat loss from the surface and the thermal conductivity of the Earth's interior with depth determines the relative thickness of permafrost at the lower boundary (French, 2007; Bowden, 2010). As geothermal warming is variable, there is a strong temperature anomaly that occurs with depth in the upper 100 metres of permafrost (Lachenbruch and Marshall, 1986).

1.2.3. Active Layer

The active layer is the uppermost ground layer which sits on top of the permafrost and intermediate transient zone (French, 2007). It experiences seasonal freeze-thaw when summer ambient air temperatures rise above 0ºC (French, 2007). Its thickness varies on an annual basis, primarily due to warming which converts soil ice to water as near-surface soil temperatures increase (Kane et al., 1991). This can result in the active layer thaw reaching decimetres deep (Kane et al., 1991). Projects such as the Circumpolar Active Layer Monitoring Programme (CALM) have been measuring and monitoring decadal changes within the active layer's three-part system (Figure 1.3) (Shur et al., 2005; French, 2007).

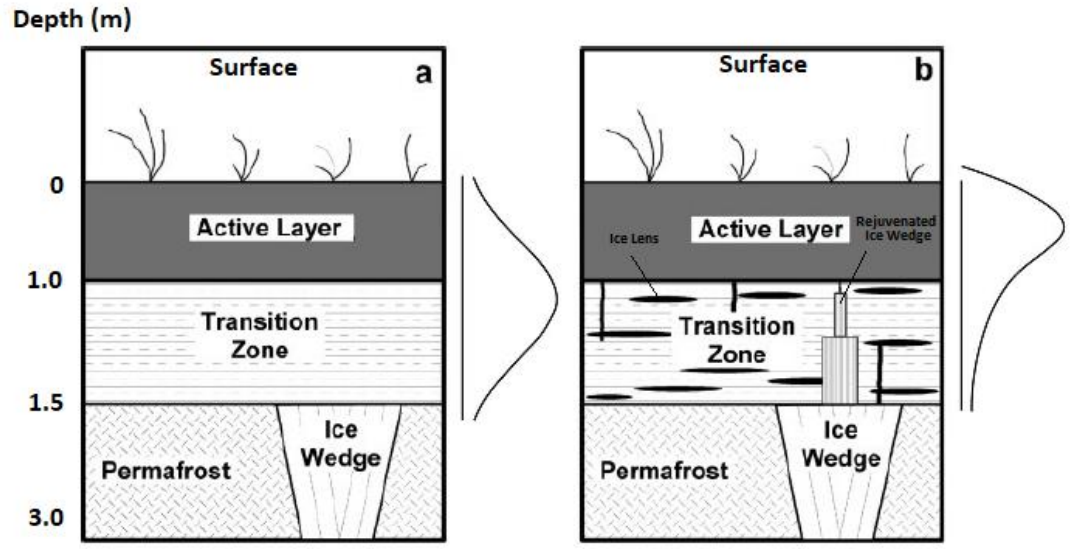

Figure 1.3: Three-layer conceptual model of the active layer after (a) deep thaw and (b) prolonged ice enrichment. Model adapted from Figure 1 in Shur et al (2005).

1.2.4. Thermokarst

Permafrost thaw at high latitudes occurs at both gradual (active layer seasonal surface thaw) and abrupt (deep thermokarst thaw) rates (Anthony et al., 2018; Turetsky et al., 2020). Under RCP4.5, carbon release from gradual thaw can be taken up by plants, whilst abrupt thaw from features such as lakes, thaw slumps and erosion gullies results in deep organic carbon mobilisation and emission increases of ~130% (Anthony et al., 2018). Vertical thickening of the active layer and increased surface temperatures lead to the development of hummocky thermokarst terrain associated with subsidence or erosion of the land surface (French, 2007). Summer thawing on hillslopes will result in a thicker active layer and subsequent slope instability due to a reduction in shear strength at the base caused by excess pore water pressures (McRoberts and Morgenstern, 1974; Gooseff, 2009).

1.3. Knowledge Gaps

Interactions between permafrost and climate constitute one of the largest terrestrial feedbacks (Abbott and Jones, 2015). The postglacial landscape is being modified from the regional to continental scale as disturbance regimes intensify and therefore increasing understandings of relationships between geomorphic settings and climate is important for the study of fluvial-geomorphic impacts as permafrost degrades (Kokelj and Jorgenson, 2013; Segal et al., 2016; Kokelj et al., 2017). However, using geomorphic change from abrupt thawing to estimate carbon release is limited which impacts carbon estimates on a global level (Hugelius et al., 2014; Abbott and Jones, 2015; Turetsky et al., 2019). Despite the number of Arctic hillslope thermokarst landforms increasing, they are underrepresented, particularly within large-scale studies, since they are difficult to detect within satellite imagery (Gooseff et al., 2009; Ramage, 2018; Turetsky et al., 2019). High-resolution (2-metre) remote sensing techniques such as the ArcticDEM (refer to Chapter 2, Section 2.3) allow for surface features which reflect the impacts of degradation to be mapped at a high temporal resolution over small spatial scales, capturing the local heterogeneity of permafrost landscapes (Westermann et al., 2015).

1.4. Arctic Permafrost Landscapes

In the circumpolar north, decreasing extent and continued degradation of permafrost over the last half a century in response to climate change has resulted in implications for topography, hydrology, infrastructure, and global climate (Streletskiy et al., 2015). The following section summarises the suite of micro- and macro-scale thermokarst landforms that develop following land surface collapse within Arctic periglacial landscapes (Figure 1.4; Kokelj and Jorgenson, 2013). Features which are the subsequent focus of Chapters 3 and 4 are justified, and more detailed descriptions of their formations are provided.

1.4.1. Periglacial Landforms

Thermokarst landscapes are geomorphologically diverse and influenced by local topographic, permafrost and ecological conditions and rates of temporal change (Kokelj and Jorgenson, 2013). Nevertheless, the terrain can be divided into three different landscape types, which collectively cover twenty-two different landforms (Kokelj and Jorgenson, 2013). These three landscape types contribute near equally to the northern permafrost region, collectively accounting for ~20% of its area (Olefeldt et al., 2016).

Wetland environments are characterised by thermokarst bogs and fens with the former creating circular, and the latter linear, depressions within fluvial and lacustrine deposits in discontinuous permafrost (Jorgenson and Osterkamp, 2005; Kokelj and Jorgenson, 2013). These occur due to peatland collapse which is significant since the permafrost zone within the circumpolar north is 19% peatlands, which are degrading rapidly (Tarnocai et al., 2009). The development of these features has significant ecological and hydrological implications due to shifts in vegetation communities and thawing of frozen soils (Kuhry, 2008; Wright et al., 2008). In colder permafrost regions, peatlands can support IW polygons due to histel (permafrost-affected organic soil) formation (Hugelius et al., 2014; Olefeldt et al., 2016).

The most prevalent and readily detectable form of thermokarst within lowland ice-rich permafrost is lake thermokarst (Kokelj and Jorgenson, 2013). The process of lake expansion, drainage and evolution typically begins with the degradation of high-centred IW polygons (Kokelj and Jorgenson, 2013). Within later stages, formation includes collapse pingos, as well as thermokarst troughs

and pits which often occur in basins of former thermokarst lakes or as a result of continued IW degradation (Jorgenson and Osterkamp, 2005; Kokelj and Jorgenson, 2013; Olefeldt et al., 2016).

Hillslope thermokarst, including ALDS, RTS and thermal erosion gullies constitute major thermokarst landforms associated with extreme events, heat transfer and hydraulic conductivity (Kokelj and Jorgenson, 2013). Detachment slides and thaw slumps occur on moderate slopes in hilly topography, most often near watercourses, therefore making them particularly important with respect to their impact on fluvial-geomorphic systems (Olefeldt et al., 2016). Failure and mass wasting alter surface runoff dynamics and trigger sediment and organic carbon transport into terrestrial and marine waterbodies (Bowden et al., 2008). Equally, thermal erosion gullies rely on surface water flow but through channels which are often provided by IW troughs (Kokelj and Jorgenson, 2013).

This thesis focusses on IWs (Chapter 3), ALDS (Chapter 4) and RTS (Chapter 4) within Arctic hillslope environments. The study of IWs is important since these features often trigger the formation of other thermokarst landforms and are characteristic of wetland, lake and hillslope thermokarst environments. Detachment slides and thaw slumps can significantly alter the ionic chemistry of Arctic stream networks due to large sediment inputs and the mobilisation of carbon stores (Kokelj et al., 2009a; Kokelj and Jorgenson, 2013).

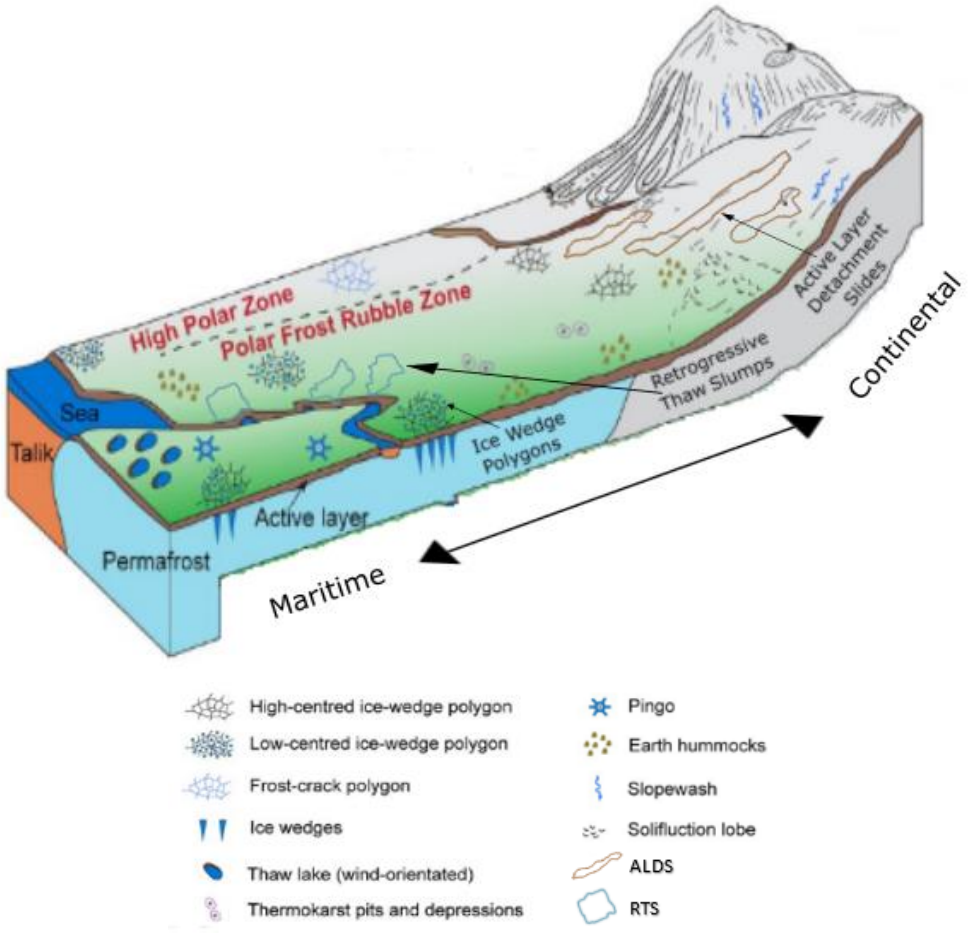

Figure 1.4: Schematic diagram of periglacial landforms found within wetland, lake and hillslope thermokarst environments. Diagram adapted from Giles et al (2017).

1.4.2. Ice Wedge Polygons

IW polygons are one of the most common ground patterns in the Arctic (Lachenbruch, 1962). IW formation is attributed to thermal contraction (Leffingwell, 1915) whereby groundwater continually freezes and expands as the soil contracts under cold winter temperatures, and cracks to increase the area in which the wedge ice forms (Leffingwell, 1915; Harry and Gozdzik, 1988). Regular cracking is characteristic of active IWs which are continuing to grow, as opposed to those which are inactive or relict, now simply preserved within permafrost (Mackay, 1975 in Harry and Gozdzik, 1988). Polygonal patterns spanning 5m to 40m, are produced as overlying soil is forced into ridges separated by centimetre- to metre-wide troughs as IWs continue to develop often reaching 3m to 6m deep (Lachenbruch, 1962; Black, 1982; Morse and Burn, 2013).

Located near the top of the permafrost and comprising ~20% of this volume, current literature indicates that IWs are susceptible to minor changes in temperature and precipitation over sub-decadal timescales; which is significant given the centuries to millennia over which they form (de Klerk et al., 2011; Kokelj et al., 2014; Liljedahl et al., 2016). After two decades of air temperatures being elevated by 5^{o}C, subsidence is likely to be initiated within the Canadian Arctic and troughs will become more discernible as they begin to develop and connect (Liljedahl et al., 2016). Burn (n.d) suggests that a window of opportunity for studying these features has emerged within the last decade, particularly across the Canadian Western Arctic, which must be explored before total drainage of the landscape occurs with further melting and trough infilling (Liljedahl et al., 2016).

Research into IW processes on hillslopes is disproportional to their importance as analogues of climate change. Whilst these structures were central to Mackay's (1995) work in terms of identifying and mapping IW types, their development is mostly documented across lowlands as opposed to hillslopes where the morphology is smoother (Burn and O'Neill, 2015). Assuming a uniform climate, similar features should exist on hillslopes, however these are more difficult to detect given the transitory state of the landscape. Anti-syngenetic IWs are most common on receding slopes due to downward growth and a net deficit of material as a result of erosion (Figure 1.5; Mackay, 1990; Mackay, 1995). Slope recession results in the truncation of these features over time (Mackay, 1995). At the base of the slope, these may evolve into syngenetic IWs as net gains in material, originating from upslope, allow for upward growth in the rising permafrost surface (Figure 1.5; Mackay, 1990; Mackay, 1995). Recent research conducted on hillslopes near Illisarvik suggests greater penetrating thaw depths have resulted in troughs which have deepened by >35 mm/yr (Burn, n.d). Compared with slope bases, the steeper gradient of hillslopes provides a more effective meltwater evacuation pathway, resulting in greater subsidence rates (Burn, n.d).

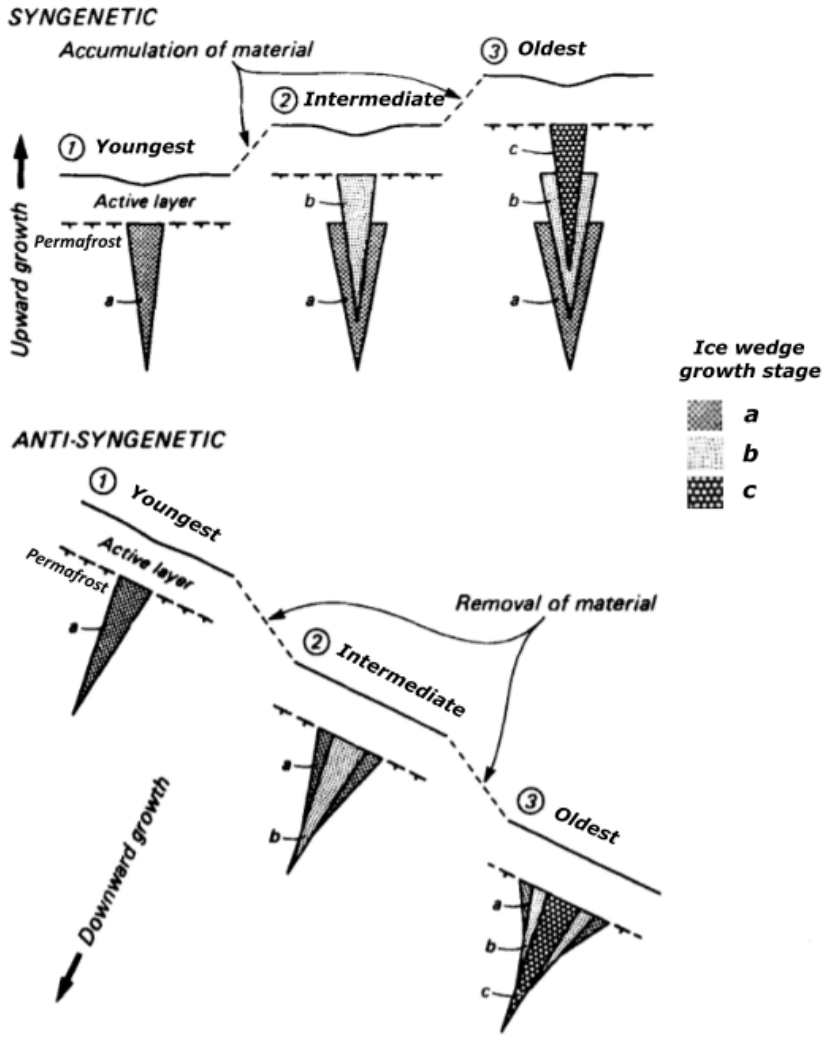

Figure 1.5: Schematic diagram showing the three growth stages of syngenetic and anti-syngenetic hillslope ice wedges. Figure adapted from Mackay (1990).

1.4.3. Active Layer Detachment Slides

These initiate in hillslope soils with high water pressure and a significant ice-rich zone (Lewkowicz, 1990; Harris and Lewkowicz, 1993; Lewkowicz, 2007). Mass-wasting occurs due to a loss of shear strength at the base of the active layer, causing gravitational sliding along a slip plane (Harris and Lewkowicz, 1993; Lewkowicz and Harris, 2005a; Lewkowicz 2007; Mithan, 2018). The detached active layer slides over the underlying permafrost, ultimately resulting in the displaced vegetation mat accumulating at the bottom of the slope (Bowden, 2010). Failures can initiate at multiple points along the feature's length, including propagation from the headwall scarp, through the runout zone or upwards from the compressional zone at the toe (Lewkowicz, 1990). However, they are relatively quick to stabilise, re-vegetating in 5 to 10 years (Swanson, 2014).

They are most common on north facing slopes of ~5º to 20º where significant ground ice forms due to lower solar radiation (Lewkowicz and Harris, 2005b; Swanson, 2014). However, ground ice, dependant on soil moisture and temperature, is a more important factor than aspect (Mithan, 2018). It has a direct impact on the extent of the failure and can therefore result in features being located on a range of slopes (Lewkowicz and Harris, 2005b). Consequently, sliding mechanisms will vary between continuous and discontinuous permafrost (Lewkowicz and Harris, 2005a). A low liquid limit and high silt content will result in viscous flow, whilst high quantities of both will enable development of a shear plane which slides as a cohesive block (Harris and Lewkowicz, 1993; Lewkowicz and Harris, 2005a; French, 2007;; Harris et al., 2008; Mithan 2018). The latter is likely to occur in cold permafrost regions, when the active layer experiences two-sided freezing (Mackay, 1981; Harris and Lewkowicz, 1993).

Features typically exhibit dimensions of 10's to 100's of metres long, 10m to 30m wide, and 1m deep (Figure 1.6; French, 2007; Swanson, 2014). Based on the type of movement, ALDS are classified morphologically as either compact, elongate or complex (Figure 1.6; Lewkowicz and Harris, 2005a). Continued retrogressive failure over multiple days results in the development of complex features (Figure 1.6.c.; Lewkowicz and Harris, 2005a). Either block movement results in cuspate headwalls at the scar zone of compact failures or multiple scar zones and linked downslope toes joins elongate failures (Lewkowicz and Harris, 2005a).

The sliding mechanism characteristic of these features means that they do not significantly penetrate the underlying permafrost and therefore debate centres on whether they should be included within studies of thermokarst terrain (Bowden, 2010). However, the impacts that they exert on the environment and the way in which continued thaw is initiated through their formation justifies their importance (Bowden, 2010).

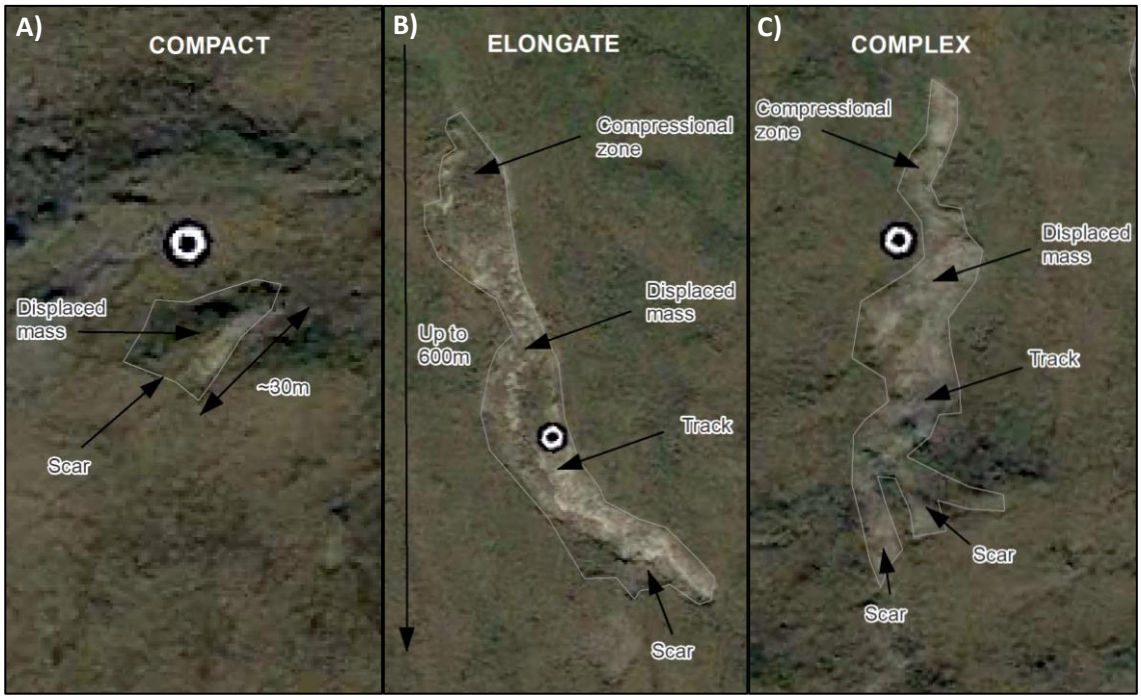

Figure 1.6: Illustrates the morphological forms of active layer detachment slides from (a) bell-shaped; to (b) hour-glass shaped, to (c) more complex forms with multiple scar zones. The delineated features are examples of those which are later analysed in Chapter 4.

1.4.4. Retrogressive Thaw Slumps

Thaw slumps are highly erosive features characteristic of the High Arctic which tend to form over several years, stabilising ~50 summers after initiation (French and Egginton, 1973). They are most likely to develop where ground ice deposits are continually exposed to thaw through combined thermal and geomorphic processes associated with wave action and fluvial activity such as lateral stream erosion (French, 2007; Lantuit et al., 2012; Kokelj et al., 2017). They are consequently categorised as polycyclic features, often developing from active layer slope failure or occurring at previous RTS sites (Lewkowicz, 1990; French, 2007; Lantuit et al., 2012). These processes are reinforced by permafrost warming, winter snowfall and vegetation feedbacks (Kokelj et al., 2009b; Lantuit et al., 2012).

Thaw slumps exhibit a distinctive steep concave headwall which is typically 1m to 2m high and is capable of average summer retreat rates of ~8m, dependant on scarp height (Figure 1.7; Lantuit et al., 2005; French, 2007). Back-wasting which serves to enlarge the headwall is caused by localised water flow, heat transfer and summer ablation which collectively thaw the ground ice with material produced accumulating at the base (Lantuit and Pollard, 2005; Kokelj and Jorgenson, 2013). The “matrix-supported diamicton” produced as a result

of slumping is transported across the gently sloping floor as debris, meltwater or mudflows which often flow across alluvial sediments to form more structurally complex deposits (French, 2007: 194).

Alongside ground ice, growth is influenced by topography, slope, and the nature of the debris itself (Kokelj and Jorgenson, 2013). Continued growth will cease when the amount of thawed sediments is significant enough to cover the ground ice and debris removal rates diminish (Lacelle et al., 2010). However, surface runoff due to processes such as rainfall and snowmelt can serve to re-initiate slumps by exposing previously buried ground ice (Lantuit et al., 2012). Intensification of air temperatures and precipitation have caused thaw slump activity to increase in frequency which increases volumes of eroded ground ice and has significant consequences for carbon release (Lantuit and Pollard, 2005; Kokelj et al., 2015). Thus, research into the climatic trigger mechanisms of these features is important in terms of landscape response. Thaw slumps can, over several years, occupy tens of hectares of terrain, thawing the top several metres of permafrost to expose previously trapped carbon, release solutes and allow for weathering (Kokelj et al., 2009a; Kokelj and Jorgenson, 2013). Future climate warming scenarios such as RCP4.5 are likely to act as triggering mechanisms for increased initiation rates, such that they will “rise to >10,000 decade^{-1} after 2075” (Lewkowicz and Way, 2019).

Figure 1.7: Indicates the geomorphological expression of a typical coastal retrogressive thaw slump. The delineated feature is an example of those later analysed in Chapter 4.

1.4.5. Summary of diagnostic features of ALDS and RTS

Several key diagnostic features distinguish the geomorphological footprints of ALDS and RTS. ALDS are identifiable as elongate features (up to hundreds of metres long), which are raised from the landscape as the vegetation mat detaches from the underlying permafrost and migrates downslope (Lewkowicz and Harris, 2005a; Bowden, 2010; Swanson, 2014). A steep concave headwall (1m to 2m high) and gently sloping floor are characteristic of RTS as backwasting incises the landscape, producing debris deposits which are transported away from the base (French, 2007; Kokelj and Jorgenson, 2013).

1.5. Previous Remote Sensing of Thermokarst

As the climate warms, permafrost degradation is becoming widespread across Arctic landscapes, resulting in the increased development of associated thermokarst landforms and features (Westermann et al., 2015). Changes to

permafrost characteristics, landscape dynamics and feedbacks over spatiotemporal scales are typically under monitored, despite their global impacts (Grosse et al., 2016). Remote sensing techniques have played a vital role in detecting, mapping, and quantifying aspects of degradational processes which would not be possible via field techniques (Hall, 1982).

Remote sensing techniques for permafrost cover ground-based (terrestrial photogrammetry, laser scanning and synthetic aperture radar), airborne and spaceborne methods over varying spatiotemporal scales (Kääb, 2008; Jorgenson and Grosse, 2016). The spatial and temporal scales over which thawing processes occur influences how they are captured by remote sensing (Westermann et al., 2015). Areal changes of features which indicate subsidence induced by degrading permafrost have utilised optical, microwave and LiDAR techniques to monitor ground changes (Lui et al., 2015). Synthetic aperture radar, corroborated by optical imagery were used by Balser et al., (2014) in the detection of RTS initiation between 2004 and 2005. Digital terrain models can be derived from these datasets and have the capacity to be used alongside spectral image classification, with the former being used to quantify vertical change and the latter to detect surface changes (such as disturbed vegetation) associated with hillslope mass movements (Kääb, 2008). Subsequent analysis by Balser et al (2015) incorporated their previous datasets and findings within a terrain suitability analysis to model the significance of different terrain factors for both RTS and ALDS across the Brooks Range of Alaska.

The topographic evolution of IWs and thaw slumps can be monitored using LiDAR (Kokelj and Jorgenson, 2013). Polygonal ground in Alaska was investigated by Hubbard et al (2013) using LiDAR-based geomorphic zonation to indicate drainage by extracting distance, slope, and curvature metrics to measure high and low-centred polygons. Along the Beaufort Sea coast, this airborne LiDAR was used by Obu et al (2017) to study RTS, however whilst the horizontal resolution was 1m, the observation period was short, with changes only studied over one year.

Seminal work on the mapping of polygonal networks has typically involved the collection of in-situ observations such as ground temperatures and ground ice to monitor subsidence and rates of IW cracking (Mackay and Burn, 2002). Alongside this, aerial photography has been key in terms of assessing regional

variability (Kokelj et al., 2014). However, some studies have combined this with remote sensing such as radar signatures to investigate soil conditions of IWs in Alaska (Arcone et al., 1982). Multiple techniques have been used to measure volumes of ground ice, such as in Northern Canada where this has been analysed using ground penetrating radar, DEMs (digital elevation models) and aerial photography (Bode et al., 2008). However, the DEM (created by the Northwest Territories Centre for Geomatics from air photos) used within this study had a vertical accuracy of ~1.5m and therefore the resolution was too low to accurately detect IW subsidence (Bode et al., 2008). Aerial photography has been central to the monitoring of ALDS and RTS by Swanson (2012) and Lacelle et al (2010) for identifying areal change and slump initiation. This data is ideal due to its significant temporal length (Westermann et al., 2015). However, the study of permafrost dynamics has progressed over the last decade due to advances in sensor capabilities, image processing, multivariate analysis, and more extensive archives (Jorgenson and Grosse, 2016). Whilst remote sensing is unable to directly measure subsurface changes such as thaw depths, DEMs have allowed for vertical and horizontal surface deformation of thawing indicators to be quantified from which the state of the permafrost can be derived (Westermann et al., 2015).

The analysis of remote landscapes using DEMs is highly valuable, both in terms of validating field research and providing a more detailed quantitative assessment of how landforms are evolving across differing spatial extents and geographical scales (Etzelmüller, 2000). The free availability and increased processing power of high-resolution remotely sensed data has transformed the spatial analysis of landforms and facilitated the development of geomorphometry (Evans, 2012). Topographic parameters which reflect the terrain such as slope, aspect and curvature can readily be derived from DEM data (Mithan, 2018). The ArcticDEM is one such example of a digital surface model which was developed (and released in 2016) in order to quickly and easily obtain large quantities of terrain data from remote locations (PGC, 2020a). In addition, ArcticDEM can be used to quantify rates and volumes of change, which will be a key component of this thesis (Williams, 2012; refer to Chapter 4). This subsequently allows for geomorphometric classification, by drawing relationships between these parameters and landform surface processes, with the relative dominance of these two different datasets exhibiting spatial variance (Etzelmüller, 2000). Pike (1988)

introduced the capabilities of GIS as a tool to automate landform characterisation from DEMs, to ultimately produce assessments of geometric signatures on a regional scale. The generation of these geomorphometric parameters can be used to map the distribution of landslide terrain such as ALDS and RTS (Pike, 1988).

1.5.1. Previous work in the Canadian Arctic

The foundations of research into the development and subsequent degradation of IWs in the Canadian Arctic were initiated by Mackay. His investigations into IW cracking at an artificially drained lake site at Illisarvik in 1978, typify processes occurring throughout Alaska and the Canadian Western Arctic (Mackay and Burn, 2002). Long-term field studies capturing both summer and winter observations which began with Mackay, have since been pursued by Burn (Burn and O'Neill, 2015). This has allowed for trends to be identified in lowland and hillslope IWs within the NWT (Mackay, 2000). Such research has investigated the contrasting "ridge-trough-ridge" morphology, which is readily identifiable in lowlands but, despite the presence of larger polygons, is more difficult to determine on hillslopes due to slope movement indicated by solifluction lobes (Burn and O'Neill, 2015).

Highly variable cracking frequencies on Garry Island were reported by Mackay between 1967 and 1987 with maximums ranging from 42% to 75% at different sites (Mackay, 1992). More recent observations in the NWT have shown that temperatures are above the cracking threshold, with high rates of thaw and subsidence now characterising the last two decades of measurements on Illisarvik, Richards Island (Kokelj et al, 2007; Burn, n.d). Recent field research conducted on hillslopes near Illisarvik suggests greater penetrating thaw depths have resulted in troughs which have deepened by >35 mm/yr over the last decade (Burn, n.d). On Banks Island, successively warm summers have led to significant trough subsidence and ponding on the hilltops, exposing epigenetic and anti-syngenetic wedges (Fraser et al, 2018).

The geomorphological transition of polygons from low-centred to high-centred has significant impacts on local tundra hydrology which are not well quantified (Liljedahl et al, 2012). These changes greatly impact watershed-scale hydrology as runoff from high-centred polygons is double that of low-centred (Liljedahl et al, 2012). Runoff is increased throughout trough formation, often due

to changes in the distribution of trapped snow and subsequent snowmelt pathways (Liljedahl et al, 2016). Whilst modelling local changes in snow distribution as polygonal networks form is important (for example this provides an explanation for cracking on Garry Island versus none at Inuvik), Burn (2004) argued that this is often not accounted for within numerical modelling. On the lowlands, Liljedahl et al (2016) used vegetation as an indicator of change. Thawing causes trough-ponding to increase when polygon centres drain, which results in wetland species such as water-tolerant sedges to become more abundant and lichen and moss cover to decline (Liljedahl et al, 2016).

1.5.2. Previous work in Northern Alaska

Within the Brooks Range ~20 types of thermokarst disturbance features can be found (Chapter 1, Section 1.4) which exhibit different feedbacks with the local terrain, climate, and ecosystem (Balser et al., 2015). Upland (stream valley) ALDS and lowland (lakes) RTS are the most dominant modes of thaw, typically occurring in ice-rich permafrost on slopes of 4^{o} to 15^{o} (Young et al., 2013; Balser et al., 2015; Rudy et al., 2016). ALDS involve the downslope mass movement of thawed soils which have detached from the active layer as a collective unit, resulting in a higher elongation ratio than RTS features (Kokelj and Jorgenson, 2013; Swanson 2014; refer to Chapter 1, Section 1.4.3). In contrast, RTS features tend to be deeper than ALDS features due to their eroding cut-banks that form through fluvial processes which thaw ice-rich sediments along lake shores (Kokelj and Jorgenson, 2013; Swanson 2014; refer to Chapter 1, Section 1.4.4). ALDS tend to be more abundant on north-facing slopes where a thicker snowpack and vegetation mat is able to develop within the “transition zone” due to lower levels of winter insolation and increased soil moisture (Lewkowicz and Harris, 2005b; Shur et al., 2005; Swanson 2014).

The influence of thermokarst processes on upland terrain such as the Brooks Range and Foothills is less well studied in comparison with Arctic lowlands, and the study of hillslope thermokarst is equally poorly documented (Gooseff et al., 2009; Bowden et al., 2012). Hillslope failures detach surficial soils from their substrate and locally mobilise otherwise static ancient stores of carbon and nutrients (Gooseff et al., 2009). Where features such as RTS are located near waterbodies, sediment runoff results in the release of carbon into more regional lacustrine and oceanic systems (Bowden et al., 2008). The resultant

PCF causes continued warming as greenhouse gases are released from the thawing permafrost (Siewert et al., 2015). Therefore, local hillslope failures are of great importance to the large-scale global climate system (Kokelj and Jorgenson, 2013).

Of the research conducted on Alaskan hillslope thermokarst, most notable studies include those which focus on: regional impacts of sediment and nutrient delivery (Bowden et al., 2008; Gooseff et al., 2009); reviews of thermokarst research (Kokelj and Jorgenson, 2013); databases synthesising and categorising thermokarst landscapes (Olefeldt et al., 2016); and thermokarst interactions with the terrain (Balser et al., 2015). The thermokarst feature inventory in Balser et al (2015) guides this analysis and is evaluated within the context of Olefeldt et al's (2016) classification map of hillslope thermokarst. Within the Balser et al database, 2492 ALDS and 805 RTS were mapped using a combination of the University of Alaska Fairbanks aerial photo analysis; field GPS surveys undertaken between 2006 and 2011 (Balser et al., 2009; Gooseff et al. 2009; Balser et al., 2014); and the U.S. National Park Service high-resolution satellite image analysis (Swanson and Hill 2010). Based on the aforementioned studies, the most crucial outstanding information relates to quantification of geomorphological change over a high spatiotemporal resolution to determine feature distribution, age and frequency which can subsequently be linked to landscape characteristics and processes. The information could be used in further research to estimate carbon release from individual features based on magnitudes of geomorphic change.

1.6. Aims and Objectives

The extent of thermokarst terrain has increased due to climate warming and this has consequently impacted the rate and magnitude at which thermokarst landforms are increasing (Kokelj and Jorgenson, 2013; Bowden, 2010). Gradual top-down permafrost thaw due to seasonal thawing of the surface is predicted to result in 18 million km^2 of active layer vertical thickening with impacts for carbon emissions (Anthony et al., 2018; Turetsky et al., 2020). Abrupt thaw mobilises deep carbon from thermokarst at an accelerated rate and therefore is capable of producing similar emissions and climate feedbacks in an area one sixth of the size of the region of gradual thaw (Anthony et al., 2018; Turetsky et al., 2020). Degradation poses significant issues for both the physical and human

environment, primarily in terms of carbon release, hydrology, vegetation, and ecosystems (Gooseff et al., 2009; Abbott et al., 2015; Olefeldt et al., 2016).

There is a requirement for additional information on geomorphological change of thermokarst features within permafrost environments in response to interactions between climate and topography. To address the issue, this thesis aims to: (i) map the distribution of hillslope process features across the Arctic; (ii) quantify their morphology and extents; and (iii) investigate their rates of formation. Specific attention will be placed on landscape characteristics such as changes to slope, aspect, and elevation; and subsequent impacts on Arctic fluvial systems and carbon release across the Arctic as permafrost degradation becomes more widespread.

The following objectives have been formulated for chapter three:

> ***O1****: Quantify annual subsidence rates associated with geomorphic degradation using the 2-metre gridded ArcticDEM.*
>
> ***O2****: Determine spatial coherence in patterns of elevation change by investigating trends at polygonal network sites.*
>
> ***O3****: Compare (1) vegetation growth facilitated by water routing and (2) snow accumulation due to prevailing winds over topographic depressions, with patterns of positive elevation change.*

The following objectives have been formulated for chapter four:

> ***O1****: Quantify statistical relationships between large-scale regional terrain properties, such as elevation, slope, and aspect, and thermokarst feature occurrence using the 100-metre gridded ArcticDEM.*
>
> ***O2****: Determine small-scale morphometric characteristics of hillslope thermokarst feature types using the 2-metre gridded ArcticDEM.*
>
> ***O3****: Compare morphometric characteristics from Google Earth Imagery and ArcticDEM to identify rates of change in areal extent over time.*

1.7. Thesis Structure Outline

After conveying the global importance of changes taking place within Arctic periglacial environments and introducing recent work conducted across this region, the following chapters will use the outlined objectives to guide further investigation. Chapter 2 will present the detailed methodological approach devised for hillslope thermokarst change detection using ArcticDEM. Chapters 3 uses Garry Island, Canada to develop a methodology with which to detect and quantify changes to thermokarst features. Chapter 4 develops and extends this methodology by applying it to the Brooks Range of Northern Alaska to detect mass failures. A synthesis which draws together findings and discussions from Chapters 3 and 4 is outlined in Chapter 5. Here, areas where degradation is likely to initiate are identified (Section 5.2.1), and wider Arctic implications in the context of sediment loss and estimated carbon release are addressed (Section 5.2.2).

Chapter 2

Methods

This chapter provides detailed information about datasets, tools and techniques developed and later implemented in Chapters 3 (Garry Island) and 4 (Brooks Range). Two main study areas are introduced which collectively cover three forms of degradational processes prevalent across hillslopes in the High Arctic. Garry Island is used as a test area to develop the method ultimately used throughout. ArcticDEM is introduced from which a DEM differencing method for investigating periglacial landscape change is undertaken. Study region-specific methods undertaken include snowblow modelling on Garry Island and geomorphological characterisation of the Brooks Range. Dataset inventories, model builder workflows and RMSE tables are included such that the methodology could be replicated and/or reproduced for additional Arctic thermokarst environments.

2.1. Study Locations

Table 2.1: Basic conditions of each study region within the overall Arctic context. These conditions are described in further detail in: Chapter 3, Section 3.1.2; and Chapter 4, Section 4.1.2.

	Garry Island	Brooks Range
MAAT	-15°C (at northern limit) (Brown, 1970)	10°C to 12°C (in July) (Walker et al., 2002)
MAGST	-4°C to -6°C (Obu et al., 2018)	-5°C to 1°C (Balser et al., 2015)
Permafrost type	Continuous (Obu et al., 2018)	Continuous (Obu et al., 2018)
Climate zone	Arctic Bioclimate Subzone E (Balser et al., 2015)	Climate-driven ecosystem modified (Shur and Jorgenson, 2007)
Geology	Ice deposits from advances of the Laurentide ice sheet (Wisconsinan glaciation) (Pollard, 1990)	Complex glacial deposits and exposed bedrock (Balser et al., 2015)
Vegetation	Tundra vegetation (Government of the NWT, 2014)	Tussock tundra and Arctic low shrubs (Walker et al., 2002)

2.1.1. Garry Island, Northwest Territories, Canada

IWs are particularly prominent within periglacial landscapes due to their "distinctive surface manifestation" with ground subsidence measuring decimetres in depth (Chapter 1, Section 1.4.2) (French, 2007:176; Liljedahl et al., 2016). These are widespread across the Arctic with approximately 10% of terrain within the Canadian NWT being occupied by high-centred polygons (Liljedahl et al., 2016). Ice deposits originate from advances of the Laurentide ice sheet during the Wisconsinan glaciation (Pollard, 1990). Over millennia, cooling Holocene climates have caused IW networks to develop on hilltops and slopes. As these become truncated at the permafrost table due to solifluction, relict Pleistocene ice is exposed and cracking may reactivate Wisconsinan wedges (Mackay, 1995; Fraser et al., 2018). Uplands are being transformed by climate-driven thaw of these features on hilltops as the active layer responds to summer warming, whilst in low-Arctic and subarctic regions thermokarst is more stable due to protective buffering provided by the organic layer (Fraser et al., 2018). This study samples IW networks on Garry Island (Figure 2.1) where hillslope troughs have been observed to be degrading over the past decade.

Field studies conducted by researchers at Carleton University have identified locations of significant thaw subsidence at 69 29.786 N 135 45.208 W and 69 29.935 N 135 46.460 W (Burn, pers. comm). Ongoing monitoring by Burn over the last two decades at the neighbouring Richard's Island has detected similar patterns of high hillslope subsidence rates (Burn, n.d). Garry Island is therefore an ideal test area for validating DEM differencing and other remote sensing techniques, by comparing these results with those obtained from fieldwork (Chapter 3, Section 3.4). Methods developed for Garry Island will then be used to quantify recent changes in northern Alaska where thermokarst features are undergoing more extensive subsidence.

2.1.2. Brooks Range and Foothills, Northern Alaska

Within the Brooks Range and Alaskan Foothills (Figure 2.1), ALDS and RTS are the most prevalent forms of permafrost degradation (Chapter 1, Section 1.4) (Balser et al., 2015). The frequency and rate of retreat of these thermo-erosional features across the low Arctic of North America has increased since the twentieth century due to climate warming (Balser et al., 2014). Geomorphology of this

continuous permafrost zone is attributable to complex glacial deposits comprising drift sheets from four distinct glacial intervals dating back to the early Pleistocene (Hamilton, 2003; Balser et al., 2015). The study area lies within the warmest Arctic Bioclimate; Subzone E (Balser et al., 2015). With mean temperatures of 10^{o}C to 12^{o}C in July, this zone is predominantly comprised of tussock tundra and Arctic low shrubs (Walker et al., 2002). The spatial distribution of failures is driven by ground ice conditions, controlled by landscape and terrain properties which can be observed using ArcticDEM (Balser et al., 2015). Disturbance rates depend on regional climate warming events which are also influenced by the terrain; this further highlights the importance of studying these parameters to improve understanding of the drivers of change (Balser et al., 2015).

Following Balser et al (2015) this thesis considers 2492 ALDS and 805 RTS features across the Brooks Range where previous investigations have shown that above average summer warming and rates of thaw were responsible for feature initiation between 1997 and 2010 (Balser et al., 2015). In the Noatak Basin, 80% of the features monitored were detected within ERS Imagery between June 2004 and July 2005 due to warmer than average temperatures in summer 2004 (Balser et al., 2014). The disturbances investigated within this thesis occur over differing elevation, slope, and aspect ranges (Table 2.2). Four sub regions were selected, based on a feature density, which reflect the highly variable terrain. They encompass both high and low elevations across a range of longitudes to account for differing climate divisions which influence feature formation (Table 2.2). The sample of features mapped within sites, selected based on Balser et al (2015) points viewed within Google Earth (GE) Imagery, comprise varied spatial morphometries. Measured changes in the size, shape, depth, and area of features derived from ArcticDEM can be used to estimate rates of change and carbon release over time (Chapter 5, Section 5.2.2).

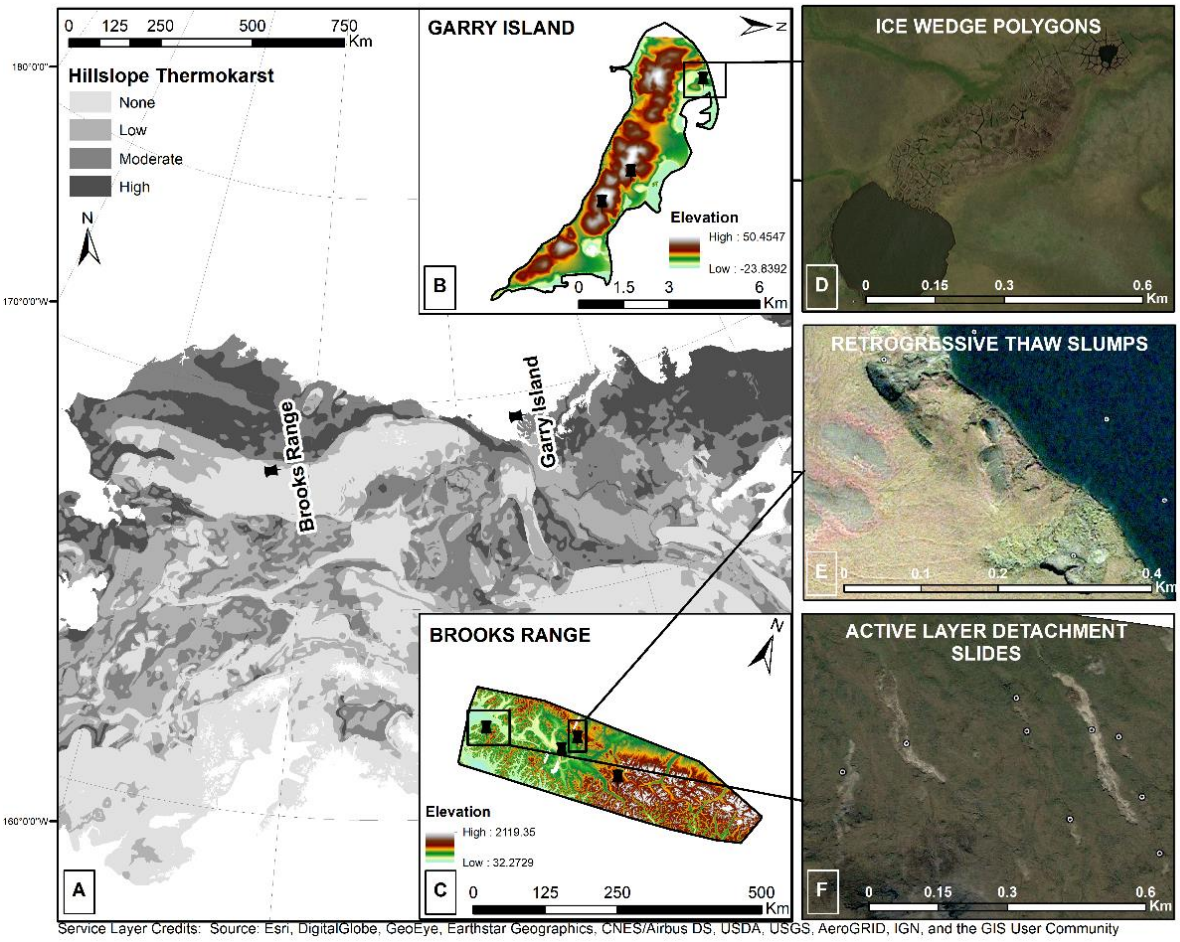

Figure 2.1: (A) Locations of Garry Island and the Brooks Range in the context of Arctic hillslope thermokarst, with elevations and sub regions of analysis shown for each study region (B) and (C). Panels (D), (E) and (F) indicate examples of features which will become the focus of the analysis. The thaw slumps in (E) are located on the bank on Feniak Lake (68.2557° N, -158.3247° W). ArcticDEM data provided by: Porter et al (2018); PGC (2020a).

Table 2.2: Average characteristics for each study region and sub-region sampled.

		Longitude	Latitude	Area (km^2)	Elevation (m)	Slope (°)	Aspect (°)
Garry Island		-135.71	69.49	20	16	4	175
Brooks Range		-156.59	67.96	67,204	737	8	170
	Site 1	-157.91	68.26	391	615	6	186
	Site 2	-158.42	67.95	331	300	8	161
	Site 3	-161.44	67.78	1,149	476	10	192
	Site 4	-155.83	67.96	190	970	7	150

2.2. Justification of Methods

Arctic warming is exceeding the global average, with warming of 0.75^{o}C (relative to 1951-1980 average) over the last decade resulting in large-scale terrestrial responses (Post et al., 2019). This is primarily driven by Arctic amplification as warming temperatures cause retreat of snow and ice cover which influence albedo feedbacks between the ocean and atmosphere (Serreze et al., 2009). However, surface air temperatures vary both regionally and seasonally as a result of sub-regional warming events (Overland et al., 2004). The use of remote sensing in this analysis allows for change to be quantified in locations, such as the Canadian High Arctic, that are under sampled by in-situ data (Metcalfe et al., 2018). The high-resolution ArcticDEM can be used to determine past, present, and future responses of the High Arctic to climate change which will increase their representation within predictive models (Metcalfe et al., 2018). The approach used corresponds with those implemented in similar studies of permafrost degradation across the North Slope of Alaska (Miller et al., 2019). Change has been investigated using ArcticDEM data at 2-metre and 100-metre resolutions. Large-scale controls are derived using 100-metre gridded data (used in Chapter 4, Section 4.3.1), whilst morphometric analysis at the 2-metre scale enhances the quantitative information that can be extracted (used in Chapter 4, Section 4.3.2). This allows for the calculation of volumes of change within individual features.

2.3. Digital Surface Model of the Arctic (ArcticDEM)

2.3.1. Data Source and Processing

High-resolution Arctic terrain data was derived from: (1) high-quality sub-metre stereo imagery from DigitalGlobe's Worldview-1, 2 and 3 satellites; (2) petascale computing running on the University of Illinois's Blue Water supercomputer; and (3) open source photogrammetry using the Ohio State University's Surface Extraction with TIN-based Search-space Minimization (SETSM) (Morin et al., 2016). These 2-metre resolution DEM strips covering the entire Arctic above 60^{o} north were the result of a collaboration between the US National Geospatial-Intelligence Agency (NGA) and the US National Science Foundation (NSF) (Morin et al., 2016; Candela et al., 2017). The dataset is used to quantify varying spatial geomorphology and topographic change within thermokarst environments both seasonally and inter-annually.

ArcticDEM is derived from optical imagery and therefore atmospheric conditions (water, vegetation, and snow) are difficult to penetrate which may impact the ground elevations captured (PGC, 2020b). Bare-earth products such as the SRTM digital surface model apply static adjustments to correct vertical heights over vegetated areas (O'Loughlin et al., 2015). However, noise and errors in the extracted terrain values will be apparent within the ArcticDEM since there is no bare-earth product (O'Loughlin et al., 2015; PGC, 2020b).

2.3.2. Geoid, Ellipsoid and Datum

ArcticDEM strips are vertically referenced relative to the WGS84 ellipsoid (PGC, 2020c) which varies in height from the geoid (approximate mean sea level (MSL)), dependant on location (Fraczek, 2003). Where heights were originally referenced above MSL, satellites now typically use height above the ellipsoid which approximates the shape of the Earth using a mathematical model (Li and Götze, 2001). These have a higher degree of accuracy, with the WGS84 ellipsoid producing an uncertainty of ~2cm from the centre of mass (Zilkoski et al., 1997). Datums use local elevations to fix the ellipsoid to the Earth (Morgan, 1987). The two datums used within this study are NAD83 and WGS which use the ellipsoids GRS80 and WGS84 (Morgan, 1987). Above the ellipsoid, elevation is 0 and distances are calculated from this such that measurements can be positive or negative which may be misleading (Li and Götze, 2001). Theoretical sea level estimated by an ellipsoid is relative to the Earth's gravitational potential and therefore irregularities in this surface impact measurements (Li and Götze, 2001; Fraczek, 2003). Using a geoid height calculator, undulations from the ellipsoidal height calculated for Garry Island are -5m (UNAVCO, 2019).

2.3.3. Data Outputs

2-metre resolution tiles were utilised within the change detection analysis of both study regions (Appendix A and B). These individual DEM strips are assigned a specific time and date relating to their orbit acquisition (PGC, 2020c). Within the Brooks Range study region, 100-metre mosaic data were also used to extract terrain properties such as slope, aspect, elevation, and northings/eastings (Chapter 4, Section 4.3.1). The best quality DEM strips are compiled into a mosaic dataset which provides a more extensive coverage (PGC, 2020c). This large-scale differencing was undertaken in order to quantify geostatistical

relationships between locations of thermokarst features and topographic conditions.

Whilst the 0.5m vertical precision of ArcticDEM was sufficient to resolve degradation of ALDS and RTS (Chapter 4), detection was more difficult where more subtle elevation changes occurred in IWs (Chapter 3; Morin et al., 2016). This study was constrained temporally due to data only being available for the period 2010 to 2017. It was also limited spatially due to incomplete DEM coverage across the study regions.

2.3.4. Mean Adjustment

ArcticDEM reports a vertical accuracy of -0.01m ± 0.07m when statistically fit to seasonally-subsetted ICESat (laser altimeter Ice Cloud and land Elevation Satellite with decimetre level vertical accuracy) elevations (Schutz et al., 2005; Candela et al., 2017). However different Worldview satellite sensors within the ArcticDEM constellation introduce further biases between DEMs (Candela et al., 2017). The aim of this investigation is to study relative changes in elevation between ArcticDEM pairs in order to focus on measuring geomorphic change which may have occurred over time as a result of permafrost degradation. The approach taken was to remove possible inter-DEM elevation biases which may be associated with absolute changes. Potential noise signals were filtered out therefore decreasing error and uncertainties and increasing the reliability that measured change is due to land subsidence (Williams, 2012).

The methodology for reducing bias across ArcticDEM strips was initially tested and developed using Garry Island as a training site. A raster calculation to identify a high elevation, low slope control area (Equation 2.1) was formulated using the ArcticDEM date 16th May 2017 and a derivative slope map (evidenced in Chapter 3, Section 3.2.2). Using zonal statistics extracted from the control area for each ArcticDEM tile, elevation was adjusted to equal the middle date within the time series (7th November 2013). With a maximum and minimum values of 16.7m and 12.5m across the time series, this date aligned closest with the median value of 14.6m (Figure 2.2.a.). No thermokarst associated change was expected to have taken place at the control site since anti-syngenetic and syngenetic IWs characteristic of Garry Island do not occur on low angled slopes (Kokelj et al., 2014). At the control site, the mean elevation difference (Figure 2.2.b.) was

removed such that landscape subsidence remained (Miller et al., 2019). This initial pre-processing stage was similarly applied to the DEM strips used for the Brooks Range (Chapter 4, Section 4.2).

Equation 2.1:

$$(Slope(ArcticDEM) \leq 2)\ AND\ (ArcticDEM > 10)$$

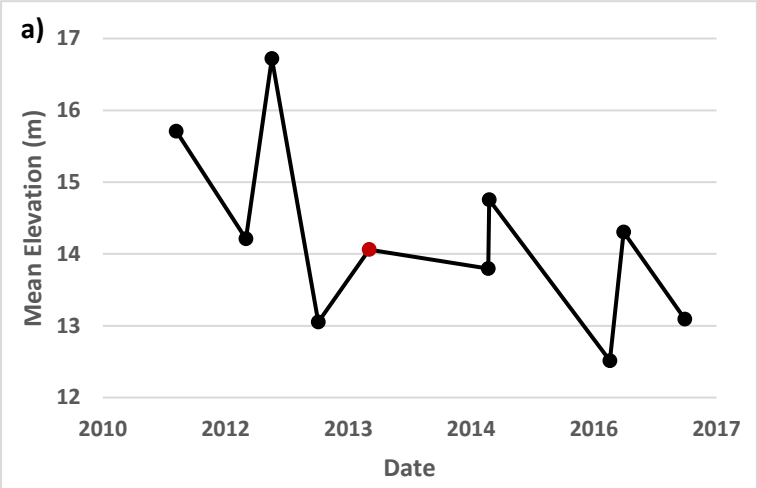

b)

Date (DD-MM-YY)	Mean Difference (m)
13-09-11	1.65
23-06-12	0.15
06-10-12	2.66
13-04-13	-1.00
07-11-13	
07-03-15	-0.26
11-03-15	0.70
14-07-16	-1.55
09-09-16	0.25
16-05-17	-0.97

Figure 2.2: (a) Mean elevation at the control site for each ArcticDEM date, derived from zonal statistics. The ~median date 7th November 2013 (indicated in red) was used to adjust the means of each year. (b) Shows the amount by which each ArcticDEM year had to be adjusted.

2.3.5. Elevation Model Differencing

At the selected study sites within each study region, pairs of 2-metre resolution DEM strips were selected. Where possible these spanned the full temporal range of the ArcticDEM from 2007 to present. Tiles were selected which provided the most complete coverage of (1) Garry Island and (2) the Balser et al (2015) feature locations (Appendix A and B). Following Miller et al (2019), raster calculations subtracted the historical DEM tile within each pair away from the most recent tile to provide a series of difference rasters indicating where positive and negative landscape change has occurred over time. Within polygonal networks, positive elevation changes may occur with thermal expansion, as IWs grow and the ground is subject to frost heave (Peterson and Krantz, 1998). Negative change represents ground lowering due to summer thawing of the active layer, which is characteristic of IW melt and hillslope mass failures (Murton, 2009).

2.4. Snowblow Model

Positive elevation changes were detected within difference rasters on Garry Island where negative changes would usually be expected as a result of IW degradation. An investigation was therefore undertaken to determine whether this was due to errors within the ArcticDEM or subsequent differencing method which would need to be corrected for. Snow was the most likely contributor given the image acquisition dates of September 2016 and May 2017 (Figure 3.9, Chapter 3). Therefore, an ArcGIS Python-scripted Snowblow Model was implemented to simulate the varied topographical redistribution of snow as a result of prevailing wind direction and in this case ultimately produced a binary shelter index (Mills et al., 2019). Originally developed by Mills et al (2019) to model wind erosion processes for the Ellsworth Mountains in West Antarctica, input parameters were consequently altered in relation to the study of Garry Island. For computational ease, the DEM was resampled to a coarser 10 metre grid and a northeast (NE) dominant wind direction was used based on data from the Tuktoyaktuk weather station, provided by Environment Canada. The output shelter index ranging from no shelter (0) to shelter (1) is derived from linearly scaled aspect and slope indexes, where the aspect index is 1 and the slope index was set at 5^{o} for Garry Island. The purpose of the shelter index is to identify where 'units' of snow are blown in from neighbouring cells and erosion is low, resulting in a net gain of snow and therefore a higher shelter index value (Mills et al., 2019).

2.5. Characterisation of Arctic Geomorphological Forms

2.5.1. Google Earth Imagery

As a precursor to undertaking geomorphological mapping of thermokarst disturbances within Alaska using ArcticDEM, GE Imagery was used to distinguish the spatial extent of the features in the context of their local topography. Thermokarst feature locations compiled by Balser et al (2015) were viewed as KMZ files within high-resolution (<2.5m) DigitalGlobe QuickBird satellite imagery from 2008 which helped to identify feature proximity to their marked locations by Balser et al (2015). Those which were detectable within GE Imagery and subsequently selected for analysis, were those which were identified by NPS within IKONOS/Geoeye/Worldview imagery in 2010. Viewing features in this manner served to guide further analysis by determining whether the features

were present in the landscape pre-2010 and whether they were significant enough in size to be confidently detected by the ArcticDEM (Potere, 2008). To increase the scientific utility of this archive, the images were georeferenced to ArcticDEM strips (using geographic degrees, NAD83) by aligning the Balser et al (2015) location points in order to quantify horizontal positional accuracy. RMSE values based on the georeferencing process were calculated for all feature locations within each image (Table 2.3), with further combined RMSEs derived for each overall site using Equation 2.2.

Equation 2.2:

$$RMSE_{site} = \sqrt{\frac{(GRE_{image\ 1})^2 + (GRE_{image\ 2})^2 \ldots + (GRE_{image\ N})^2}{N}}$$

Table 2.3: RMSE values, associated with georeferencing, reported for each Google Earth image within each site of the study region. Gaps in the table represent the absence of the feature type in the image.

Site Number	Number of GE images within site	RMSE of ALDS (m)	RMSE of RTS (m)	Combined site RMSE (m)
1	4	1.29	1.41	1.60
		2.07	1.51	
2	2		8.23181e-011	1.07
			1.51	
3	6	6.26	4.65661e-010	3.00
		2.32831e-010	5.20625e-010	
		0	3.85	
4	3	3.77		7.35
		11.76		
		3.10		

2.5.2. Thermokarst Landform Identification

2.5.2.1. Manual Feature Area Delineation

The method of manual feature digitisation into polygon shapefiles is dependent on how the geographic feature is interpreted and captured. A technique for individual feature mapping within GE Imagery was developed based on disturbance initiation and formation, guided by mapping criteria for ALDS implemented by Mithan (2018). Each mapped feature extended from the initial bare-earth region at the headwall, through to the restabilising runout zone;

laterally constrained by highly disturbed soils which were identifiable in the imagery as lighter or darker than the surrounding vegetation (Figure 1.6 in Chapter 1, Section 1.4.3; Kokelj and Jorgenson, 2013). Within DEM differencing years, proximal areas of high magnitude positive and negative changes clearly highlighted headwall scarp locations. More subtle changes were often observed within the runout zone. Consequently, cross-referencing with the GE Imagery was occasionally required to indicate the approximate location of termination points of features.

2.5.2.2. Semi-automated Delimitation of Feature Dimensions

Spatial morphometry of thermokarst features within the Brooks Range, in particular the ALDS, was highly varied. To reduce the volume of manual measuring and to keep delineation techniques consistent across all features, a semi-automated method was developed using a series of ArcGIS tools within Model Builder (Figure 2.3). Once all features had been mapped as shapefiles, morphometric characteristics could be simultaneously measured using this single model (Sweeney et al., 2017). Approximate length and width of GE and ArcticDEM mapped features were derived. Each shapefile polygon was converted to a centreline, unsplit and the near distance between the unsplit line and feature edges was calculated. Average width was then derived by doubling this distance. Length was determined by creating a convex hull around each feature and calculating a minimum bounding geometry, to provide an approximate straight-line length of each feature. Depth was calculated by manually sampling elevation transects aligned at three equal intervals perpendicular to the straight-line length, calculating the difference between maximum and minimum measurements, and averaging the three results. The semi-automated method can rapidly capture characteristics, meaning that assessments of the spatial magnitude of degradation can be better constrained on a more frequent basis (Sweeney et al., 2017).

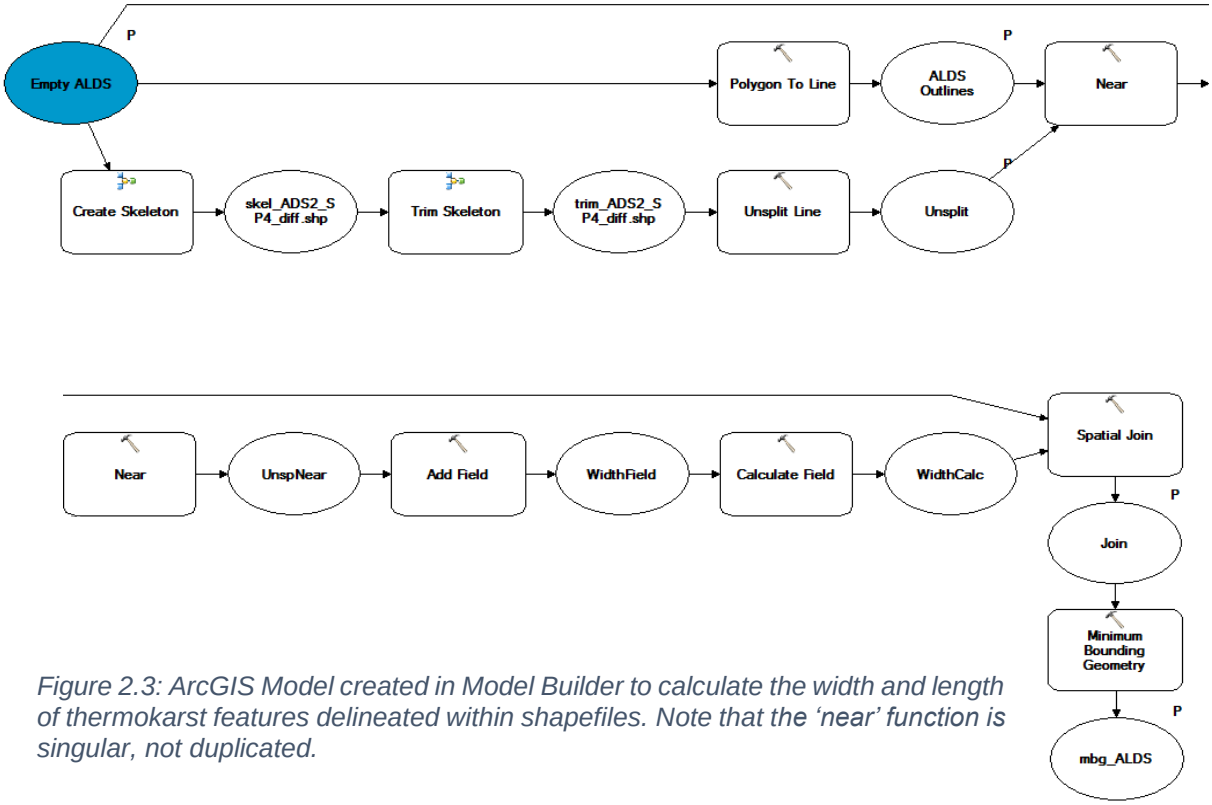

Figure 2.3: ArcGIS Model created in Model Builder to calculate the width and length of thermokarst features delineated within shapefiles. Note that the 'near' function is singular, not duplicated.

2.6. Probability-weighted Suitability Map

Elevation and slope data were derived for each thermokarst feature within the Balser et al (2015) database using the 100-metre gridded ArcticDEM. The geostatistical distributions of these results were subsequently used to create a map determining the susceptibility of terrain across the Brooks Range study region to the initiation of failures. The map takes slopes and elevations most frequently occupied by features and weights areas as highly or lowly suitable for their formation.

Equation 2.3:

$$Normalised\ probability\ function\ 1 = \frac{1}{\sqrt{2\pi}}\ e^{-(0.5\frac{ele - mean\ ele}{ele\ std.\ dev})^2}$$

Equation 2.4:

$$Normalised\ probability\ function\ 2 = \frac{1}{\sqrt{2\pi}}\ e^{-(0.5\frac{slp - mean\ slp}{slp\ std.\ dev})^2}$$

Statistical means and standards deviations for elevation (ele) and slope (slp) were used ($(0.5\frac{ele-mean\ ele}{ele\ std.\ dev})$) in order to calculate z-scores. Within each cell, this returned a value associated with the standard normal distribution that predicts the proximity of values to the mean, such that high or low z-scores are at the distribution tails. The former part of Equations 3 and 4 is a function which calculates the curve around the mean. This was ultimately squared to produce a positive value. Equations 3 and 4 were calculated for both ALDS and RTS and the results subsequently multiplied to produce a combined probability map, indicating areas which will be susceptible to either type of hillslope failure. Where elevation and slope conditions are most suitable for feature formation, a value nearer to 1 is achieved within the susceptibility map. Within the study region, this map has been used to indicate areas where features (1) may have formed but have not been mapped by Balser et al (2015) or (2) will be likely to form in the future (refer to Chapter 5, Section 5.2).

2.7. Summary

The overall approach aims to use high-resolution ArcticDEM data in order to quantify changes to hillslope thermokarst features within Canada and Alaska. Repeat DEMs are used to determine elevation change from vertical differencing therefore indicating thaw subsidence processes relating to IWs and mass failures. On Garry Island (Chapter 3), a snowblow model was used in order to explain positive elevation changes observed from ArcticDEM data (Chapter 3, Section 3.4.2). Within Alaska (Chapter 4), GE Imagery was used to inform sites selected for investigation with ArcticDEM. An automated process to map the geomorphometric form of individual features was devised. Using extracted terrain parameters, it was possible to identify areas which may be susceptible to ALDS and RTS (Chapter 5, Section 5.2.1). In addition, quantified rates of change allowed for estimating carbon release from individual features (Chapter 5, Section 5.2.2).

Chapter 3

An investigation into 21st Century changes in the ground structure of Garry Island, Canadian High Arctic, using remote sensing techniques

3.1. Introduction

This chapter seeks to quantify elevation changes on Garry Island, Arctic Canada, in order to determine the geomorphic impact of IW degradation. Although changes in High Arctic regions have been identified by in-situ observations and some remotely sensed imagery, there is a lack of quantifiable studies determining how warming has affected surface topography, particularly on hillslopes, in Arctic Canada. The ArcticDEM is therefore used to detect surface elevation changes (refer to Chapter 2, Section 2.3). DEMs covering a time period between 2011 and 2017 are tied together using a high elevation (>10m) /low slope (≤2^{o}) control area to minimise biases, identifying relative change caused by landscape subsidence (refer to Chapter 2, Section 2.3.4). The relatively short observation period of 6 years leads to an average detectable vertical rate of change of 0.03 m/yr on Garry Island, which corresponds with those observed in-situ in the western Arctic (Burn, n.d).Valuable data is missing specifically at above-local (regional) scales, and from remote sites that are difficult to study in the field. These locations can only be assessed using data products, such as the ArcticDEM, that afford a pan-Arctic view of hillslope change. Garry Island is an example of smaller-scale changes occurring within the Arctic which have been previously overlooked in landform classifications (such as Olefeldt et al., 2016), which highlights the novelty of this study.

3.1.1. Objectives

In order to fulfil the aim of this thesis as outlined in Chapter 1 (Section 1.6), this chapter sets out to investigate the following objectives:

O1*: Quantify annual subsidence rates associated with geomorphic degradation using the 2-metre gridded ArcticDEM.*

O2*: Determine spatial coherence in patterns of elevation change by investigating trends at polygonal network sites.*

O3*: Compare (1) vegetation growth facilitated by water routing and (2) snow accumulation due to prevailing winds over topographic depressions, with patterns of positive elevation change.*

3.1.2. Study Region

Garry Island is located within the NWT of Canada, 150km northwest (NW) of Inuvik at a latitude of 69^{o} 28'N and longitude of 135^{o} 42'W (Kerfoot, 1969; Mackay, 1975). Situated within the Beaufort Sea, the island is ~11km long and 0.8km to 3.2km wide (Kerfoot, 1969). Prevailing wind direction varies between NW and NE, with the highest wind speeds coming from the NW. At the start of the study period in 2011, the greatest frequency of wind speeds was recorded in the east. Monthly average temperatures reach summer maximums of ~12^{o}C in July contrasting winter minimums of ~-26^{o}C in February (Figure 3.2.b.).

Past glacial activity has played an important role in shaping the island's geology and in turn, the vegetation type (Kerfoot et al., 1969; Hill et al., 1990). Ice-thrust deposits attributed to the Early Wisconsin glaciation are responsible for deformed sediments composed of sand, silt, and clay (Kupsch, 1962; Kerfoot et al., 1969; Hill et al., 1990). The result is an island with relatively low relief (Figure 3.2.a.) and a broad distribution of elevations. These reach a maximum of 55m, although 94% are concentrated between 0m and 35m. Across the island, thermokarst features have developed in the form of polygonal ground as the thick permafrost (typically >400m in the western Arctic) has degraded, resulting in a deeper active layer and higher ground temperatures (Kerfoot et al., 1969; Mackay and Burn, 2002). Thermal-contraction cracking as outlined by Leffingwell (1915), has led to the development of the non-sorted hummocked ground which typifies Garry Island, as well as the wider Arctic region (Mackay, 1980). The "shrubs, herbs, mosses, and lichens" which make up the hummock-tussock tundra vegetation, owe their existence to the way in which geomorphic activity has shaped the island's drainage (Kerfoot et al., 1969).

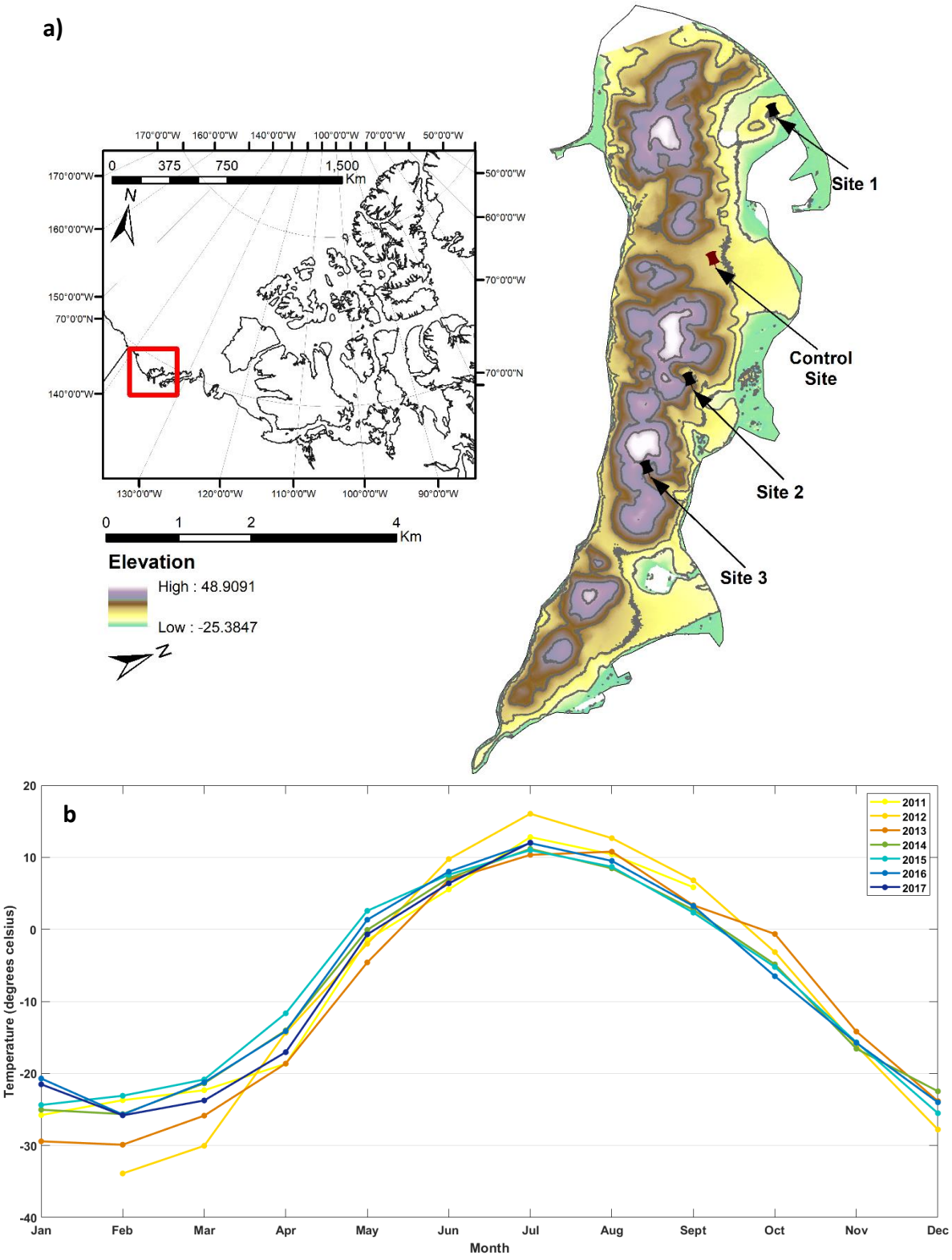

Figure 3.2: (a) Elevation of Garry Island using ArcticDEM data from July 2016 with 10m contour intervals to indicate relief. The three main study sites and control area are highlighted. (b) Monthly average temperatures using daily data from Tuktoyaktuk weather station, NWT, located at latitude 69.43, longitude -133.02 and elevation 4.6 m a.s.l. (Environment Canada, 2019). ArcticDEM data provided by: Porter et al (2018); PGC (2020a).

3.2. Methods

3.2.1. Approach

The approach uses ArcticDEM to identify spatiotemporal trends in IW degradation, by differencing DEMs to quantify vertical rates of change. The main methodology for control area and site selection, bias correction and elevation differencing is summarised here (Figure 3.3), with a more detailed account outlined in Chapter 2, Section 2.3. Additional methodology for Garry Island took the form of generating drainage lines using ArcHydro and calculating a shelter index using a snowblow model (Chapter 2, Section 2.4). These interconnected elements play an important role within the tundra microclimate (Liljedahl et al., 2012). Snow which accumulates within troughs contributes to the hydrological network through the summer snowmelt runoff period such that thermo-erosion can lead to runoff channelled through underground tunnels and gullies (Fortier et al., 2007).

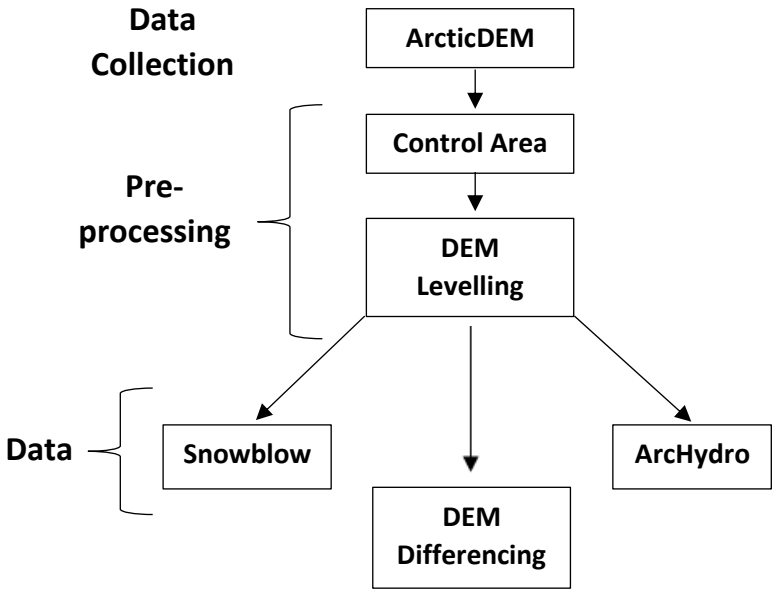

Figure 3.3: Workflow of the main methodological steps undertaken.

3.2.2. Pre-processing

A series of 2-metre resolution ArcticDEM tiles (Porter et al., 2018; PGC, 2020a) covering Garry Island were obtained between 2011 and 2017 (Appendix A, Chapter 2, Section 2.3.3). Using a DEM from May 2017 (Figure 3.4.a) and a slope map generated for the same year (Figure 3.4.b), a raster calculation (Equation 2.1, Chapter 2, Section 2.3.4),was used to select a control area with slopes ≤2^{o}

and elevations >10m (Figure 3.4.c). This was chosen based on the conditions required for IW growth in the NWT where (1) IWs are likely to occur on slopes of ~6^{o} as subsidence and meltwater evacuation are greater than on flatter ground (Burn, n.d) and (2) they are unlikely to form at very high elevations. Analysing 2017 DEM data of known extensive IW networks in the north of the island, slopes averaged 4^{o} and island-wide elevation averaged 16m, with elevation in the north averaging 5m. The purpose of identifying a control area was to select an area where thermokarst processes are unlikely to have taken place, and to use this control area to "tie" the DEM tiles together, so that any inter-DEM elevation biases are removed. Each DEM tile was tied to the middle date within the time series (7th November 2013) using the mean elevation value within the control area in order that subsequent differencing calculations would identify relative change rather than absolute elevations. Once the DEMs were tied to this master DEM, inter- and intra-annual elevation changes were calculated by simple differencing. These differences were then analysed in relation to elevation and slope values from the beginning of the time series (2011).

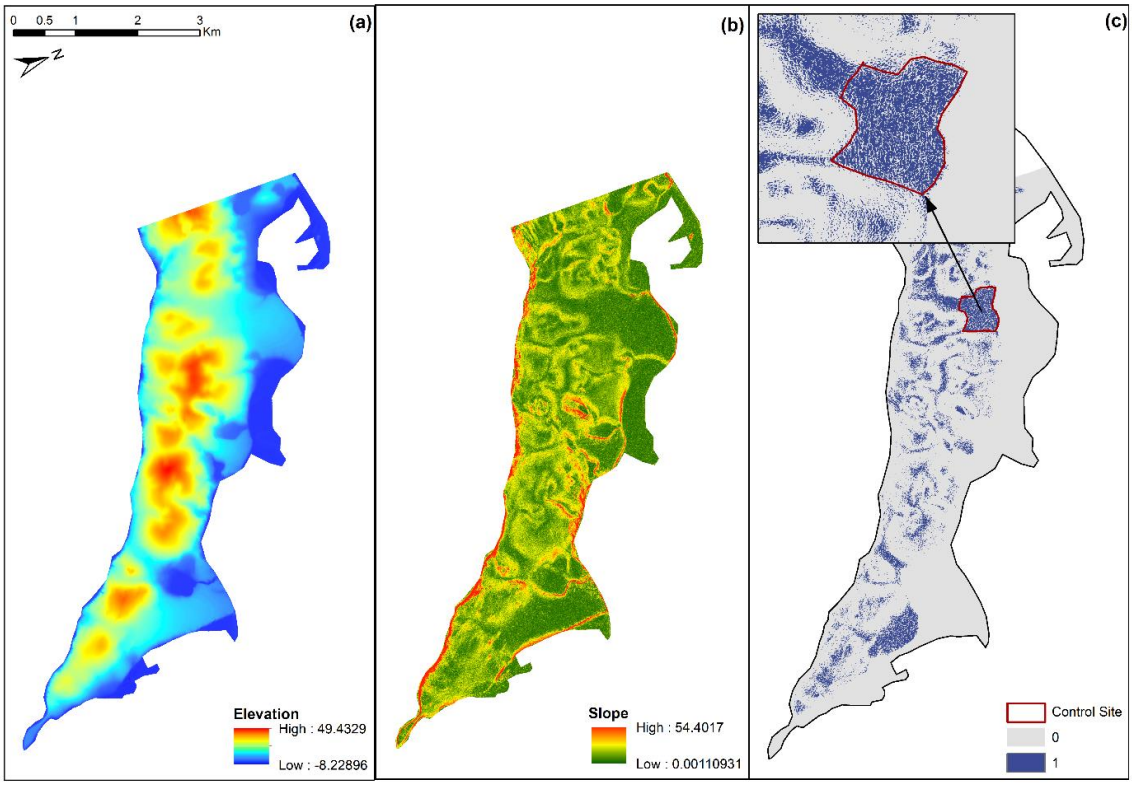

Figure 3.4: (a) ArcticDEM tile for May 2017 covering Garry Island, (b) slope map derived from the ArcticDEM tile and (c) control area identified using slopes ≤2^{o} and elevations >10m. ArcticDEM data provided by: Porter et al (2018); PGC (2020a).

3.2.3. Study Sites

3 study sites were selected which spatially represent Garry Island, covering the northern, middle, and southern portion (Figure 3.2.a.; Table 3.1). Site 1 was selected based on known polygonal networks identified through in-situ measurements (Burn, pers. comm). Sites 2 and 3 were selected based on observations of bands of positive elevation change detected within initial differencing.

Table 3.1: Locations of the control area and study site across Garry Island.

	Location	Area
Control Site	135°43'59.276"W 69°29'30.248"N	0.32km^2
Site 1	135°46'30.53"W 69°30'16.683"N	0.18km^2
Site 2	135°41'51.699"W 69°29'1.792"N	0.38km^2
Site 3	135°40'16.948"W 69°28'32.099"N	1.32km^2

3.2.4. Hydrological Network Analysis

The coupling between hydrological regimes and IW topography is important to investigate (Nitzbon et al., 2019). Spatial variability in hydrological conditions affects rates of IW degradation with resultant ground subsidence impacting surface and subsurface drainage, linked to polygon type (Nitzbon et al., 2019). Terrain pre-processing was computed on the master DEM (this provided total island coverage) to ultimately determine drainage paths on Garry Island. Terrain pre-processing involved filling sinks, followed by flow direction and flow accumulation in order to determine the steepest path of descent and the cell in which this accumulates (Merwade, 2012). Streams were defined using a threshold area of 1km^2 as opposed to the default, giving a denser stream network which was more appropriate for further analysis. Using flow direction and stream grid as inputs, stream segments were generated in order to delineate catchment grids and catchment polygons. The drainage lines produced help to identify routing of water and patterns of drainage across Garry Island.

3.2.5. Snow Drift and Accumulation Patterns Analysis

Patterns of snow accumulation are important because snow provides insulation to IWs which prevents winter cracking (Mackay, 1989). However, where snow accumulates in IW troughs and topographic depressions it influences local drainage as it melts (Liljedahl et al., 2016). Using a snowdrift model which runs in a Python Script, a shelter index was calculated (Mills et al., 2019). This produces a binary index to predict where snow will accumulate in gullies in the topography, based on an inputted DEM and varying wind direction and slope values (Purves et al., 1999; Mills et al., 2019). A tile from ArcticDEM, dated 16th May 2017, was resampled from a 2-metre grid to a coarser 10-metre grid in order to match with the computational capacity of the model. Alongside this, the other key input is prevailing wind direction. This was determined using wind data from Environment Canada for the Tuktoyaktuk weather station, ~100km east of Garry Island. Whilst wind direction is highly variable, the dominant directions in 2011 (start of the study period) were from the NW and NE (Figure 3.5).

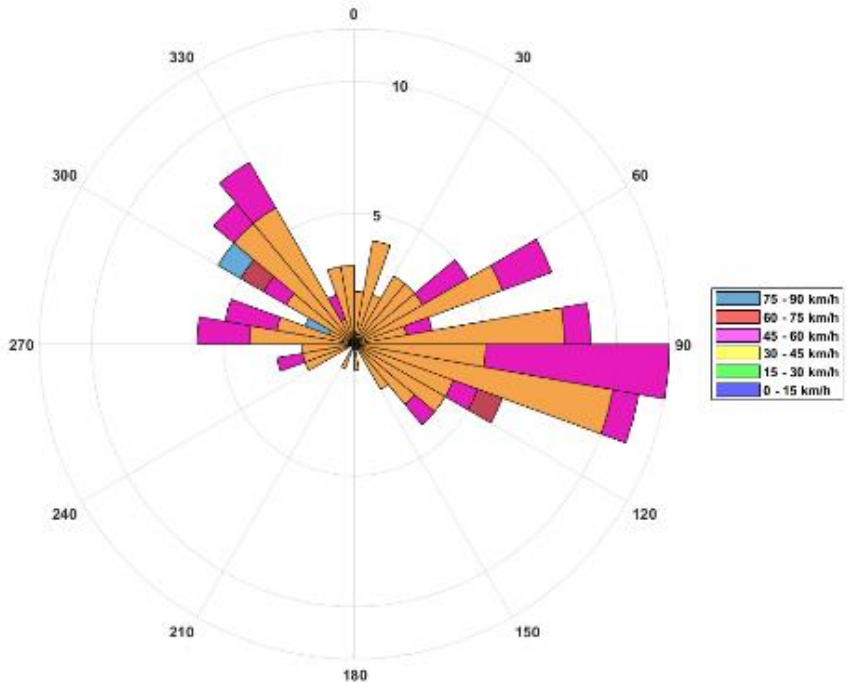

Figure 3.5: Wind rose for Garry Island using daily wind direction and wind speed data for the start of the study period in 2011. Data obtained from Tuktoyaktuk weather station, NWT, located at latitude 69.43, longitude -133.02 and elevation 4.6 m a.s.l. (Environment Canada, 2019).

The maximum and minimum slope values were defined based on investigation of a slope map produced for Garry Island. Slope values which corresponded with the location of gullies were concentrated between 5^{o} and 10^{o}, hence making these sensible choices for the maximum and minimum values. This value aligns with assumptions by Purves et al (1999) that state that 5^{o} is the pivotal point, above which the shelter index scales with increase in slope (Mills et al., 2019). A preliminary test using the minimum slope value of 0.001^{o} within the DEM generated an output whereby large swaths of the island were classified as sheltered (Table 3.2). This was due to the slope angle being too low, which impacted snow transportation such that snow was accumulating in very minor topographic depressions.

Table 3.2: Output table of iterations used in the snowblow model in order to determine the optimum parameters.

Output	Wind Direction	Min. Slope	Max. Slope
1	122.5	1.0	Off
2	292.5 (WNW)	0.001	Off
3	67.5 (ENE)	0.001	Off
4	90 (E)	0.001	Off
5	292.5 (WNW)	5	10
6	67.5 (ENE)	5	10
7	90 (E)	5	10
8	45 (NE)	5	10
9	315 (NW)	5	10

3.3. Results

Elevation change was analysed over the period 2011-2017, with elevations most frequently occurring between 10m and 15m in 2011 (Figure 3.6). In general, Garry Island has experienced an overall lowering in elevation, with average elevation reducing by 0.22m by 2017. However, across the island there are localised trends of uplift and subsidence. In upland areas there is significant subsidence on hillslopes north of Drinking Lake (Site 1) which may be linked to hillslope IWs and downslope movement. This is reversed in the south of the island (Sites 2 and 3) with positive elevation changes in distinct bands, which may be attributed to vegetation growth on southwest slopes. Inter- vs. intra-annual differencing revealed more nuanced patterns of change within the north-south divide of positive vs. negative change.

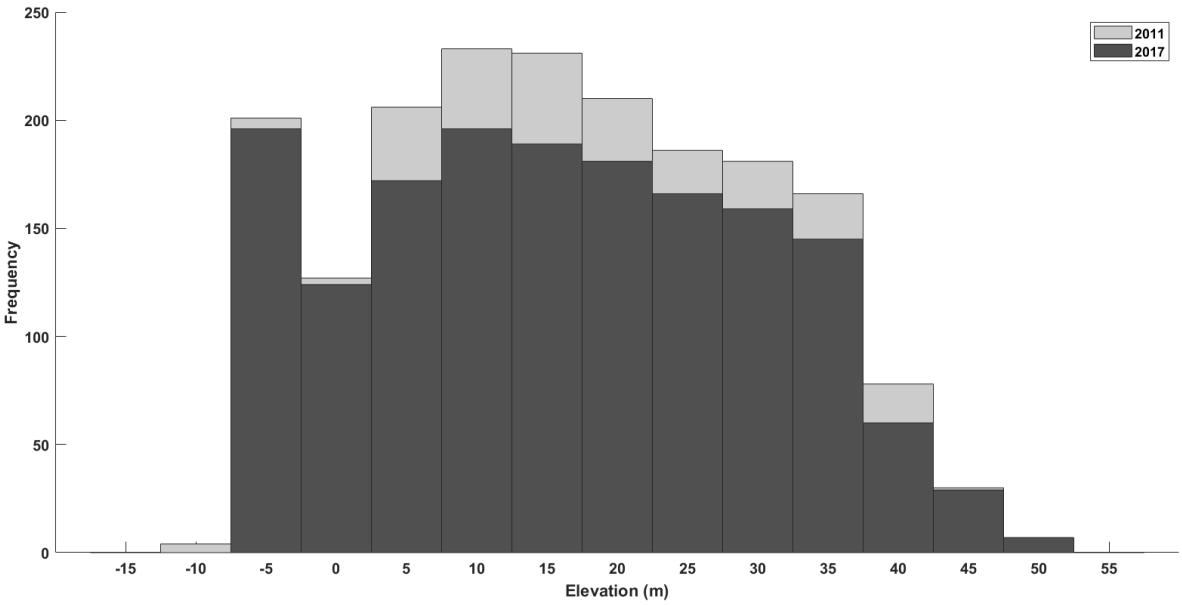

Figure 3.6: Hypsometry of Garry Island in 2011 (start of study period) and 2017 (end of study period). ArcticDEM data provided by: Porter et al (2018); PGC (2020a).

3.3.1. Long Term vs. Seasonal Changes

Seasonal variances in elevation demonstrate a clearer signal than the long-term trend in elevation differences on Garry Island (average elevation difference of -2.47m for July vs September 2016, -2.01m for September 2011 vs. September 2016) (Figures 3.7.a and 3.7.b). The hypsometry of seasonal elevations has a more symmetrical pattern either side of the 0m peak, with the highest values clearly occurring between -0.4m and 0.4m, as opposed to the long-term elevation frequencies which are slightly more skewed towards the positive (Figure 3.7.c). Seasonally, sub-metre positive elevation differences of ~0.5m dominate the NE side of the island, whilst negative elevation of a similar magnitude is characteristic of the southwest (Figure 3.7.a). Over the long term, the pattern is less spatially coherent (Figure 3.7.b), with 74% of elevation differences being concentrated between -0.2m and 0.4m (Figure 3.7.c). Structures within this are more difficult to discern, compared with the seasonal plot within which local relief is clearly detectable, whereby differences in positive elevation appear in bands (Figure 3.7.a).

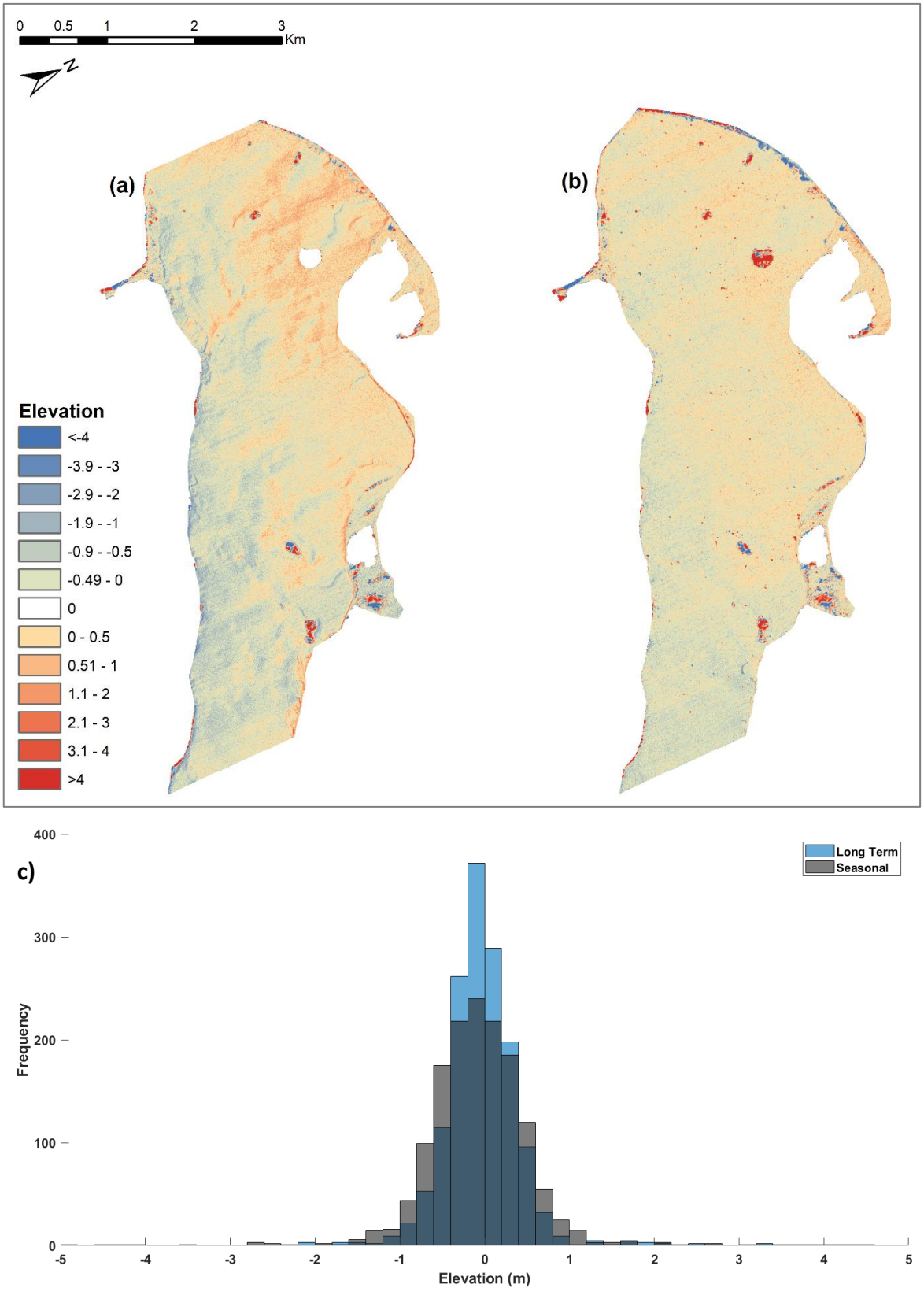

Figure 3.7: (a) Shows seasonal differencing of elevation data for Garry Island between July and September 2016 and (b) long term differencing between Septembers 2011 and 2016. (c) Shows the hypsometry of elevations for these two datasets. ArcticDEM data provided by: Porter et al (2018); PGC (2020a).

3.3.2. Hydrological Patterns

Drainage on Garry Island corresponds with bands of positive elevation change, typically on the order of ~1m to 2m (Figure 3.8.a.). Generally, the drainage lines are located south of these features, along elevation changes of ~-0.5m in the north and ~0.5m in the south (Figure 3.8.a.). A cross-section through one gully shows that the peak in measured change in elevation (1.6m) coincides with the peak slope value (6.9º) in 2017, with elevation change decreasing with distance towards one of the lowest points (0.7º) (Figure 3.8.b.).

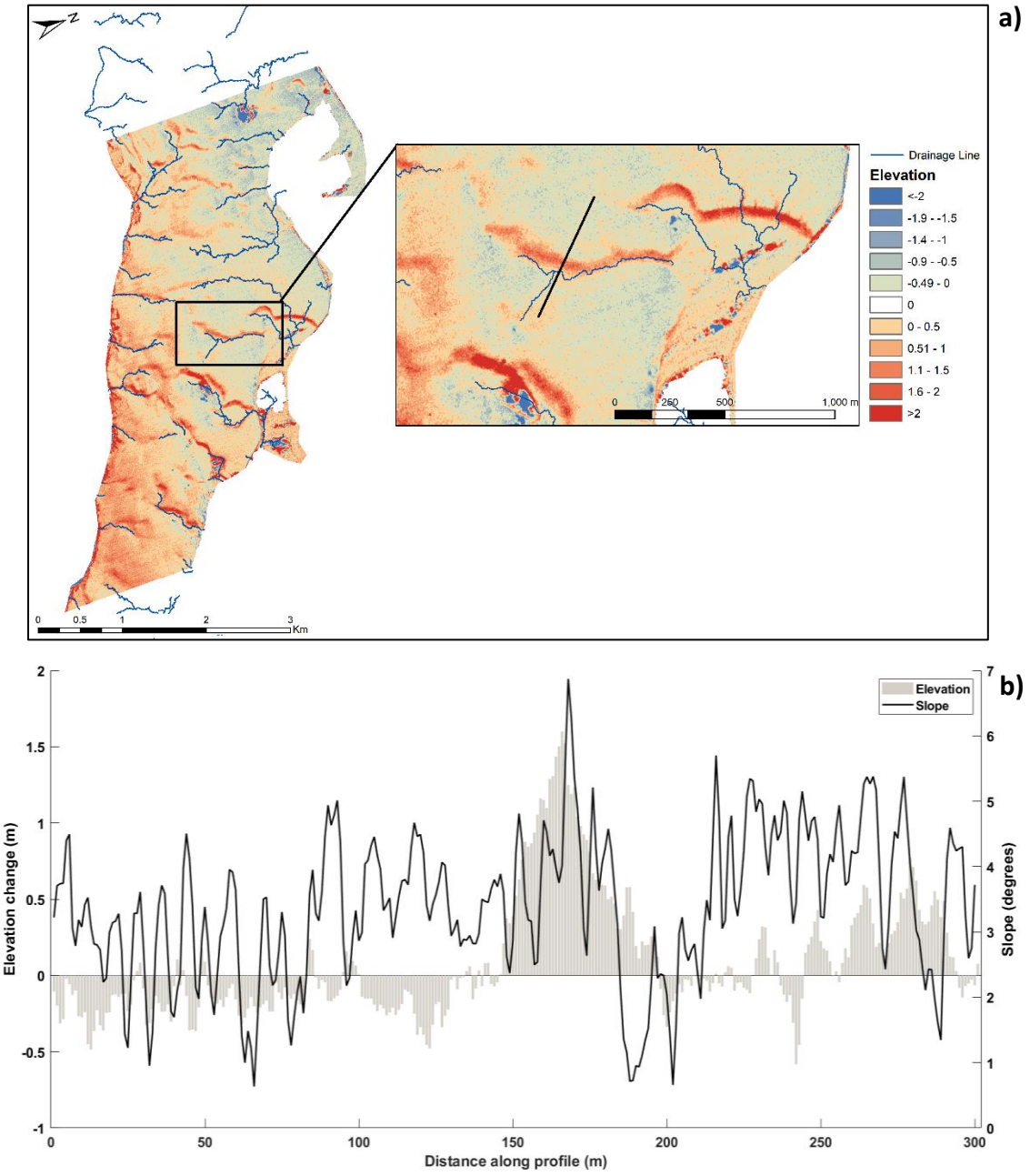

Figure 3.8: (a) Shows drainage lines overlaid onto an elevation difference map of Garry Island from September 2016 to May 2017. The insert map identifies one of the gullies. (b) Shows a transect taken across the previously identified gully, showing the observed elevation change (2016 to 2017) and slope (2017) at this site. Spatially coherent patterns of noise (as seen in the insert map of 3.8.a) are likely attributable to large water bodies such as lakes. ArcticDEM data provided by: Porter et al (2018); PGC (2020a).

3.3.3. Snow Distribution

The outputs of the shelter index show that northeasterly winds (the prevailing wind direction) produces bands of high shelter, predominantly on the western side of the island (Figures 3.9.c and 3.9.d). These correspond with localised areas of positive elevation difference (Figure 3.9.a) and with snow present within Sentinel Imagery (Figure 3.9.b). Northeasterly winds produce slightly more extensive areas of high shelter than east-north-easterlies (Figures 3.9.c and 3.9.d). Where elevation change in the highlighted gullies is ~2m (Figure 3.9.a.), shelter values of ≥0.8 are observed (Figure 3.9.d.).

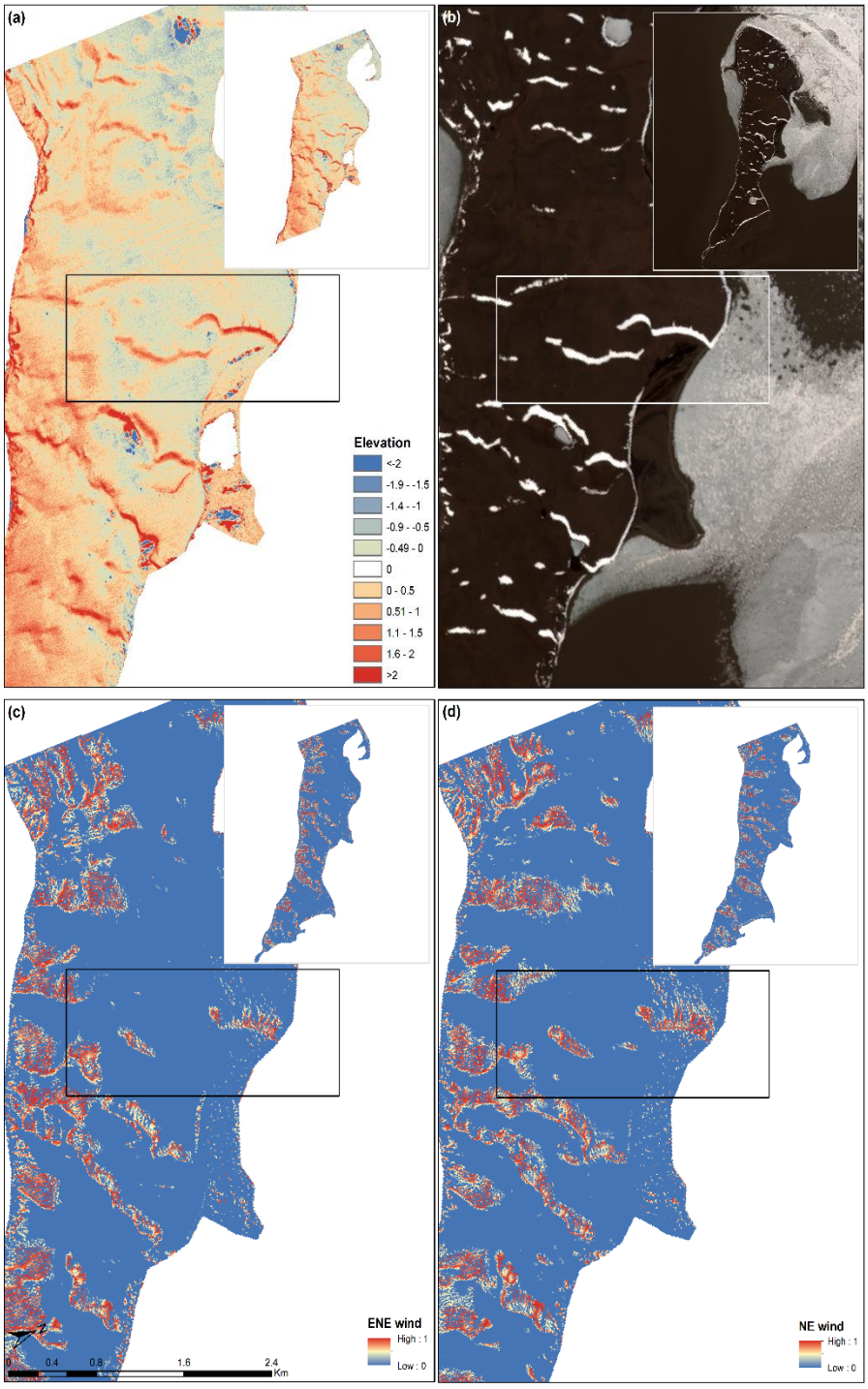

Figure 3.9: (a) Elevation differencing between September 2016 and May 2017; (b) Sentinel 2 Imagery from June 2017 showing snow accumulation; (c) and (d) snowblow modelling results. ArcticDEM data provided by: Porter et al (2018); PGC (2020a). Sentinel 2 Imagery provided by: European Space Agency (2020).

3.3.4. Local Site-based Analysis

3.3.4.1. Site 1 (Garry Island - north)

The average elevation, whilst variable over the time period, still exhibits some clear trends (Figure 3.10.a). 2016 shows a significant increase in elevation between mid-summer (July) and the very end of summer (September) whereby the elevation has increased by 6%. During 2015, the elevation increases by more over 4 days (2.7%) than the decrease over 7 months in 2013 (1%). The average rate of change over the entire time series is -0.08 m/yr, with an average of 0.5m of lowering between 2011 and 2017.

At Drinking Lake, 99% of the measured change is less than or equal to ±2m (Figure 3.10.b). Within this there are spatially coherent trends whereby there is positive change at lower elevation and negative change at higher elevation. The main band of change occurs between 0m and -1m, at initial elevations between -5m and 15m, distinguishing these as areas of surface lowering. Whilst at the beginning of the plot the initial elevation is consistently negative (despite increasing by ~3m), elevation change drops from 1.3m to -2.2m (Figure 3.10.c). A more pronounced negative trend exists towards the latter half of the data. At initial elevations of ~2m, elevation change measured ~4m, whereas at the tail end, changes as low as ~-5m were recorded at initial elevations of ~16m (Figure 3.10.d). Artefacts in the data are clearly apparent such as at 7m initial elevation where elevation change in consistently negative (Figure 3.10.b).

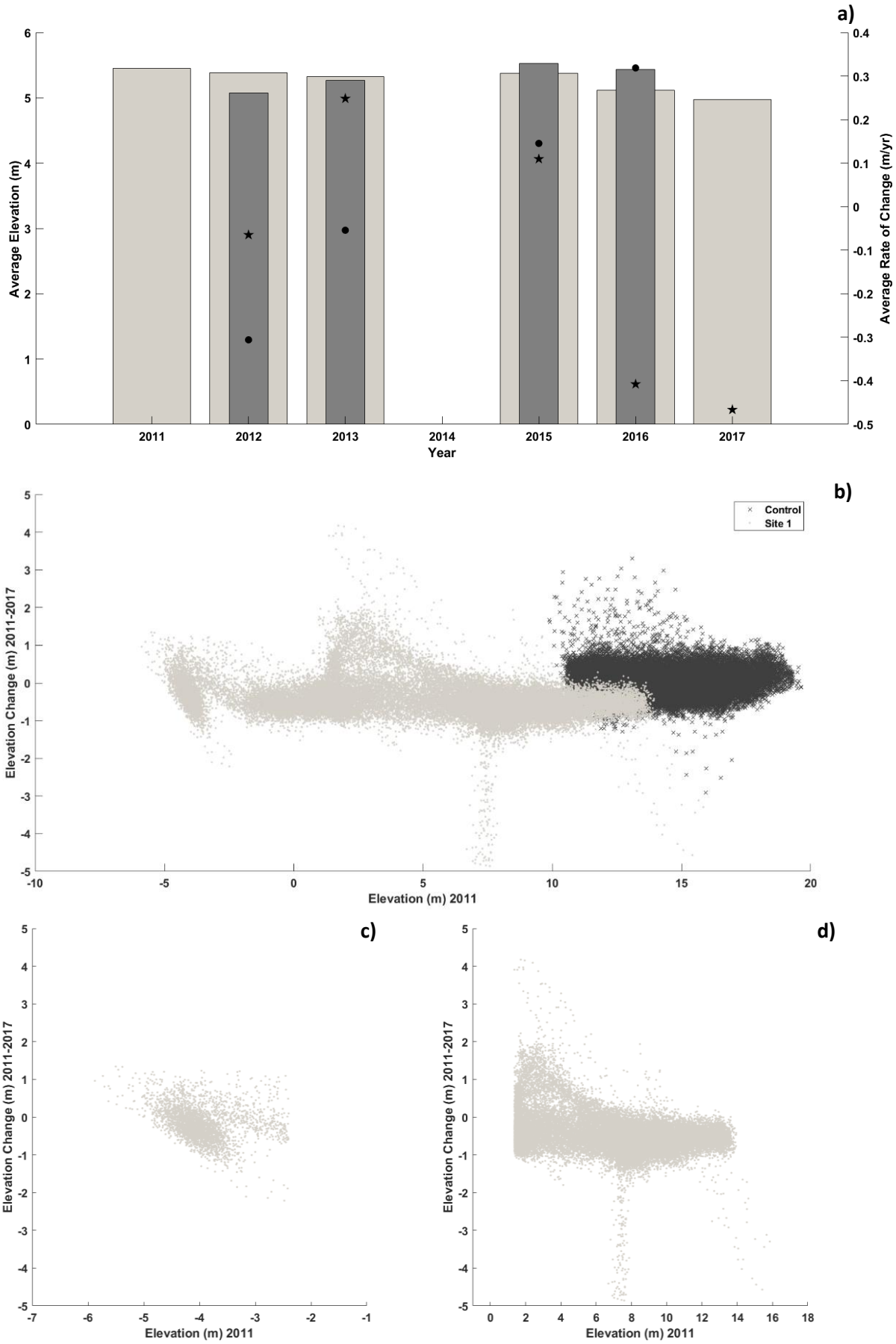

Figure 3.10: (a) The left axis plots a bar graph of average elevation per year. The right axis shows the average rate of elevation change between each date within the time series. The darker bars and circle symbols represent a second month within the year. (b) Scatter plot of long-term elevation change compared with the initial elevation in 2011, with the control site for reference. (c) and (d) show specific trends identified from (b). ArcticDEM data provided by: Porter et al (2018); PGC (2020a).

3.3.4.2. Site 2 (Garry Island - middle)

With the exception of 2012, average elevation varies by 0.4m, with the highest and lowest elevations recorded in 2013 and 2016 respectively (Figure 3.11.a). The average rate of change between 2011 and 2012 is the largest across the time series, with a value of -0.6 m/yr, compared with an average rate of 0.02 m/yr across the entire time series. Intra-annual change varies by no more than 0.2m over the 2013 to 2016 time period. However, this change doubles within 2012 such that at its lowest point, average elevation in June 2012 is 0.9m lower than April 2013.

Elevation change at the middle site on Garry Island is densest between 1m and -1m, with some of this change extending up to 2m between initial elevations of 10m and 40m (Figure 3.11.b). 56% of elevation change over the time series is positive. Between 10m and 30m, elevation change extends from -5m to 5m, often occurring in relatively distinct columns. At ~10m initial elevation, elevation change measured ~5m. This begins a negative trend which can be traced down to ~-5m at initial elevations of ~20m (Figure 3.11.c).

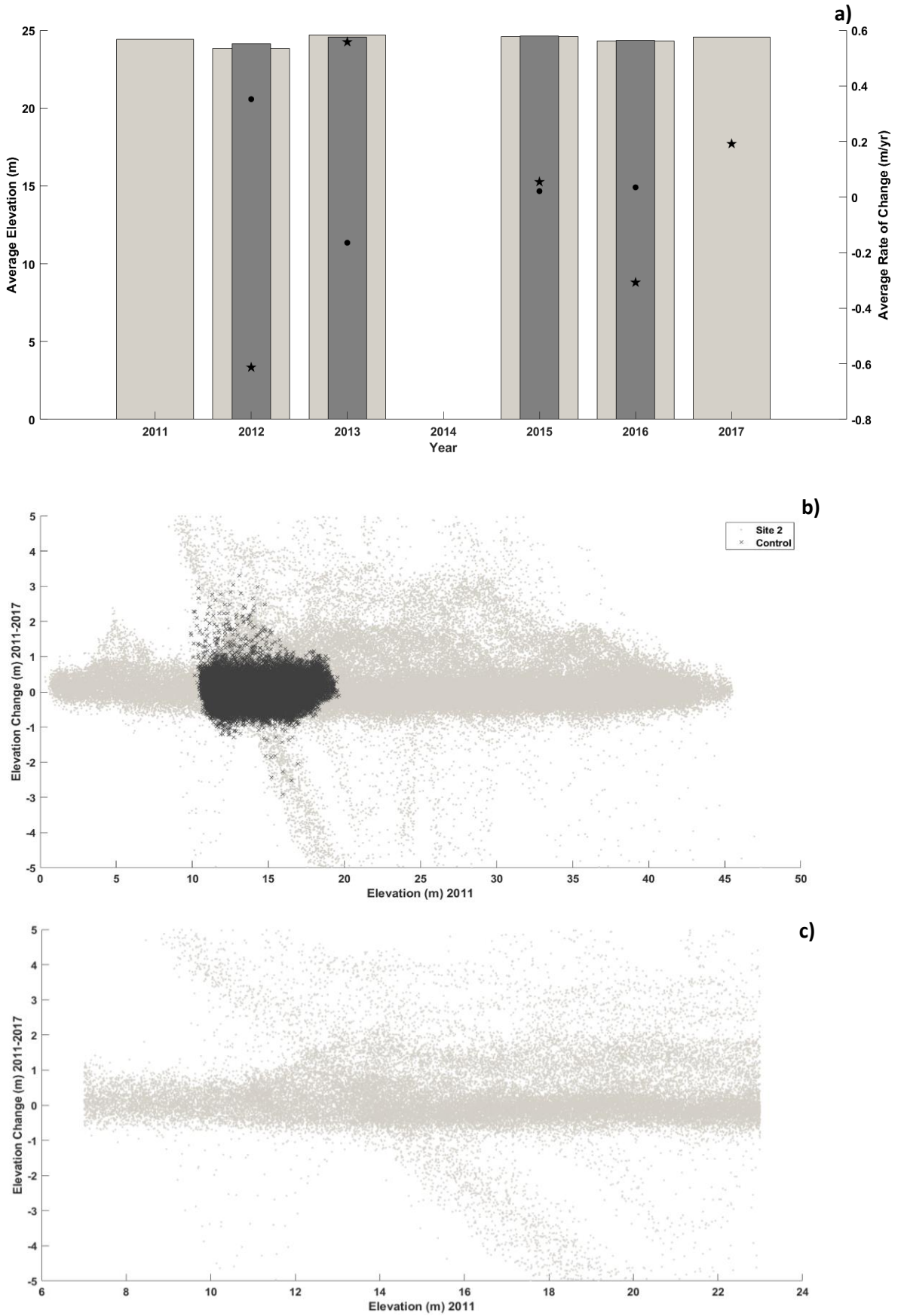

Figure 3.11: (a) The left axis plots a bar graph of average elevation per year. The right axis shows the average rate of elevation change between each date within the time series. The darker bars and circle symbols represent a second month within the year. (b) Scatter plot of long-term elevation change compared with the initial elevation in 2011, with the control site for reference. (c) and (d) show specific trends identified from (b). ArcticDEM data provided by: Porter et al (2018); PGC (2020a).

3.3.4.3. Site 3 (Garry Island - south)

Average elevation remains relatively consistent over the time period, such that the average rate of change over the entire time series is 0.05 m/yr (Figure 3.12.a). The yearly elevation varies by only 0.78m and achieves an average elevation in 2017 which is 0.3m higher than in 2011. Intra-annual differences are greatest in 2012 where an average of 3.4m of change occurs over 4 months.

In the south of the island, elevation change varies, dependant on the initial ground height in 2011 (Figure 3.12.b). For elevations below ~25m, observed change is ±2m, however between 0m and 10m, there is spatial variance around the main area of change. Between 25m and 50m change reduces to half of its former magnitude with less elevation points lying outside of +1/-1m of change. Given these spatial variations across the study site, average change between 2011 and 2017 measured 0.3m. Between initial elevations of 30m and 40m, bands of elevation change can be identified which display a negative correlation. 5m of change has occurred at ~30m, which at ~35m has become negative change of almost the same magnitude.

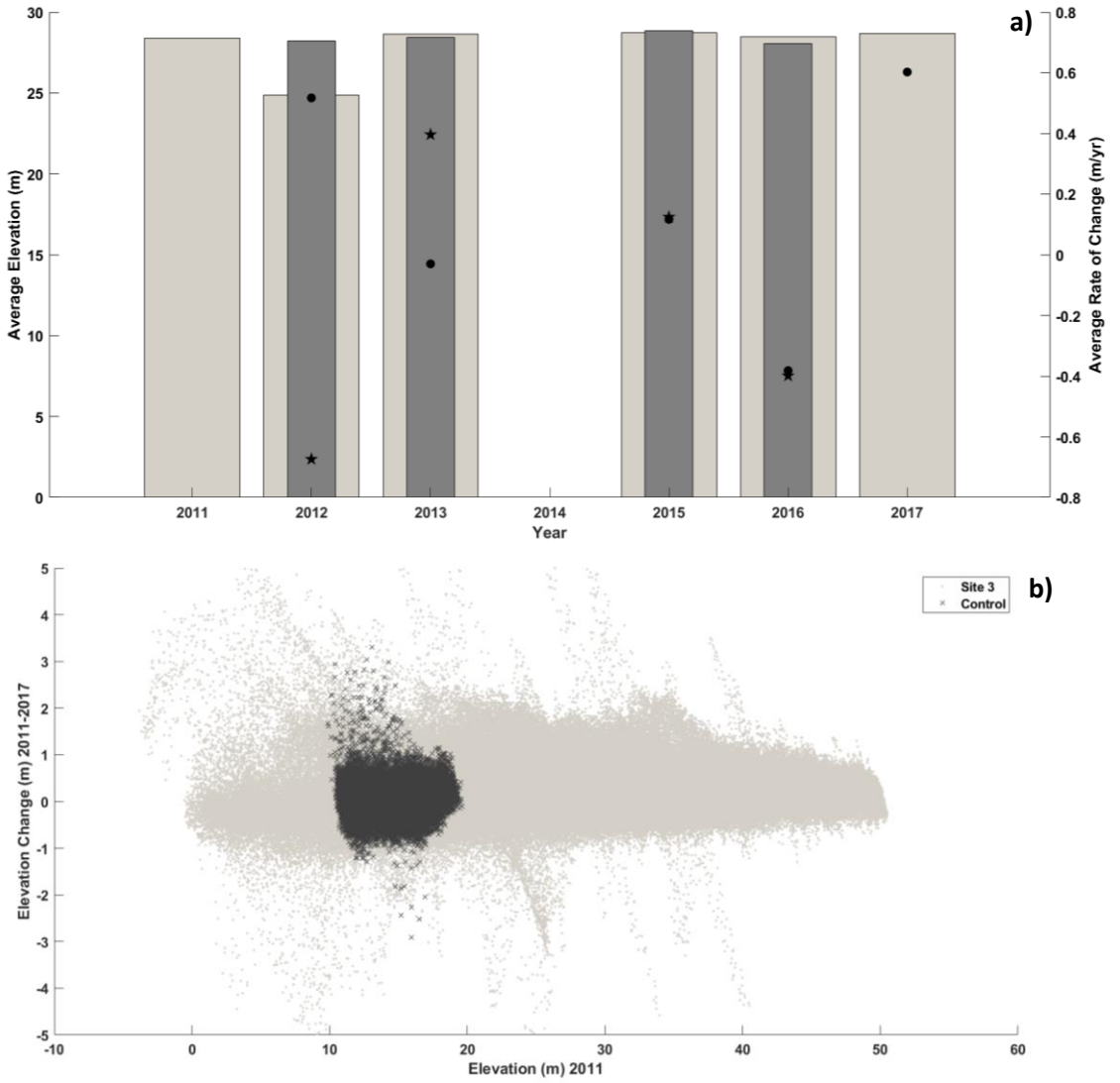

Figure 3.12: (a) The left axis plots a bar graph of average elevation per year. The right axis shows the average rate of elevation change between each date within the time series. The darker bars and circle symbols represent a second month within the year. (b) Scatter plot of long-term elevation change compared with the initial elevation in 2011, with the control site for reference. (c) and (d) show specific trends picked out of (b). ArcticDEM data provided by: Porter et al (2018); PGC (2020a).

3.3.5. Summary of Results

Vertical rates of across Garry island measured 0.03 m/yr, with an average lowering of 0.22m between 2011 and 2017 (Figure 3.6). Seasonal changes between July and September 2016 exhibited greater average elevation differences than variances over the long-term (Figure 3.7). Negative changes of -0.08 m/yr were detected at Site 1 in the north of Garry Island (Figure 3.10) whilst positive changes of 0.05 m/yr were evident in the south (Site 3) (Figure 3.12). Bands of positive elevation change were observed between September 2016 and May 2017, with change on the order of ~2m. These were found to most closely correlate with (1) snow present within Sentinel 2 Imagery from June 2017 and (2) snowblow modelling using northeasterly winds (Figure 3.9).

3.4. Discussion

3.4.1. Negative Elevation Change

Significant negative elevation change is observed on Garry Island over elevations of 5m to 40m (Sections 3.3. and 1.4.2). This may suggest that more widespread degradation of continuous permafrost has been identified which is indicative of regional responses to warming. Negative elevation changes of -0.08 m/yr were observed at Site 1 in the north of Garry Island (Figure 3.10.a). This may reflect transitions from IWs which were previously prone to regular cracking (Mackay, 1974), to those now experiencing greater thawing and subsidence (Burn, n.d). Measured changes indicate that ArcticDEM can detect these thermokarst features, overcoming challenges of assessing smaller-scale features using remote sensing (Jorgenson and Grosse, 2016). ArcticDEM could be invaluable in terms of increasing the spatiotemporal mapping of IW polygons, particularly where they are difficult to observe on hillslopes within the field as the ridges and troughs are truncated by mass movement (Mackay, 1995; Christiansen et al., 2016; Burn, n.d). However, there are some elements which are currently beyond remote sensing capabilities which makes assessments of IW degradation far from comprehensive. (1) the ability to map ground ice; (2) observing differing rates of subsidence between polygon ridges and troughs; and (3) detecting transitional changes between low-centred and high-centred polygons.

The subsidence expressed on the surface which was analysed within this study only allows for estimations of the size of the underlying IW (Morse and Burn, 2013). It is important to understand subsurface changes since melting of excess ground ice is the driving force of subsidence, consequently influencing the magnitude of elevation change (Bode et al., 2008). As well as vertical subsidence, horizontal deformation can occur in the event of thermal contraction cracking (Mackay and Burn, 2002). As the ground seasonally expands and contracts, largely moving material into adjacent troughs and ridges, the extent of measurable change at the surface will differ (Kokelj and Burn, 2004). Small changes in relative elevation (~5 mm/yr) may be attributable to polygon centres, whilst larger declines (~35 mm/yr) are typical of troughs (Burn, n.d). Within ArcticDEM Imagery, this is difficult to determine, as is polygon type. This is important because high-centred polygons sit above larger IWs which are closer to the surface and therefore these features are more susceptible to degradation

(Steedman et al., 2017). Degradation occurs in the troughs, whilst the centres have higher elevations (Steedman et al., 2017). The reverse is true of low-centred polygons which have elevated rims (Liljedahl et al., 2012). 10% of the Tuktoyaktuk Coastlands are characterised by high-centre polygons and therefore these would be expected on Garry Island given that these develop from degrading low-centre polygons (Steedman et al., 2017).

3.4.2. Positive Elevation Change

Positive elevation changes observed within the ArcticDEM differencing and corresponding with gullies on the western side of Garry Island could be interpreted in several ways. Such as: (1) they might reflect positive elevation change as a result of ice growth in the ground (frost heave from massive ice segregation); or (2) they may reflect zones of vegetation growth as previous studies have suggested in other parts of the Arctic. It is argued here that the positive differences are neither indicative of thermokarst activity nor associated fluctuations in vegetation growth, but instead indicate a third mechanism: providing settling points for windblown snow, guided by topographic structure, which has also influenced drainage patterns across the tundra (Mackay and MacKay, 1974; Morse et al., 2012).

Based on field observations and records of subsurface change on Garry Island, there is no evidence for topographic increases as a result of ground ice growth (Burn, n.d). As such, all existing observations point towards subsidence where IWs have been observed over the last two decades (Burn, n.d). Field observations in the NWT and across the High Arctic have determined that warming over the latter half of the 20th century has resulted in less semi-permanent snow, earlier seasonal snow melt and greater IW thaw; therefore initiating drainage downslope (Wahren et al., 2005; Woo and Young, 2014; Burn, pers. comm). Extreme climate warming across Northern Alaska in 1998 caused significant permafrost degradation, resulting in both increased thaw depths and depths to the top of IWs (Wolfe et al., 2000). Consequently, thaw truncation has meant that IWs which had previously been stable for thousands of years saw decreases in secondary and tertiary wedges (Wolfe et al., 2000; Jorgenson et al., 2006).

Wind redistribution of snow over topographic concavities was determined as the most likely cause of positive elevation change on the hillslopes of Garry Island (Morse et al., 2012; Woo and Young, 2014). Across the High Arctic, late-lying snow in the form of snow beds and snowbanks typically persist beyond the duration of the seasonal snow cover (Woo and Young, 2014). Suspected snow beds lying parallel to northeasterly winds were identified within ArcticDEM (May 2017) and Sentinel (June 2017) Imagery, corresponding with the end of the snow season and the beginning of thawing of the active layer (Figure 3.9). These were detectable within ArcticDEM due to the high spatial resolution which has previously impacted the observation of perennial snow within satellite imagery (Fontana et al., 2010). Depths of these snowbanks corresponded with those measured on slopes across the NWT (~0.5m to 1m) with some reaching up to ~2m in this study (Figure 3.9; Lewkowicz and French, 1982).

During Arctic winters these snowblow events occur repeatedly, smoothing irregularities in the ground surface where the snow is deep (Woo and Young, 2014). On Garry Island, snowdrifts have historically been observed to form “sastrugi” due to wind erosion (Mackay and MacKay, 1974). Windblown snow cover is often found on the hillslopes of Garry Island, which in some instances may correspond with the location of polygonal ground (Kerfoot, 1969: Figure 1; Mackay and MacKay, 1974). This is likely to increase the severity of hillslope IW degradation as increased snow depth within the troughs reduces winter cracking (Burn and O’Neill, 2015).

Semi-permanent snowbanks are often characteristic of stream valleys and therefore the density and distribution of snow cover greatly impacts hydrological systems (Woo and Young, 2014). In high latitudes such as the Canadian High Arctic, water tracks in permafrost-dominated soils are under researched, despite indicating patterns of subsurface drainage and water rerouting across non-incised slopes (Gooseff et al., 2013; Paquette et al., 2017). To further investigate the possible role of drainage systems in the development of positive elevation bands, a water routing analysis was performed (Figure 3.8). The results of routing water through Garry Island show that drainage lines are located downslope of the areas of positive elevation. They are suggested to establish where patterned ground has been detected (Paquette et al., 2017). This may suggest rainfall as the cause of surface flow (Lewkowicz and French, 1982). In contrast, where

drainage lines are not present southward of snowbanks, it is likely that the atmosphere is the dominant mechanism of snow loss (Lewkowicz and French, 1982).

If these gully areas were linked in some way to glacio-fluvial processes in polygonal networks, then changes would be expected to take place in the central axis of the gully, as water carves out a pathway along the bed (Godin and Fortier, 2012). The expected morphological result of thermo-erosion would be a distinct u-shaped valley with a negative elevation change at its centre (Godin and Fortier, 2012). However, since many of the channels across Garry Island are meltwater pathways occurring on low-angle slopes, these are not likely to be capable of high rates of erosion (Paquette et al., 2017). In fact, gully cross-sections show that negative elevation change reaches a maximum of ~0.5m on the lower flank of the gully where a water track is located (Figure 3.8.b). Therefore, the likely explanation is that enhanced snow melt contributes to stream initiation as opposed to streams eroding the snow beds; the latter is more typical of temperate environments (Lewkowicz and French, 1982; Woo and Young, 2014).

Snow further impacts hydrological regimes by interacting with vegetation, particularly as the duration of snow cover shortens, allowing for plant productivity to increase (Callaghan et al., 2011). The summer meltwater season further facilitates slope vegetation growth by contributing to surface and subsurface flows (Woo and Steer, 1982; Woo and Young, 2014). Therefore, it is suggested that the positive elevation change located northward of drainage lines could be attributed to vegetation growth. To test this idea NDVI analysis was carried out on Landsat Imagery from June 2017 (Figure 3.13). However, whilst NDVI values were found to be predominantly located in the north and along the western side of the island, in general they were not correlated with the bands of high positive elevation change (Figures 3.13.c.and 3.13.d).

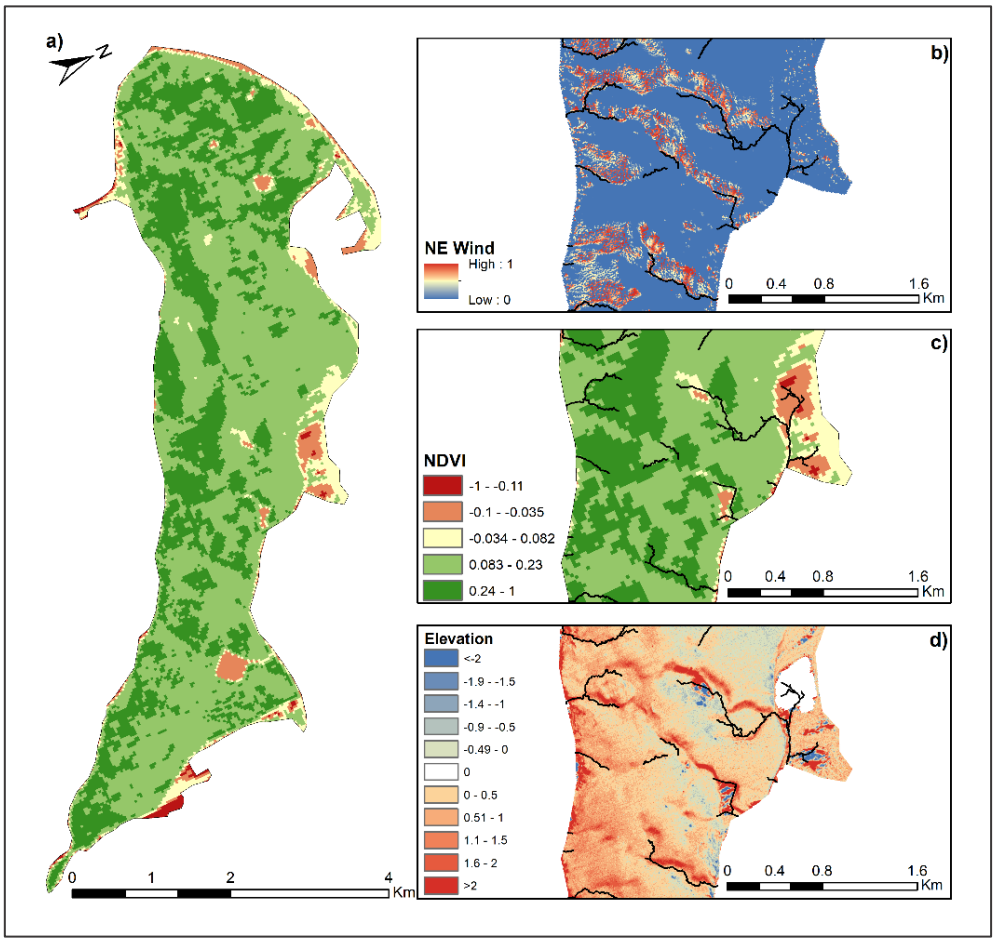

Figure 3.13: (a) and (c) NDVI of Garry Island using Landsat Imagery from June 2017, the closest to the May 2017 ArcticDEM data. (b) Shelter index generated using a snowblow model and northeasterly winds. (d) Elevation change between September 2016 and May 2017 using ArcticDEM. Drainage lines generated for May 2017 ArcticDEM Imagery are overlaid onto panels (b), (c) and (d) for reference. ArcticDEM data provided by: Porter et al (2018); PGC (2020a). Landsat Imagery provided by: USGS Earth Explorer (2020).

The relationship between snow and vegetation also works in reverse; the increased presence of shrubs allows for deeper snow to accumulate which causes temperatures within the winter soil to be higher due to insulation (Sturm et al., 2005). Some of the higher NDVI values (>0.24) along the western side of the island begin to correlate with the areas of high shelter (Figures 3.13.b.and 3.13.c). This suggests that vegetation may be sheltered by the snow over winter, allowing it to survive and continue growing over the summer. Drifting snow tends to surround the shrubs, as well as being located downwind of these areas (Sturm et al., 2005). Snow trapping has significant implications for local ground temperatures as deep snow serves as trough insulation over winter, therefore increasing temperatures and reducing IW cracking (Burn and O'Neill, 2015). Vegetation removal can reactivate IW growth as snow depth is reduced (Burn and O'Neill, 2015).

3.5. Conclusion

Garry Island has been used in order to test the capabilities of the ArcticDEM to detect small-scale hillslope features. Although the accuracy of the ArcticDEM has not been extensively validated with respect to remote sites such as Garry Island, comparison with ICESat observations suggests the ArcticDEM has a vertical precision of <0.5m (refer to Chapter 2, Section 2.3.4) (Morin et al., 2016; Candela et al., 2017; Glennie, 2017). It has proven that signals of vertical change associated with the degradation of IWs are possible to detect at rates comparable to those in the field (Section 3.4.1). Rates of change over the 6-year study period (Figure 3.6) align with in-situ measurements monitored since 2006 in the western Arctic, indicating that thawing is becoming more rapid (Burn, n.d). The broad pattern of change across the island illustrated negative elevation changes of -0.08 m/yr in the north where networks of IW polygons are located. However, whilst signal detection is possible, distinguishing low-centred from high-centred polygons and ridges from troughs is beyond the limits (Section 3.4.1). Positive elevation changes (up to 0.05 m/yr over the ArcticDEM survey period) were unexpectedly found further south. These patterns, which comprised most of the satellite-detected change on the island, point to snow accumulation within topographic concavities which impacts local vegetation and hydrological regimes (Section 3.4.2). This investigation has facilitated the development of an elevation differencing method, validated through in-situ field measurements, which is capable of being applied to larger-scale hillslope thermokarst landforms (implemented in Chapter 4).

Chapter 4

Satellite detection of topographic and morphological variations in active layer detachment slides and retrogressive thaw slumps in the Brooks Range and Foothills of Northern Alaska

4.1. Introduction

This chapter aims to use new high-resolution imagery and digital elevation data to improve our understanding of the large-scale occurrence and small-scale processes of thermokarst mass movement in Alaska, building on techniques outlined and developed within Chapters 2 and 3. Using an existing thermokarst feature inventory (Balser et al., 2015) to validate observations, the chapter presents new findings of thermokarst features. It relates them to topographic and geomorphological variables to quantify the settings in which they are more likely to form. Rates of recent thermokarst feature changes have been estimated which have the potential to be upscaled across larger areas of the Arctic to predict change over the next century. This analysis has revealed that both ALDS and RTS exist on moderate slopes across a range of elevations and aspects, exhibiting positive rates of change in length, width depth and area from 2010 to 2017. Outcomes of this work have wider significance in terms of demonstrating the ability of the ArcticDEM to predict how and where new features may develop as they interact with terrain features, and to estimate the associated impacts on organic carbon release on a regional Arctic scale (Chapter 5, Section 5.2). Alongside findings from Chapter 3, knowledge of hillslope processes at different scales are increased.

4.1.1. Objectives

In order to fulfil the aim of this thesis as outlined in Chapter 1 (Section 1.6), this chapter sets out to investigate the following objectives:

O1*: Quantify statistical relationships between large-scale regional terrain properties, such as elevation, slope, and aspect, and thermokarst feature occurrence using the 100-metre gridded ArcticDEM.*

O2*: Determine small-scale morphometric characteristics of hillslope thermokarst feature types using the 2-metre gridded ArcticDEM.*

O3*: Compare morphometric characteristics from Google Earth Imagery and ArcticDEM to identify rates of change in areal extent over time.*

4.1.2. Study Region

The ~500km wide study region (Figure 4.1) is situated within the mountainous Brooks Range of Northern Alaska, stretching across the North Slope (east-central portion) to Toolik Field Station in the east, and through the Noatak Basin in the west (Balser et al., 2015; Figure 4.1.a.). Elevation within the province (measured at Toolik Field Station) lies at an average of 720 m.a.s.l., with exposed bedrock clearly identifying high elevation points (Bowden et al., 2008; Balser et al., 2015). The zone is classified by Shur and Jorgenson (2007) as “climate-driven, ecosystem-modified”, due to the way in which vegetation accumulation and succession, and physiography interact to produce an ice-rich layer suitable for the development of ALDS and RTS (Shur and Jorgenson, 2007; Balser et al., 2015).

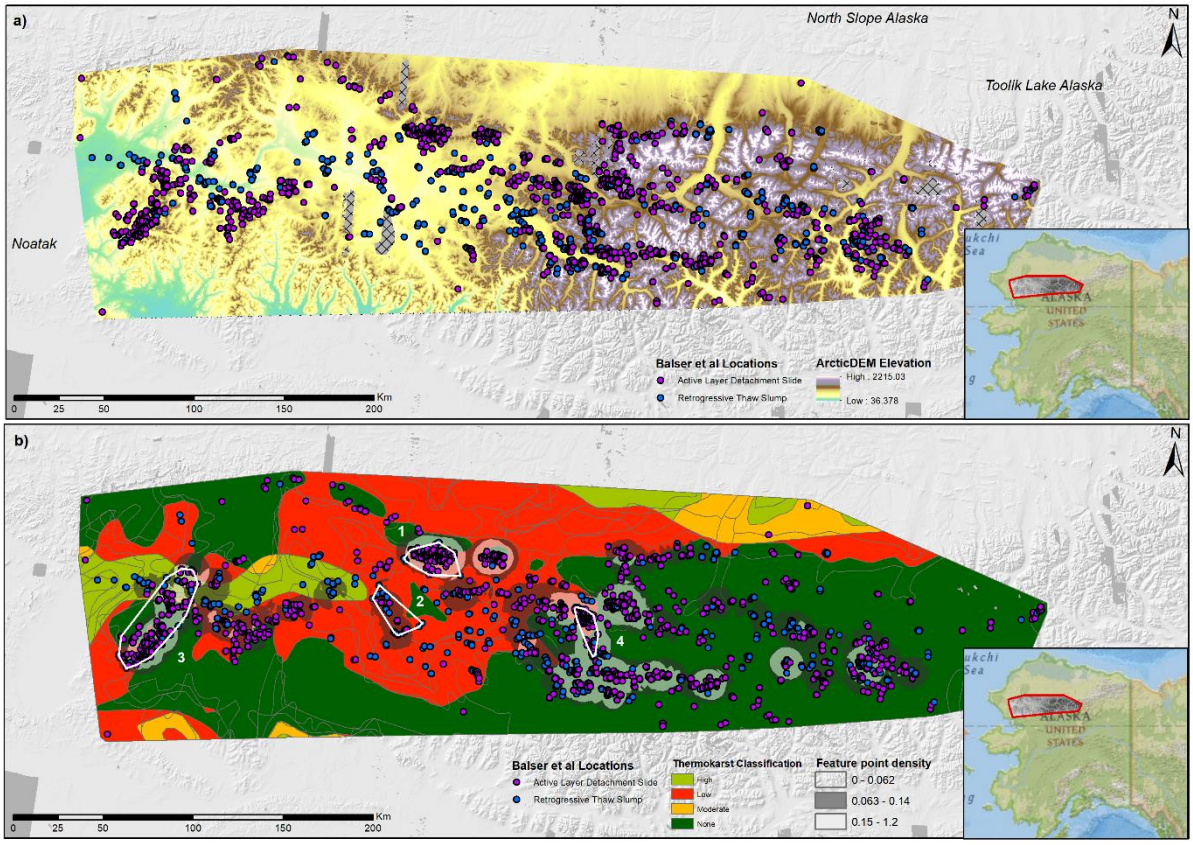

Figure 4.1: a) Elevation map of the study region located within the Western Brooks Range and Foothills of Northern Alaska, overlaid with thermokarst feature locations from a thermokarst inventory collated by Balser et al (2015). Cross-hatching represents areas with no ArcticDEM data. b) Map of the density distribution of Balser et al feature locations in relation to the thermokarst classification map produced by Olefeldt et al (2016). Labelled clusters identify the 4 study sites where density is >0.063 per km^2. ArcticDEM data provided by: Porter et al (2018); PGC (2020a).

4.2. Methods

A brief contextual overview is provided, with detailed methodology described in Chapter 2. Using the ArcticDEM 100-metre mosaic, terrain variables (slope, aspect, and elevation) and northings/eastings were extracted to a thermokarst feature inventory from Balser et al (2015). These were derived in order to investigate potential correlations and statistical distributions within the data. Balser et al (2015) feature locations were investigated within the context of GE Imagery (refer to Chapter 2, Section 2.5.1) which was vital for indicating the spatiotemporal constraints of features, determining detectability using ArcticDEM and defining sub regions of investigation.

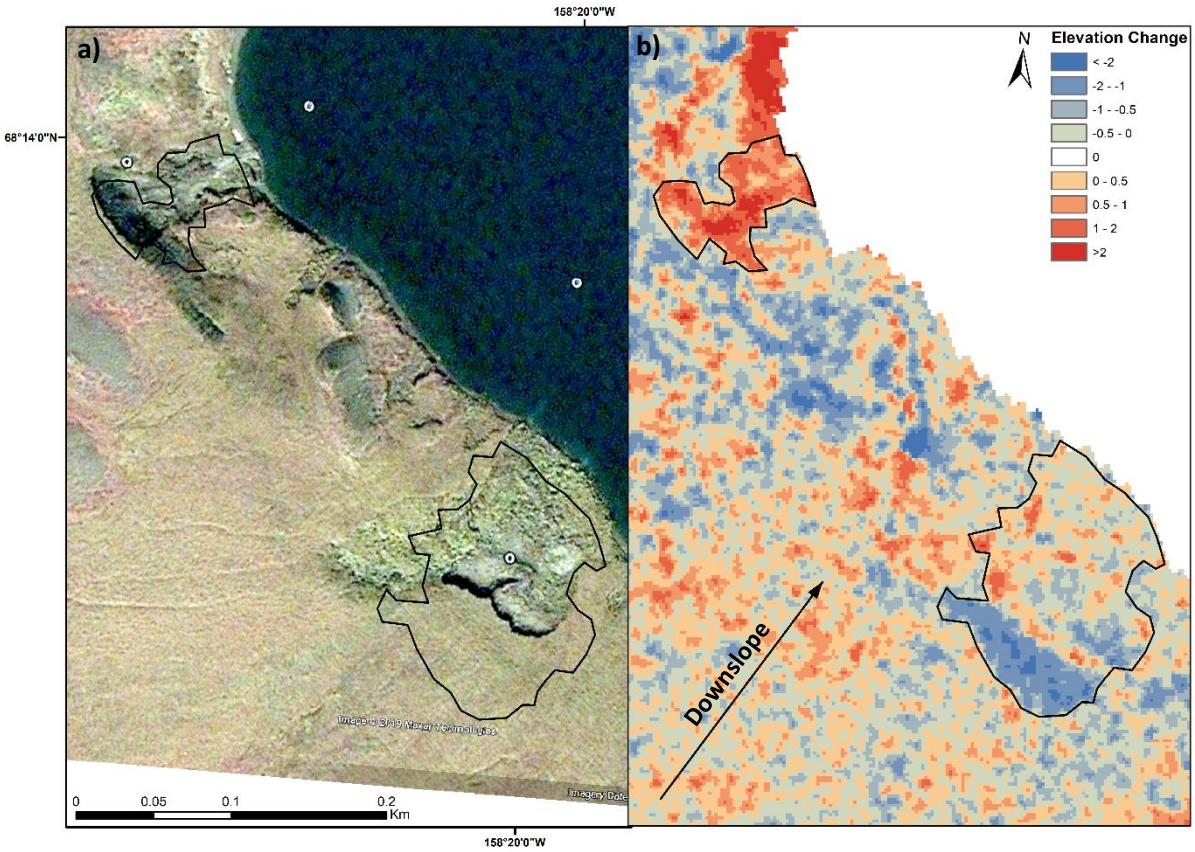

Figure 4.2: Shows how ArcticDEM differencing has been used to derive areas of change. (a) Shows Google Earth Imagery from 2008 of two retrogressive thaw slumps near Feniak Lake in the Brooks Range. (b) Shows elevation change of these two thaw slumps between 2010 and 2017 identified from ArcticDEM differencing. ArcticDEM data provided by: Porter et al (2018); PGC (2020a).

Four sub regions, which collectively encompass approximately one third (32.5%) of the total number of Balser et al (2015) feature locations, were selected based on the highest density of features calculated within a circle neighbourhood with a radius of 100km (Figure 4.1.b). Additionally, sub regions were selected which represent the full diversity of the terrain, distributed over an average elevation range of ~700m at latitudes of 67/68ºN (Table 4.1). Feature densities at Sites 1, 3 and 4 were >0.15 features per km^2, whist at Site 2 density was >0.063 features per km^2. GE Imagery and 2-metre resolution ArcticDEM tile pairs obtained at each location (Appendix B, Chapter 2, Section 2.3.3) were aligned by georeferencing the former to the latter using Balser et al (2015) GPS points. 2008 GE Imagery was consistently used across all 4 sites, however the time series of ArcticDEM tiles pairs differed between the sub areas investigated within each site. RMSE values (Table 4.1) were calculated for each overall site based on Equation 2.2 (Chapter 2, Section 2.5.1). Following methods developed for Garry Island (Chapter 3) techniques to correct for bias and difference elevation were undertaken (Figure 4.2), details of which are found in Chapter 2, Section 2.3.

Table 4.1: Sub regions selected for in depth analysis detailing: the number of features present; the average elevation; the average latitude; and the RMSE by site location, calculated by deriving an RMSE of all locations within a site.

	Site 1	**Site 2**	**Site 3**	**Site 4**
Number of features recorded by Balser at al	423	64	319	266
Mean Elevation	615 *(± SD 72.5)*	300 *(± SD 22.97)*	476 *(± SD 128.60)*	970 *(± SD 95.7)*
Mean Latitude	68.26	67.95	67.78	67.96
RMSE	1.60	1.07	3.00	7.35

Analysis undertaken in this study region and presented below adds quantitative data to the Balser et al (2015) thermokarst feature inventory using high-resolution ArcticDEM tiles to derive geomorphological changes (Section 4.3). Geomorphological mapping of features within both datasets involved spatial delineation through which new features were discovered that are not recorded in the Balser et al (2015) study (Section 4.3.8). Morphometric analysis was semi-automated with length derived as a function of a convex hull and minimum bounding geometry, and width as the doubled distance from an unsplit centreline to the feature edge. Depth was subsequently calculated as the mean value from three transects along the straight-line length. The above techniques for identifying thermokarst landforms are explained in more depth in Chapter 2, Section 2.5.2.2.

4.3. Results

The reported results address two different spatial scales, based on 2-metre and 100-metre resolutions of ArcticDEM data. At 100 metres, topographic variables have been investigated and at 2 metres, geomorphological analysis has been conducted.

4.3.1. Large-scale Topographic Variability of Thermokarst-Affected Terrain

Regional distributions of certain types of slope failures and the potential controls of large-scale topography on their occurrence were investigated. Locations of known failures provided by Balser et al (2015) were correlated with values of elevation, latitude and slope extracted from the 100-metre gridded ArcticDEM.

Hypsometry was first analysed in order to assess the elevations at which ALDS and RTS occur. The resulting hypsometric curve (Figure 4.3.a) shows a bimodal distribution for ALDS, with two distinct peaks in frequency at 600m and 900m. RTS occur at similar frequencies across the elevation range. Slope values for both sets of features (Figure 4.3.b) display similar patterns, with the highest frequencies between 4^{o} and 10^{o}, and tailing off above this. Six Balser points were excluded from Figure 4.3 since no extractable ArcticDEM 100-metre mosaic data exists at these locations.

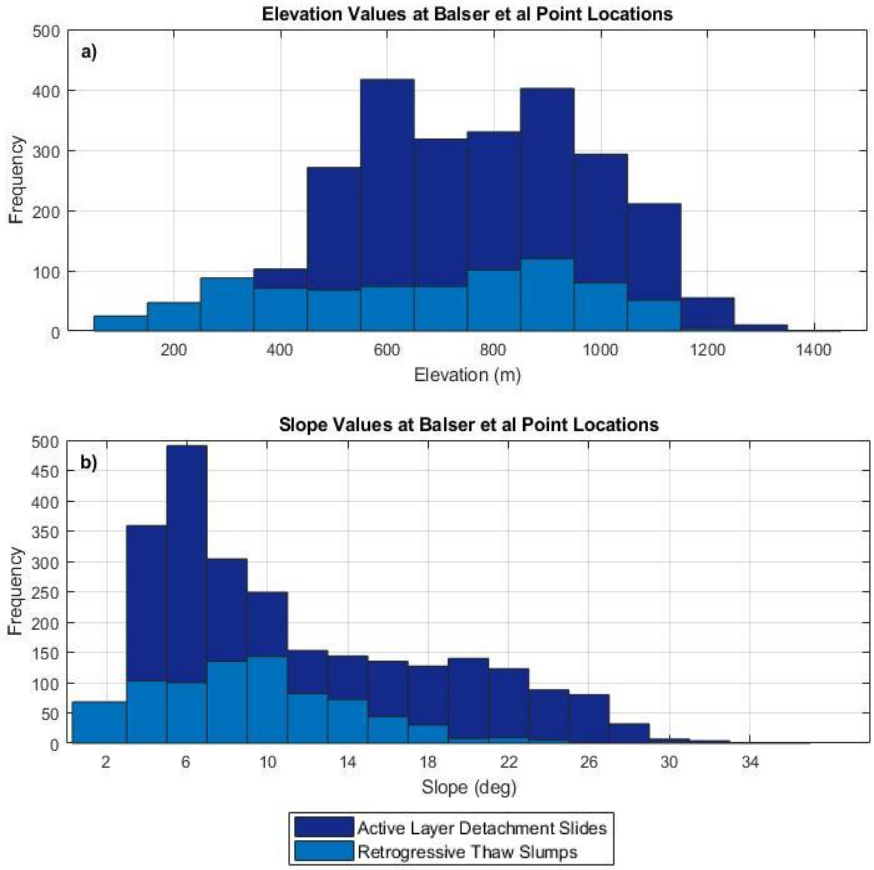

Figure 4.3: a) Hypsometry and (b) slope angles extracted to Balser et al (2015) feature locations using ArcticDEM 100-metre mosaic data. ArcticDEM data provided by: Porter et al (2018); PGC (2020a).

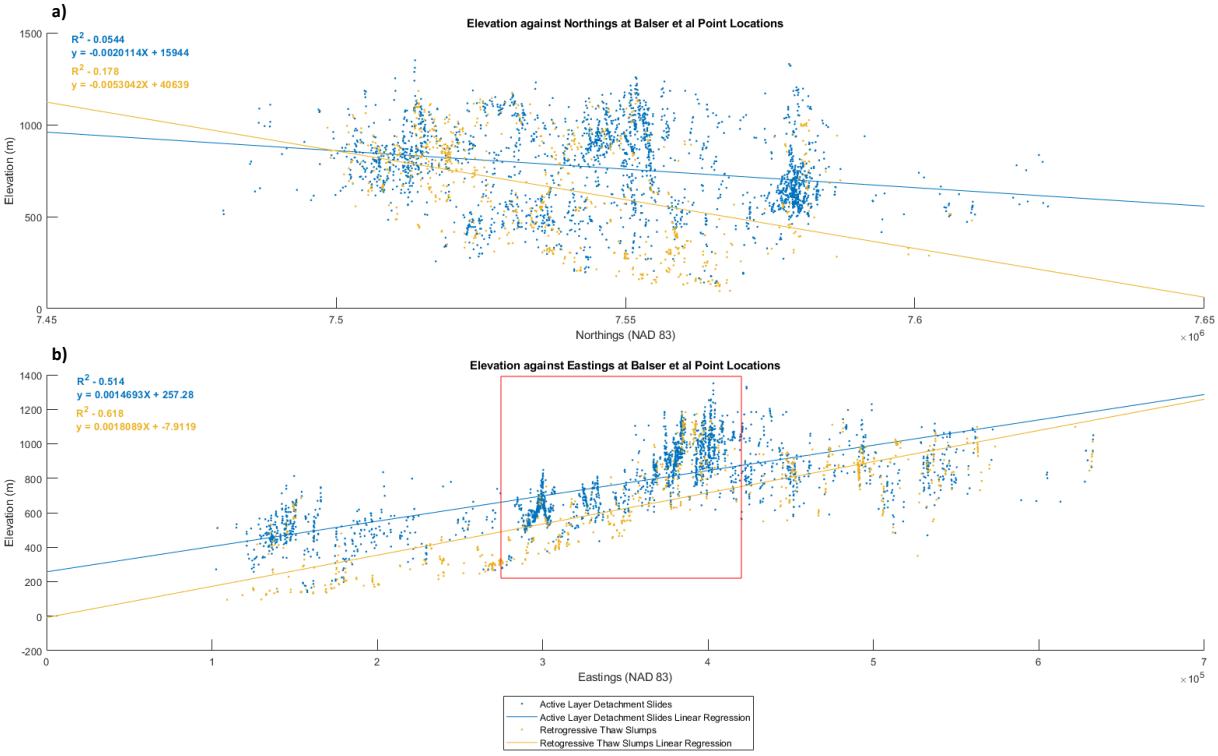

Figure 4.4: Scatter plots of elevation against (a) northings and (b) eastings for active layer detachment slides and retrogressive thaw slumps, using the North American Datum of 1983, UTM Zone 5N. ArcticDEM data provided by: Porter et al (2018); PGC (2020a).

The role of latitude in determining where failures occur was subsequently assessed. The results show a weak negative correlation (ALDS R^2 = 0.05; RTS R^2 = 0.18) between northings and elevation whereby the variance in elevation cannot be explained by difference in latitude (Figure 4.4.a). However, there is a more significant positive correlation between eastings and elevation, with elevation shown to increase in an easterly direction across the study region (Figure 4.4.b). A moderate correlation is observed within RTS which when focussing on a subsection of the plot from x= 2.75e+5m to 4.25e+5m, is strongly positively correlated, achieving an R-Squared value of 0.7. A similar value was found for ALDS, meaning that 70% of the variance in both sets of features is due to a change in eastings.

4.3.2. Small-scale Geomorphic Analysis of Failures

Having explored large-scale factors, the 2-metre resolution ArcticDEM is used to investigate processes of failure at individual features in order to analyse spatiotemporal changes. An overview of the distribution and topographic setting of each feature type is presented. For selected features within sites, analysis of size, shape, area, and depth is reported.

4.3.3. Overview of the Distribution of ALDS and RTS

The results show that ALDS characterise 45.61% of the permafrost terrain in a 2061km^2 (total area of Sites 1 to 4) study area compared with 6.40% for RTS (Table 4.2). This reflects the trend across the wider study region (67,204km^2) where ALDS and RTS features represent 3.71% and 1.20% of the landscape (Figure 4.5).

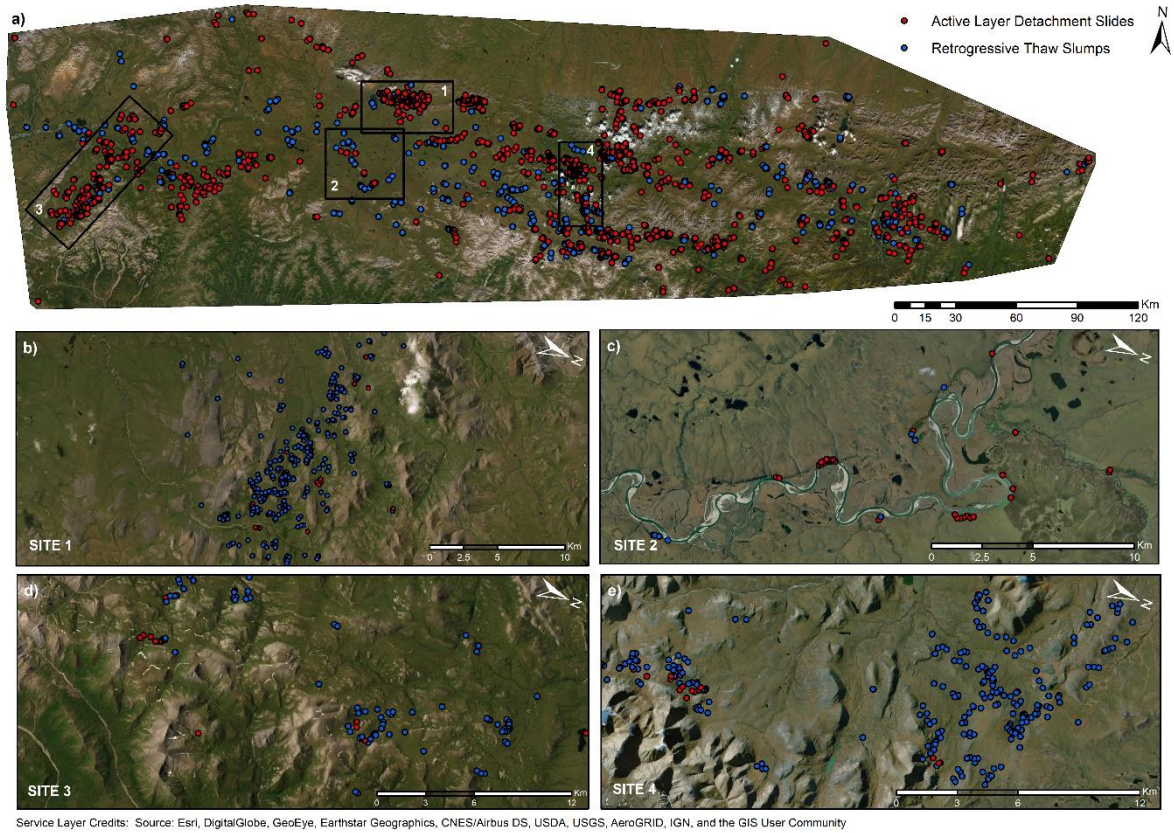

Figure 4.5: Shows the distribution of active layer detachment slides and retrogressive thaw slumps in the context of the topography of the Brooks Range. (a) Shows the total study region, with panels (b), (c), (d) and (e) showing each of the 4 study sites.

Table 4.2: Details the feature type and quantity within each study site and the number which were surveyed in terms of geomorphometry.

Site Number	Area (km^2)	ALDS	ALDS surveyed	RTS	RTS surveyed
1	391	396	5	27	4
2	331	16	-	48	6
3	1149	279	10	40	5
4	190	249	41	17	1

4.3.4. Analysis of the Topographic Setting

4.3.4.1. ALDS

ALDS were observed to occur in clusters around areas of exposed bedrock and meltwater channels (Figure 4.5). The results show that whilst the average elevation for the entire study region is 763.32m, the averages for the 4 chosen sites range from 303.88m to 963.58m. Similarly, for slopes, whilst the regional average is 7.48º, the average range across the sites varies between 6.11º and 10.70º. In Site 4, 16.47% of the features were surveyed (Table 4.2). This site showed the highest feature density, with 1.3 features per m^2 (Table 4.2). The average elevation of those surveyed was 935.38m, with average slope being 5.81º. Whilst the elevation is significantly higher than the study average, the slope is considerably lower.

4.3.4.2. RTS

RTS were found to predominantly be located around larger water bodies on the banks of rivers and lakes (Figure 4.5). The results show that the average elevation for the entire study region is 655.35m. For the 4 chosen sites, the average range varies between 298.85m and 1082.33m. Whilst slope across the entire study region averages at 9.28º, the range across the sites varies between 5.55º and 9.06º. Site 2 showed the largest number of RTS at 14.50% (Table 4.2). Further investigation of 12.50% of these features reveals that the average elevation was 298.38m and slope 9.23º. Whilst this elevation is less than half the average of the entire study region, the slope is closely aligned to the study region average.

4.3.4.3. ALDS and RTS Feature Comparison

The average elevation across the entire study region is considerably lower for RTS than ALDS. Conversely, slope across the entire study region is significantly higher for RTS than ALDS. The range of elevation for the 4 areas is much wider for RTS (298.85m to 1082.33m) than ALDS (303.88m to 962.58m). The range of slope for the 4 areas is slightly wider for RTS (5.55^{o} to 9.06^{o}) than ALDS (6.11^{o} to 10.70^{o}).

4.3.5. Changes in Thermokarst Feature Size and Shape (using ArcticDEM differencing)

4.3.5.1. ALDS

The results show positive rates of change across length and width (excluding Site 2 where no ALDS were surveyed). Across the 4 sites, feature length increased by an average rate of 109.94 m/yr, ranging from 67.20 m/yr at Site 4 to 192.01 m/yr at Site 1. Length increases measured at Site 1 were 1.5 times greater than the average of the 4 sites. The results show a lower rate of change of 25.00 m/yr for width which varied between 13.93 m/yr at Site 4 and 46.97 m/yr at Site 1. Width increases at Site 1 were almost double that of the average across the 4 sites.

4.3.5.2. RTS

The results indicate that across the 4 sites, length increased by 52.67 m/yr. Individual sites show that the rate of increase varied between 23.67 m/yr in Site 4, to 79.53 m/yr in Site 3. The most significant increases in length were observed at Site 3 such that length increased by 50% more than the average across the 4 sites. Width across all 4 sites exhibited a positive annual rate of change of 25.34 m/yr which was smaller than that seen in length. Individual sites varied between 6.29 m/yr at Site 4 and 40.83 m/yr at Site 2. At Site 2, width increased by 61% more than the average across all 4 sites.

4.3.5.3. ALDS and RTS Feature Comparison

The rate of change in ALDS length across all 4 sites is more than double that of RTS. Both ALDS and RTS saw a similar positive rate of change for width across all 4 sites. The relationship between width and length for each feature type is reflected in their differing elongation ratios (Table 4.3). Whilst ALDS were

observed to be longer and narrower with an average cross site ratio of 0.2, RTS were observed to be more circular, with an average ratio of 0.5 (Table 4.3).

Table 4.3: Average elongation ratio between length and width of ALDS and RTS features measured at each site in 2008 using Google Earth Imagery.

Site Number	ALDS	RTS
1	0.16	0.43
2	-	0.62
3	0.20	0.49
4	0.23	-

4.3.6. Changes in Thermokarst Feature Area and Depth (using ArcticDEM differencing)

4.3.6.1. ALDS

Observations showed that there was little change in depth across the 4 sites, with a rate of 0.45 m/yr, varying between 0.31 m/yr at Site 3 and 0.73 m/yr at Site 1. At the latter of these sites, increases in depth were 1.5 times greater than across all 4 sites. The most significant change was seen in area across all 4 sites. The observed rate of change was 4930.69 m^2/yr, varying between 2161.42 m^2/yr at Site 4 and 9216.13 m^2/yr at Site 1. The increase in area at Site 1 was approximately 1.5 times greater than the overall average for the 4 sites.

4.3.6.2. RTS

The results show a minimal change in depth which averaged 3.01 m/yr across all 4 sites. Individual sites varied between 0.12 m/yr at Site 4 and 9.29 m/yr at Site 2. The depth increase at Site 2 was more than 3 times that observed over the 4 sites. The most significant change was seen in area at 3551.74 m^2/yr across all 4 sites (excluding Site 4 where depth was not measurable). The rate of area change varies between 1655.32 m^2/yr at Site 1 and 6844.97 m^2/yr at Site 3. The increase at Site 3 measured approximately twice the average across the 4 sites.

4.3.6.3. ALDS and RTS Feature Comparison

A large disparity was observed with respect to depth across all 4 sites whereby the average rate of change for RTS was more than 6 times that of ALDS. Across all 4 sites, the average annual rate of change in area was 38% higher for ALDS than RTS.

4.3.7. Significant Geomorphometric Changes

4.3.7.1. ALDS

Sites 3 (Figure 4.6) and 4 (Figure 4.7) exhibited significant changes in ALDS between GE Imagery from 2008 and ArcticDEM differencing data. Feature 1 in Figure 4.6.b.i. is a 1151m^2 ALDS at an elevation and slope of 495m and 14^o, which was unable to be detected 9 years after it was mapped in GE Imagery. Unlike the rest of the ALDS in this area, this feature has a similar length and width, with an elongation ratio of 0.5. Figure 4.6.c.i shows feature 4 which was present in 2008, whilst Figure 4.6.c.ii shows feature 6 which was only present from 2010 to 2017. The former was found to have an elongation ratio of 0.3, and was located at 446m, on a slope of 6^o. 81m below feature 4 is a Balser et al (2015) GPS point at which no feature was capable of being mapped in this analysis. Figure 4.6.c.ii indicates feature 6, a new feature which has changed in volume by 22%.

At Site 4, Figure 4.7.b. highlights an area where a feature not previously recorded by Balser et al (2015), has been identified within ArcticDEM at a latitude of 68 and longitude of -155.86, ~220m from the nearest mapped feature. The area of this feature, which is located on a slope of ~7^o, spans 2721m^2. In Figure 4.7.c. the dynamic nature of the area is highlighted whereby the feature identified in 2008 divides into 2 features by the difference year (2010 to 2017). The combined area of these is 15% larger than the earlier mapped feature size.

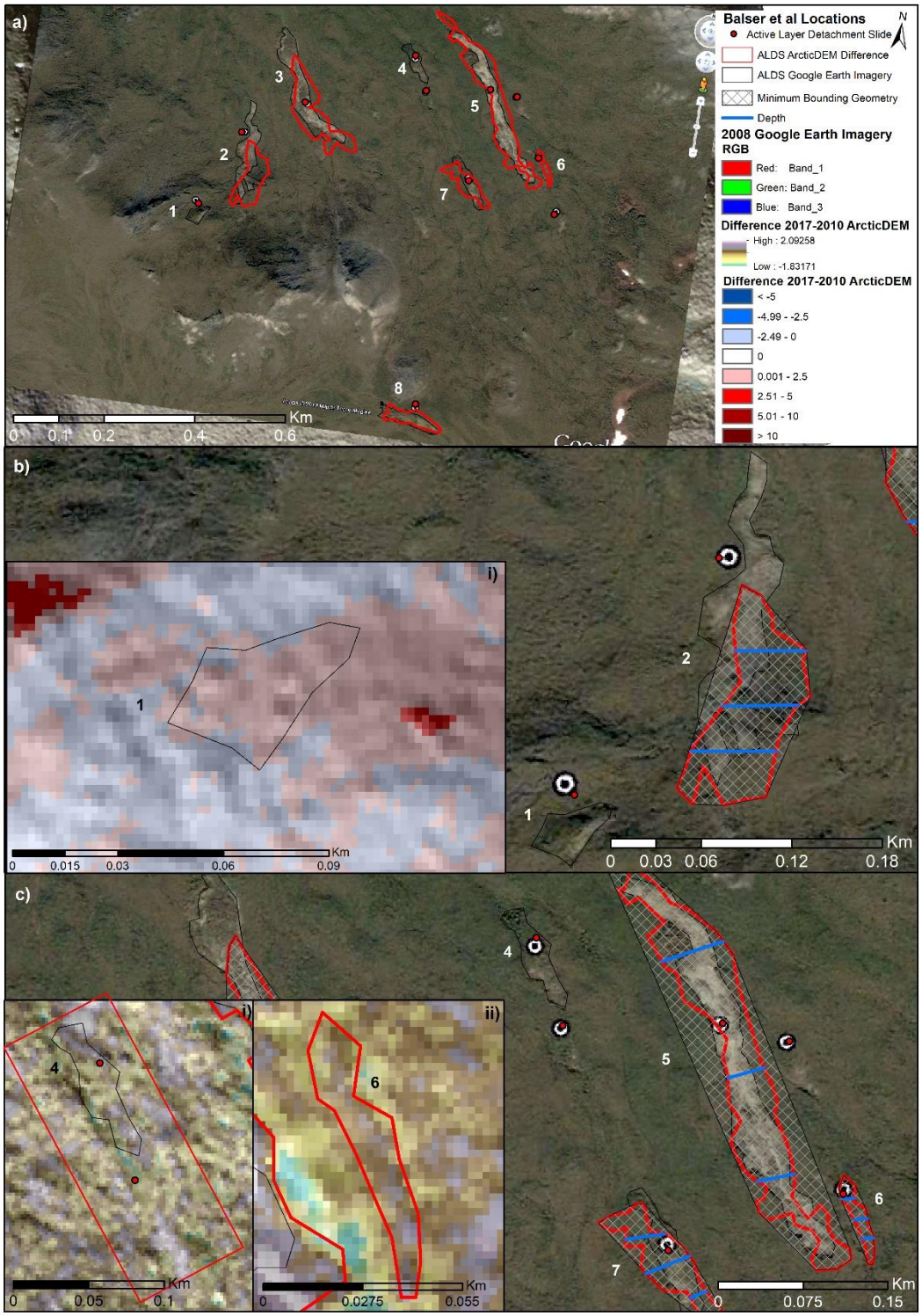

Figure 4.6: (a) Active layer detachment slides identified within Site 3, with both sets of shapefiles displayed on Google Earth Imagery. (b) Identifies a feature detected within the 2008 imagery but not in the later ArcticDEM data from 2010 to 2017. (c) Identifies features detected only in one of the following: 2008 imagery; Balser et al dataset; ArcticDEM difference layer. ArcticDEM data provided by: Porter et al (2018); PGC (2020a).

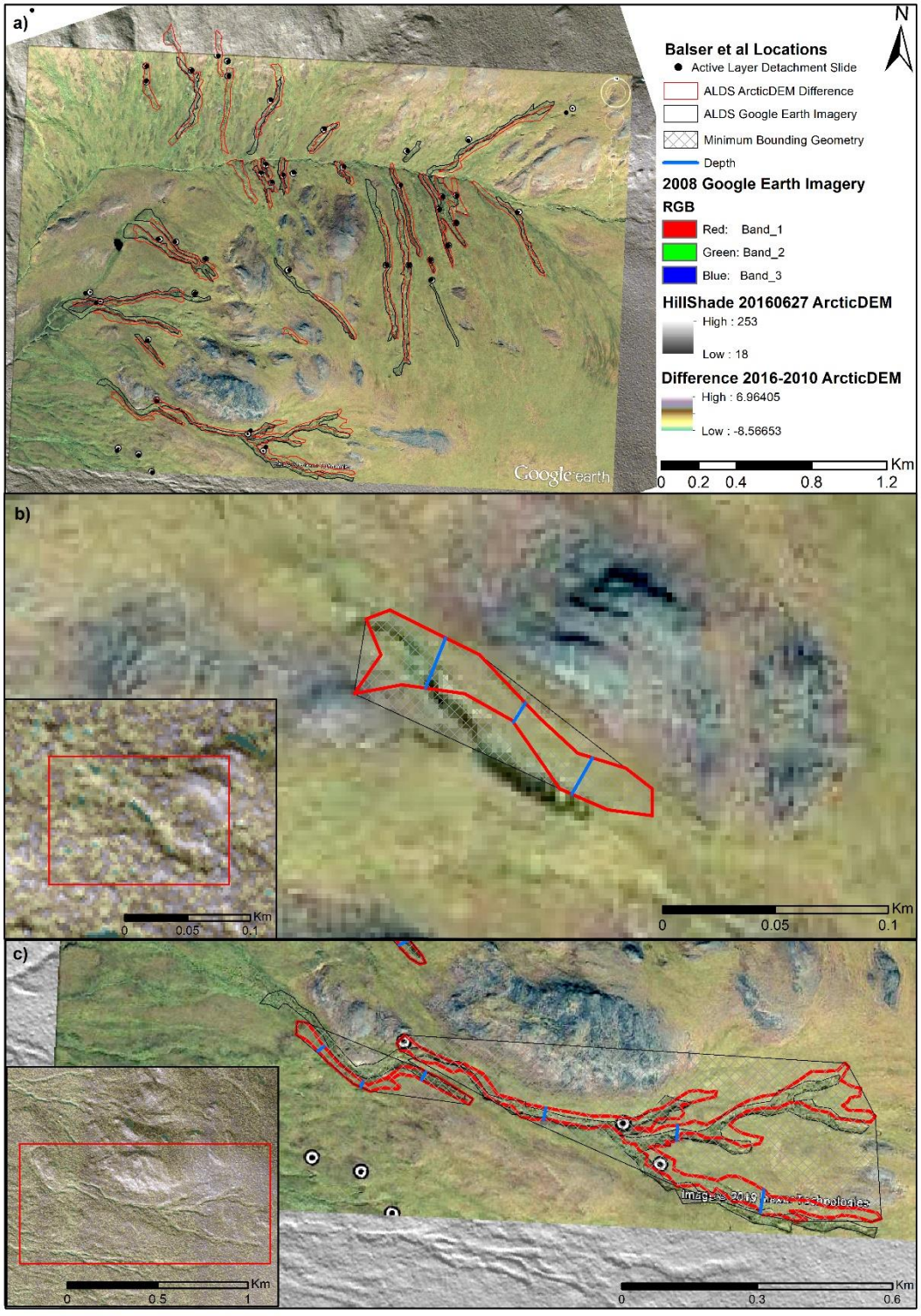

Figure 4.7: Area of active layer detachment slides within Site 4. (b) Identifies a case where a new feature is detected using ArcticDEM that is not present in Google Earth Imagery or the Balser et al (2015) dataset. Panel (c) shows an example of the different ways in which features have evolved when digitised from ArcticDEM. Sub panels highlight features within the main panels in the context of the ArcticDEM difference layer. ArcticDEM data provided by: Porter et al (2018); PGC (2020a).

4.3.7.2. RTS

Notable changes were observed within RTS at Sites 1 (Figure 4.8) and 2 (Figure 4.9), with the latter growing at a faster pace across length, width, depth, and area. In terms of length and width, Site 2's growth was 1.5 times and 3.5 times greater than Site 1. Figure 4.8 highlights two sets of RTS (Figures 4.6.a and 4.6.b) within Site 1 located 19km apart. Figure 4.8.a shows the changing morphology of two features, located on the banks of Feniak Lake, which have expanded inland. The headwall of feature 2 in Figure 4.8.a has incised by ~7.14 m/yr, reflected in a significant length increase of 25.63 m/yr as the slump has retreated. In contrast, Figure 4.8.b illustrates more linear slumps reflected in an average elongation ratio of 0.3, compared with 0.56 in Figure 4.8.a.

Selected features at Site 2 consist of stream associated RTS (Figure 4.9.a). Slumps were found to be near circular in shape, producing an average elongation ratio of 0.59. The centre point of each individual feature has migrated as slumps have advanced downslope. This is particularly evident in features one and two delineated in Figure 4.9.b, where the headwalls have advanced by ~40 m/yr and ~25 m/yr.

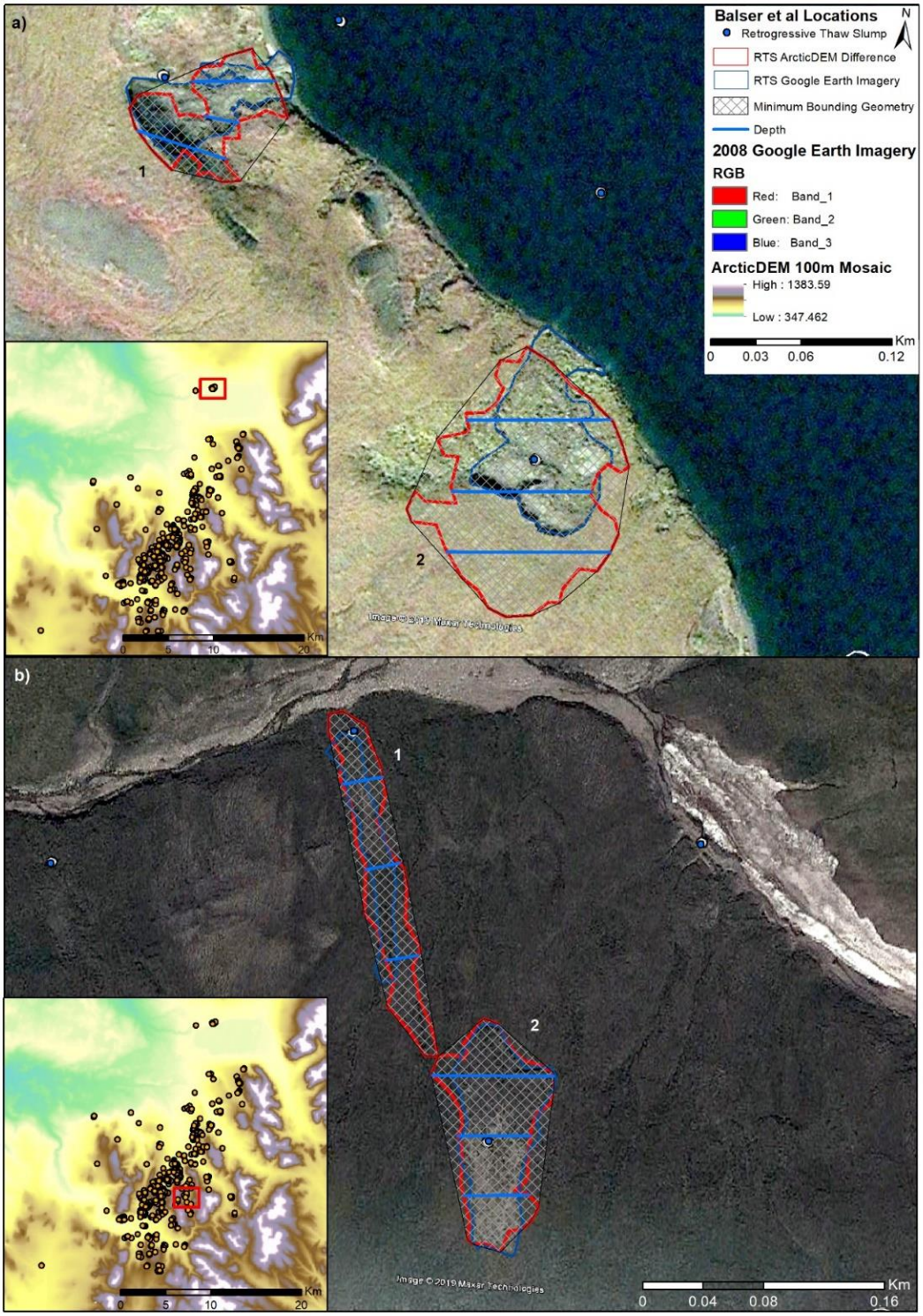

Figure 4.8: Retrogressive thaw slumps identified at a) Feniak Lake and b) inland within Site 1 (locations seen in the insert maps). Features have been mapped as shapefiles using Google Earth Imagery (blue) and differenced ArcticDEM tiles (red). (a) Uses ArcticDEM tiles from June 2010 and May 2017, (b) uses tiles from October 2013 and October 2016. ArcticDEM data provided by: Porter et al (2018); PGC (2020a).

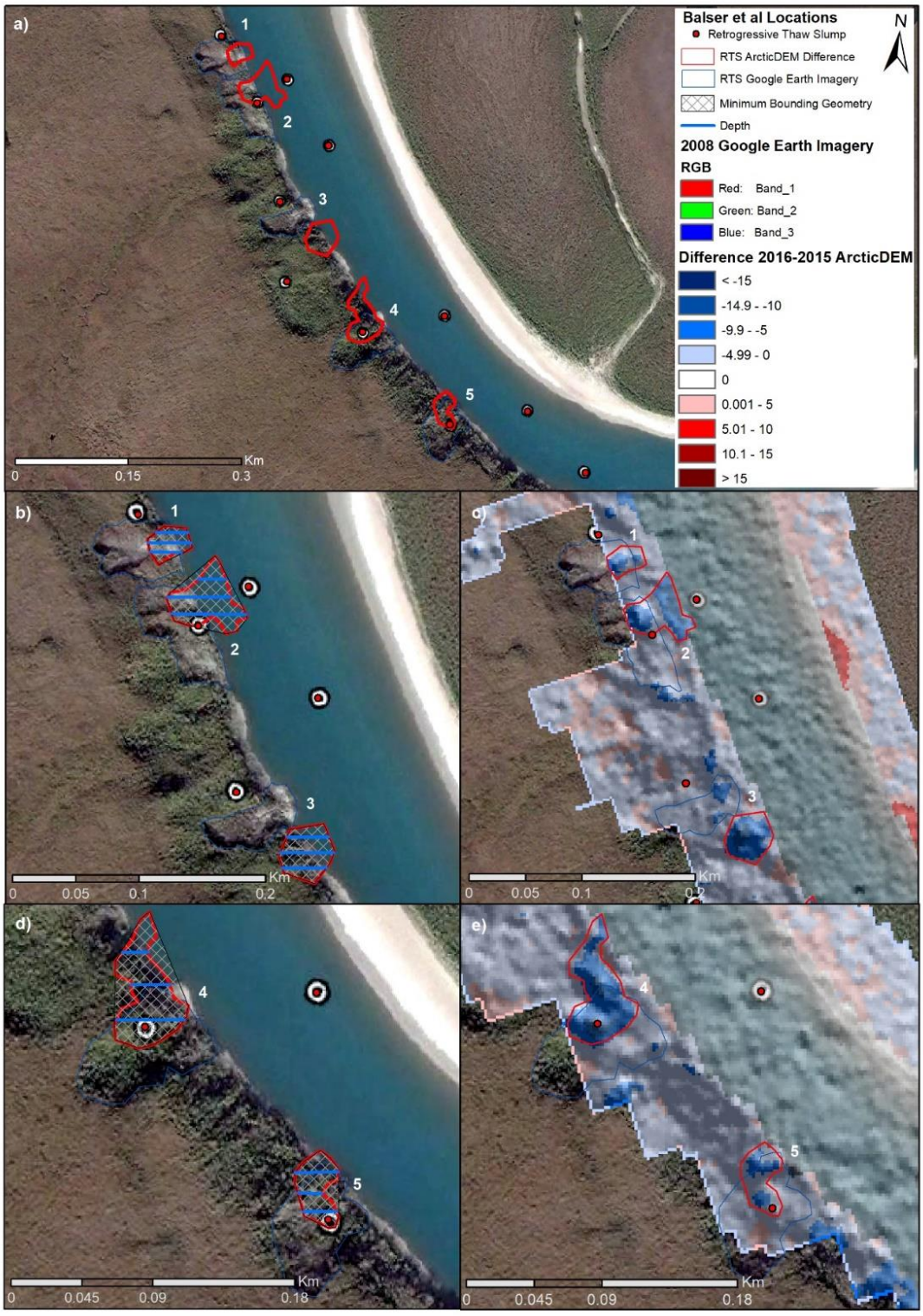

Figure 4.9: (a) A sequence of retrogressive thaw slumps along a river terrace within Site 2, analysed using Google Earth Imagery and ArcticDEM tiles from June 2015 and October 2016. Panels (b) and (c) focus on the upper portion of the stretch, whilst (d) and (e) focus on the lower portion. (c) and (e) show the ArcticDEM difference layer overlaid onto the Google Earth Imagery. ArcticDEM data provided by: Porter et al (2018); PGC (2020a).

4.3.8. Summary of Results

Northerly facing slopes with gradients of ~5º to 20º have generated more failures than regions without these attributes (Lewkowicz and Harris, 2005b; Swanson, 2014). The results of this study show that failures take place across all aspects, with the highest frequency occurring on slopes of 4º to 10º (Figure 4.3.b). At individual sites, averages range from 6º at Site 1, to 10º at Site 3.

Generally, more slumps may be hypothesised to occur in areas of lower latitude and at lower elevations, reflecting the migration of permafrost boundaries. However, the reality is far more complex as a result of topographic and geologic constraints. The region spans a latitudinal band of 67º to 68º, but the west to east elevation gradient exhibits a moderate positive correlation ($R^2 = 0.7$) in the middle portion (Figure 4.4.b). Features are most frequent at elevations of 600m to 900m but were found to initiate at much lower levels at individual sites, ranging from an average of 300m at Site 2, to 970m at Site 4 (Figure 4.3.a; Table 4.1).

Varying magnitudes of morphometric change were observed within each feature type. For ALDS, rates of change across all parameters were positive, with length and area seeing the most significant change, where length increased four times more than width. Similarly, for RTS, the most significant changes related to length and area, however length only increased at twice the rate of width. Across all 4 sites 5 features were only detected within GE Imagery and therefore are suggested to have entered a quiescent phase, becoming revegetated by the difference year (Table 4.4). 6 features were only detected within the ArcticDEM data and therefore are likely to have become active since 2008 (Table 4.4). 6 features were newly discovered which were not previously documented in the Balser et al (2015) database (Table 4.4).

Table 4.4: Details the locations of newly detected features, as well as features which have suspected to have become dormant or recently active.

Site Number	ALDS	RTS	No GPS point	Google Earth only	ArcticDEM only	Latitude/longitude
1	1		1			68.313769/-157.923296
3		1		1		67.56152/-161.773158
3	3			2	1	67.923774/-161.435595
						67.927333/-161.425327
						67.925632/-161.417858
4		1			1	67.849185/-155.748419
4	11		5	2	4	67.847711/-155.752735
						67.850315/-155.750096
						68.015772/-155.86317
						68.00838/-155.855761
						68.043973/-155.980491
						68.017385/-155.841798
						68.009654/-155.836676
						68.019899/-155.87569
						68.021737/-155.866976
						68.01916/-155.865694
						67.847386/-155.750797

4.4. Discussion

4.4.1. Regional Controls on Thermokarst Feature Distribution in the Brooks Range

Analysis of thermokarst feature distribution within the context of topographic variables has shown that feature formation is highly varied across the region's terrain. Features can initiate at elevations of 95m to 1350m, slopes of 0.3^{o} to 32^{o} and occur at equal frequencies (~20% to 30% frequent) across all aspects (Figure 4.3; Table 4.5). This suggests that additional wider processes may be responsible for the observed regional trends. Climate spans three divisions (Figure 4.10.a.) and interacts with the terrain to exert a strong control on the distribution of thermokarst features (Wendler et al., 1974; Sousanes and Hill, 2017). It is highly variable across the region due to anomalously warm patterns of ocean and atmospheric circulation; particularly observed between 2014 and 2016 which falls within the ArcticDEM 2010 to 2017 analysis period (Wendler et al., 1974; Sousanes and Hill, 2017). Changes have propagated below ground such that average annual end-of-season thaw depths increased by 0.64cm between the two decades (Figure 4.10.b). Thaw depths reached highs of ~56cm in 2007, 2010 and 2016 (Figure 4.10.b). These dates approximately coincide with the obtained GE Imagery, and the start and end points of the ArcticDEM differencing period.

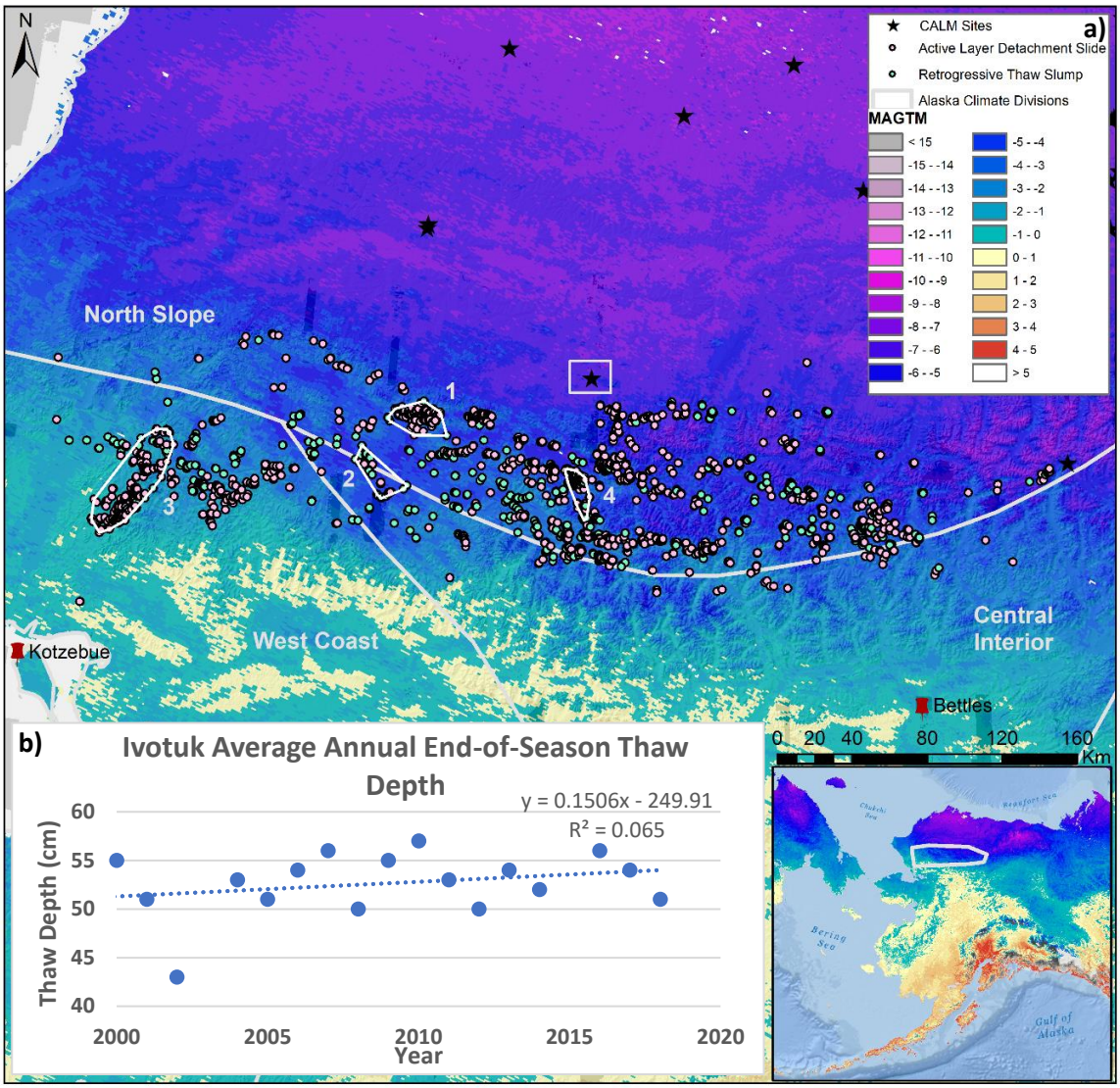

Service Layer Credits: Sources: Esri, GEBCO, NOAA, National Geographic, Garmin, HERE, Geonames.org, and other contributors. Source: PGC, UMN, Esri. Esri, Garmin, GEBCO, NOAA NGDC, and other contributors

Figure 4.10: (a) Shows the Balser et al (2015) thermokarst feature inventory and associated study sites (as numbered) in the context of: Alaska climate division boundaries defined by Bieniek et al (2012); 2000-2016 modelled mean annual ground temperatures by Obu et al (2018); and CALM data accessed through the program's website (https://www2.gwu.edu/~calm/). CALM data which falls within the study area is highlighted by a white box. Red pushpins identify the two nearest climate stations. (b) Shows thaw depth measurements for CALM Site U26 Ivotuk 1km Grid, located within the Brooks Range study region on the North Slope of Alaska and highlighted within a white box in Figure 4.10.a.

Latitude exerts a strong control on Arctic climate patterns by limiting the transmission of solar radiation per unit area (Bieniek et al., 2012; Sousanes and Hill, 2017; Mithan, 2018). Since the locations within this study are within a tight latitudinal band (67º to 68º) north of the Arctic Circle, correlations between latitude and elevation are weak (Sousanes and Hill, 2017; Figure 4.4.a.). However, the results of this study show a strong positive correlation between elevation and eastings between 154°47'22.632"W, 67°57'40.428"N and 158°21'13.464"W,

67°51'20.124"N, reflecting the region's distinct terrain which exhibits an east-west gradient between warmer interior and cooler coastal sites (Kittel et al., 2011; Figure 4.b). Features are consequently suggested to form across the region in the observed pattern due to interactions between topography and climate (Leibman et al., 2003). 17% of the disturbance features are located within the West Coast climate division (western portion of study area) where modelled temperatures typically range from -2^{o} to 1^{o}C (Figure 4.10.a). This zone is more directly impacted by warm water influxes due to decreasing sea ice trends in the Arctic Ocean and higher sea surface temperatures in the North Pacific Ocean (Bieniek et al., 2012; Wendler et al., 2014; Sousanes and Hill, 2017). Records up to 2012 show that sea ice in the Chukchi Sea reduced at an annual rate of 16% over a ~35-year period (1979-2012) (Wendler et al., 2014). However, results from geomorphological change analysis across Site 3 within the West Coast division are highly varied between feature types (Figure 4.10.a). The rate of area change for ALDS was 2.5 times less than observed at Site 1, whereas for RTS area grew at a rate 4 times faster than that of Site 1.

A continental climate with comparatively lower annual precipitation likely controls the 83% of features located in the North Slope/Central Interior climate division (eastern portion of study area; Figure 4.10.a) (Bieniek et al., 2012). Modelled MAGT clearly define the North Slope Division as temperatures below -3^{o}C, but with greater distance inland, air temperatures experience higher seasonal variations (Mithan, 2018; Figure 4.10.a). Warmer winters and wetter summers are generally characteristic in the higher elevation mountainous parts of the eastern portion, such as Site 4 (Sousanes and Hill, 2017; Figure 4.10.a). However high summer precipitation is also typical of coastal sites of mid-elevation within the West Coast Division due to increased moisture availability reinforced by declining sea ice (Bieniek et al., 2012; Chapin et al., 2014; Sousanes and Hill, 2017). These varied patterns begin to explain why features can form across the region, since precipitation is a key trigger mechanism for thermokarst disturbance (Lamoureux and Lafreniere 2009).

Whilst changes in climate (temperature, precipitation, snowfall, and thawing degree days) are key for feature initiation, terrain factors such as aspect and slope become increasingly important for the degradation of individual features over time (Jones et al., 2019). A north facing aspect is important in

feature initiation as it acts in a similar way to latitude and limits the amount of solar radiation that surfaces receive (Lewkowicz and Harris, 2005b). In the absence of direct solar radiation, winter air temperatures become an important influence on ground surface temperatures (Salzmann et al., 2007). Of the 3291 features studied, ALDS were most likely to occur on north, followed by west slopes, whilst south facing slopes were most probable for RTS (Table 4.5). Whilst the insulation of permafrost may be greatest on north slopes, greater thaw is likely to occur on all remaining slope aspects due to air temperatures having a higher influence on ground thermal regimes (Mithan, 2018). Consequently, ALDS within this study demonstrated similar probability values across all aspects, suggesting additional driving factors of geomorphic sensitivity (Table 4.5).

For RTS, the aspect of solar radiation is particularly important for driving rates of headwall retreat through continued exposure and ablation of backwall ice (Lewkowicz, 1987; Khomutov et al., 2017). This study found that these features occur most on south slopes (P=0.331), corresponding with Jones et al (2019) where 58% of surveyed thaw slumps occurred on slopes of 180º to 270º. 78% of RTS in sites 1 and 2 occur on a slope range of 162º to 175º. However, features may be prevalent on all slopes in this study (Table 4.5) because aspect plays a most key role in initiation whereby once this has taken place, features can maintain active retreat on slopes of any aspect (Jones et al., 2019). Studies in Siberian Russia from 2012 to 2015 have shown that thaw slumps are likely to develop and enlarge faster on slopes which are south facing (Khomutov et al., 2017). Following this pattern, results from this study of two RTS on slopes of 167º and 168º show that between 2010 and 2017, features enlarged in area by 604.15 m^2/yr and 2126.55 m^2/yr (Figure 4.8.a).

Table 4.5: Probability of thermokarst features occurring at each aspect.

	ALDS	RTS
N	0.279	0.260
E	0.222	0.267
S	0.238	0.331
W	0.260	0.142

4.4.2. Local Geomorphology and Mechanisms of Thermokarst Disturbance Initiation and Evolution

In addition to regional climatic controls, local environments influence and are subsequently impacted by thermokarst disturbances. Local preconditions for the formation of these features can be suggested based on ArcticDEM findings. Bedrock geology is likely to play a role in the orientation of ALDS whereby they cluster on smooth upland hillslopes, in areas located between exposed unvegetated bedrock (Hamilton, 2009; Balser et al., 2015). Figure 4.11 highlights this, with 25 ALDS clustered in an ~7km^2 area, approximately 200m to 300m apart. Outcrops and underlying bedrock close to the surface will have an impact on the accumulation of thick ground-ice and the development of sufficient pore-water pressure due to being impermeable (Lacelle et al., 2010; Balser et al., 2015; Simpson et al., 2016). Where ALDS have been able to initiate and are abundant within Figure 4.11, thin soil deposits overlie near-surface bedrock and glacial drift (Balser et al., 2015). In contrast, RTS favour colluvial deposits where the soils and permafrost are deeper and more variable (Balser et al., 2015). The presence of these geological units allows these features to dominate the Brooks Range mountainous terrain (Balser et al., 2015).

As illustrated in Figure 4.11, ALDS often align with local topographic convexities (Mithan, 2018). Saturated soils between bedrock outcrops facilitate channelised flow over gentle slopes (Lamoureaux and Lafreniere, 2009). The presence of shallow channels where features have not been detected within this study may indicate areas where ALDS could ultimately develop or have previously been located (Figure 4.11). Where located along first-order streams, these drainage pathways produce turbid water as they move through disturbed soils which increases local river turbidity over the following 24 hours (Lamoureaux and Lafreniere, 2009; Mithan, 2018). During extreme summer warming in Cape Bounty in 2007, it was possible to attribute sediment delivery pulses to discharge from individual ALDS (Lamoureaux and Lafreniere, 2009).

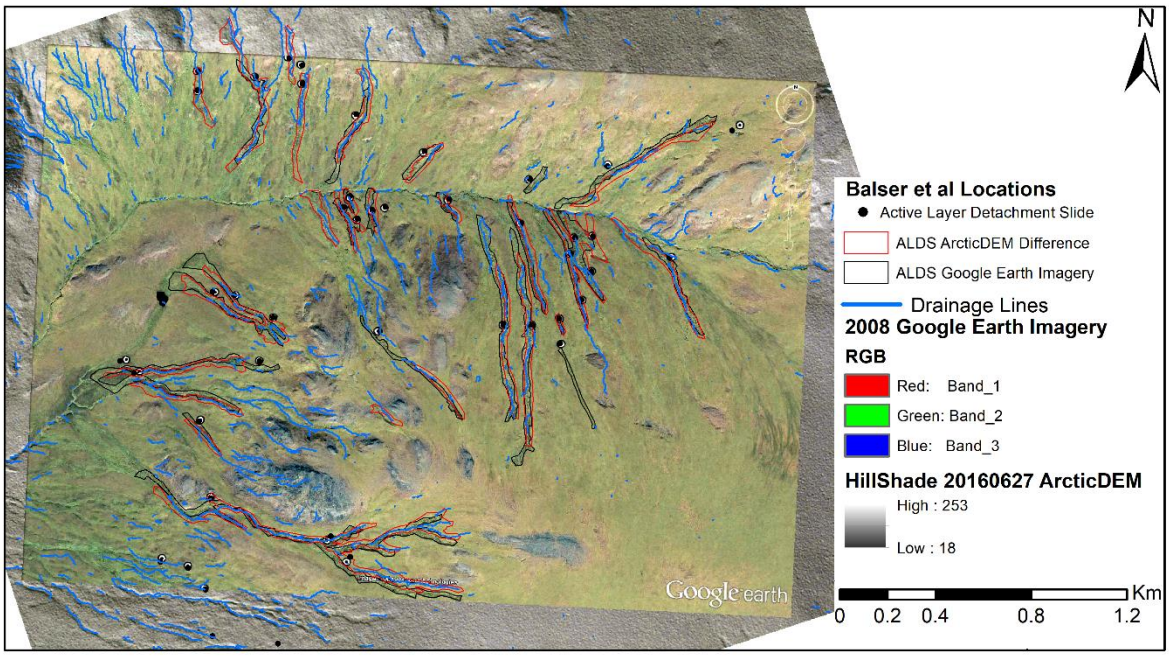

Figure 4.11: Drainage lines generated for 2016 ArcticDEM Imagery using ArcHydro. These are overlaid on mapped active layer detachment slides to show how features may linked to water routing through the landscape. ArcticDEM data provided by: Porter et al (2018); PGC (2020a).

4.4.3. Implications of Climatic and Topographic Interactions

The formation of thermokarst disturbances is directly reliant on summer climate and intense rainfall, which has been the trend within the Brooks Range over the last half a century (Balser et al., 2015; Lewkowicz and Way, 2019). At Bettles climate station, which represents the more continental features of the study (Figure 4.10.a), anomalous weather events of 2004 provided such trigger mechanisms for accelerated thaw front advance (Balser et al., 2015; Table 4.6).

Two significant weather events coincide with the data analysis period of this study. In 2012, the third wettest summer season on record was observed at Kotzebue station (Figure 4.10.a.) with a total of 20.4cm of rain falling (Sousanes and Hill, 2017). This station is representative of the more maritime locations in the West Coast region such as Site 3 (Table 4.7; Figure 4.6). Here, the rate of change in area for ALDS and RTS was observed as 3414.54 m^2/yr and 6844.97 m^2/yr. For RTS, the rate of increase in depth is more than twice that measured at Site 1. Whilst thaw depths only measured 50cm, this followed deeper recordings of 57cm in 2010 (Figure 4.10.b). More significantly, 2015-2016 was an unusually warm year for Alaska due to a strong El Niño and positive Pacific Decadal Oscillation which was recorded at Bettles station in the Central Interior (Sousanes

and Hill, 2017). Thaw depths reached 56cm in this year which were likely responsible for the 4 newly detected ALDS at Site 4 (Table 4.4) and average rate of change in area of 2161.42 m^2/yr (Figure 4.10.b).

One warm and wet summer season in the early stages of a RTS's existence can impact the trajectory of its evolution (Lewkowicz and Way, 2019). However, thaw slumps are slow to initiate, often developing from ALDS due to increased ground ice exposure (Cassidy et al., 2017). Therefore, coupled with their significant life span (up to half a century), this may explain why (1) rates of change in area at Site 1 are yet to be significantly impacted by the 2015-2016 warming event and (2) no new RTS have been identified within the study (Lewkowicz and Way, 2019). However, comparing 2016 temperatures and precipitation with those of 2004 (Table 4.6), it would be expected that more recent ArcticDEM data extending beyond the 2016/17 end point of this study would begin to more greatly reflect this weather event and show further increases in morphological parameters of current mapped features within Site 1. Given Bettles' location at the most easterly point of the study region (Figure 4.10.a), a continued trajectory of anomalous warming may result in feature initiation propagating further east. The potential for new feature formation corresponds with observations from Balser et al (2014) for the 2004 warm period which was responsible for the initiation of over three quarters of the studied features.

Table 4.6: Comparison of temperature and precipitation data measured at Bettles climate station in 2004 and 2016 (NOAA, 2016).

	April		**May**		**June**	
	2004	*2016*	*2004*	*2016*	*2004*	*2016*
Max. Temp. (ºC)	10.5	13.9	21.6	25.6	31.1	28.9
Max > 0°C (No. of days)	26	25	31	31	30	30
Total Precipitation (cm)	0.9	1.1	4.2	1.4	2.3	3.1

Table 4.7: Temperature and precipitation data measured at Kotzebue climate station data in 2012 (NOAA, 2016).

	July	August	September
Max. Temp. (°C)	21.7	20	12.8
Max > 0°C (No. of days)	31	31	30
Total Precipitation (cm)	8.8	11.1	5.2

4.4.4. Evaluation of Balser et al (2015) Thermokarst Inventory

The Balser et al (2015) database presents an inventory of thermokarst feature locations which provided this study with preliminary points of investigation. High-resolution ArcticDEM data has allowed work in this dynamic region to be improved upon by remotely detecting features and quantifying morphometric changes at sample sites of disturbance locations.

As ALDS continue to degrade, the permafrost exposed to thaw increases in depth (Schur and Jorgenson, 2007). Through ArcticDEM it is possible to begin to capture some of these changes through the calculation of depth to determine the new top of the active layer and volume to estimate material lost. How rapidly and extensively volumes of organic matter decompose and are redistributed via microbial activity has consequences for quantities of carbon release (Pautler et al., 2010). As headwall areas of RTS progressively retreat, the resultant area of bare soil may be determined by measuring difference in length relative to the width. The ability to analyse these morphometric parameters is important in the wider context because disturbance features, particularly “mega” slumps, are located near watersheds which they significantly influence as their activities increase in intensity (Kokelj et al., 2013). Near-surface thawing and associated local bank erosion results in a higher injection of sediment and increased turbidity of Arctic fluvial networks (Gooseff et al., 2009). Feature 2 in Figure 4.8.a is located on the bank of Feniak Lake and is therefore illustrative of potential localised impacts which can be quantified, with area changing at a rate of 2126.55 m^2/yr and volume by 52.77 m^3/yr.

4.5. Conclusion

Thermokarst features are abundant throughout the Brooks Range region, occurring over an elevation range of 600m to 900m and slopes of 4^{o} to 10^{o} (Section 4.3.1). This study has quantified their changing spatial geomorphometry at 4 sites using ArcticDEM from 2010 to 2017. Results showed that parameter changes were highly varied within and between feature types across the study region. Average rate of change in length and area was greater for ALDS than RTS, corresponding with their differing lifespans (Sections 4.3.5 and 4.3.6). 5 features were detected within ArcticDEM differencing which had not been previously detected by Balser et al (2015) (Table 4.4). Findings have been discussed in the context of climate divisions and west-east elevation patterns characteristic of the mountainous region (Section 4.4.1). Subsequently this has been linked with other aspects of the local terrain such as bedrock geology to provide explanations for where features are able to develop between exposed areas (Section 4.4.2). Extreme weather events with warmer air temperatures and increased precipitation have corresponded with reported geomorphological increases in 2012 and 2015-2016 (Section 4.4.3). Most importantly the analysis has highlighted that a diverse range of factors control thermokarst feature initiation, not all of which are able to be addressed here. Based on the differing initial sizes and magnitude of changes of individual features, it is likely that features have formed at different points within the time series. In order to pinpoint the exact year of initiation and the subsequent time at which features end their lifespan and become inactive, more frequent surveying would be required.

Chapter 5

Synthesis and Future Work

5.1. Overview

Permafrost degradation under a warming Arctic climate has increased the spatial extent and rate of expansion of periglacial landforms over recent decades (Lantz and Kokelj, 2008; Kokelj and Jorgenson, 2013). This has altered the geomorphological characteristics of High Arctic hillslopes with global environmental impacts on hydrological regimes and carbon fluxes (Gooseff et al., 2009; Kokelj et al., 2017). Studies have demonstrated the increasing importance of hillslope thermokarst, capturing processes such as IW cracking through in-situ measurements (Mackay, 1992; Burn and O'Neill, 2015) and mass failures through aerial photography (Balser et al 2014; Balser et al., 2015). However, remote sensing techniques are seldom the driving force of investigation, used more often as a validation tool. Indeed, few remote sensing studies sought to use elevation data to capture small-scale vertical changes, identify new sites of degradation and quantify geomorphometric changes. Using ArcticDEM, this thesis addressed knowledge gaps surrounding the geomorphic impacts of warming through: (i) quantifying elevation change across differing topographic regions and scales; (ii) assessing the spatiotemporal distribution and morphometric change of mass movements; and (iii) comparing findings with climate regimes (as per the objectives outlined in Chapter 1, Section 1.6). The research was divided into two main chapters. Chapter 3 used ArcticDEM data for Garry Island to develop an elevation differencing method which adjusted DEM biases and identified a control site. Chapter 4 applied and built upon the developed method to investigate the Alaskan Brooks Range, quantifying rates of change in feature size, shape, and areal extent. The following objectives were addressed:

5.1.1. Garry Island

The study of Garry Island allowed for a method of vertical change detection to be developed using a high-resolution dataset, which could be applied to similar hillslope thermokarst environments. The subsequent objectives were explored:

O1*: Quantify annual subsidence rates associated with geomorphic degradation using the 2-metre gridded ArcticDEM.*

ArcticDEM elevation differencing of Garry Island successfully identified topographic change attributable to thermokarst degradation. Between 2011 and 2017, vertical change of -0.03 m/yr was observed (Chapter 3, Section 3.3) which was equivalent to that measured within troughs in the western Arctic since 2006 (Burn, n.d). Fine-scale evolution of the polygonal networks, ubiquitous on hillslopes within the NWT, were at the limits of detection using ArcticDEM. Consequently, it was not possible to distinguish horizontal change between ridges and troughs, or high-centred and low-centred polygons. However, average reductions in elevation of 0.22 m/yr over the 6-year study period demonstrate the likelihood of continued subsidence and magnitude of future change (Chapter 3, Section 3.3). Seasonal changes further confirm this with 2.47m of subsidence between July and September 2016 likely being the most significant contribution to the 0.4 m/yr of change detected between September 2011 and 2016 (Chapter 3, Section 3.3.1)

O2*: Determine spatial coherence in patterns of elevation change by investigating trends at polygonal network sites.*

Field studies have determined that the north of the island (Site 1) is an area underlain by IWs (Burn, n.d). The results of elevation differencing within this study supported this, with negative vertical change of -0.08 m/yr (Chapter 3, Section 3.3.4.1). Particularly high rates of change were noted over the summer of 2016, aligning with increased rates of summer thawing. As wedge ice thaws at different rates and the overlying ground expands and contracts, material is transported between ridges and troughs (Burn and O'Neill, 2015). This variation within a polygon network was reflected by localised sub-regions of lower elevation positive change and higher elevation negative change which aids understanding of the extent of subsurface IWs.

***O3**: Compare (1) vegetation growth facilitated by water routing and (2) snow accumulation due to prevailing winds over topographic depressions, with patterns of positive elevation change.*

The results of elevation differencing between September 2016 and May 2017 produced positive vertical changes in the south of Garry Island (Chapter 3, Section 3.3.3). Multiple approaches were used to determine the cause of the identified changes. Sentinel 2 Imagery from June 2017 identified late-lying snowbanks accumulated in topographic depressions. Using a snowblow model these were found to be driven by northeasterly winds. Vegetation showed some correlation with these areas of snowblow, suggesting possible snow-vegetation interactions with vegetation trapping snow allowing for winter insulation (Chapter 3, Section 3.4.2). A hydrological analysis using Archydro showed that drainage pathways are located southward of these positive change bands, suggesting surface meltwater as their likely cause.

5.1.2. Alaska Brooks Range

The method developed for Garry Island was applied to hillslopes in the mountainous Brooks Range where large-scale elevation change was detected as a result of mass failures. Three objectives were investigated:

***O1**: Quantify statistical relationships between large-scale regional terrain properties, such as elevation, slope, and aspect, and thermokarst feature occurrence using the 100-metre gridded ArcticDEM.*

The 100-metre ArcticDEM was used to derive topographic parameters which confirmed that both ALDS and RTS form on slopes of 4^{o} to 10^{o} (Chapter 4, Section 4.3.1). ALDS form most frequently on north facing slopes at elevations of 600m to 900m, whilst RTS favour south facing slopes and occur at similar frequencies from 100m elevation up to ~1100m (Chapter 4, Section 4.3.1). This quantitative information may become invaluable in terms of predicting areas of terrain likely to be susceptible to future mass movement events. Regional climate divisions and extreme weather events exerted a significant control on east-west distribution which was proven through the investigation of temperature and precipitation data, thaw depths and MAGT which correlated with years of greater change.

***O2**: Determine small-scale morphometric characteristics of hillslope thermokarst feature types using the 2-metre gridded ArcticDEM.*

Previous work by Balser et al (2015) identified locations where ALDS and RTS occur using aerial photography. This study digitised features from high-resolution ArcticDEM Imagery, adding quantitative information to previous databases by providing length, width, depth, and areal extents and detecting new features (Chapter 4, Sections 4.3.5 and 4.3.6). A semi-automated process was developed which was able to derive approximate length and width parameters (Chapter 2, Section 2.5.2.2). Both length and width changes for ALDS were most significant at Site 1. Whereas RTS displayed the greatest rates of change in length at Site 3 and width at Site 2.

***O3**: Compare morphometric characteristics from Google Earth Imagery and ArcticDEM to identify rates of change in areal extent over time.*

The analysis of ArcticDEM data facilitated the calculation of the rates at which feature extents were changing due to thermokarst processes (Chapter 4, Section 4.3.6). For ALDS, rates of change in area were greatest at Site 1, whilst for RTS Site 3 showed the most significant increases. Comparing the two feature types across all 4 sites, the observed rates of area change in RTS were 38% lower than ALDS. This is likely attributable to their differing life spans, whereby ALDS are typically active for 5 to 10 years, whilst RTS have life spans of up to half a century and therefore take longer to reach maximum extent (refer to Chapter 1, Sections 1.4.3 and 1.4.4) (Swanson, 2014; Lewkowicz and Way, 2019). Calculating these rates of change allows for the estimation of organic carbon released across the study region (Table 5.2).

5.2. Pan-Arctic Implications

Over the next century, permafrost boundaries will advance ~100km north, as it is predicted that thawing will take place in up to one fifth of the current permafrost extent (ACIA, 2004; Bowden et al., 2008). These trends in warming air temperature have resulted in an increase in the frequency and intensity of thermokarst failure as the ground subsides (Gooseff et al., 2009). Estimates of carbon release associated with the observed topographic changes are subsequently discussed, addressing the project aim (in Chapter 1, Section 1.6).

5.2.1. Thermokarst Susceptible Terrain

The spatial distribution of landslide hazards has been assessed by scientists over the last two decades using susceptibility maps (Suzen and Doyuran, 2004). These are used to assess landslide hazards within GIS and remote sensing by determining the relative weighting of topographic, soil and geologic factors (Lee et al., 2004). Natural hazards have local and global significance in terms of erosion and landscape evolution (Guzzetti et al., 2005). Therefore, predicting where these hazards are likely to occur is important, not just within periglacial regions. Similar studies have sought to devise predictive models using feature inventory maps applied to a test area (Guzzetti et al., 2005). These models may subsequently be applicable to similar geological areas where feature characteristics have been captured (Guzzetti et al., 2005). This work can ultimately be applied to unknown regions in similar latitudes (Pachauri and Pant, 1992).

Using probability weighting techniques, this study derives a simplified susceptibility map for degradation of periglacial regions. Conditions under which thermokarst features form which were identified within this study can be used in order to broadly predict where: (1) features are present within the landscape but have not yet been studied; or (2) where features may form in the future. Elevation data from ArcticDEM and derived slope data have been used to produce a map of susceptibility for the Brooks Range region (Figure 5.1.a). This shows that 8.74% of terrain within the study region is likely to be vulnerable, with high values ($P>0.013$) distributed over MAGTs of $0^{o}C$ to $-6^{o}C$ (Figure 5.1.b). Spatially coherent patterns can be identified which, based on results from this study (Chapter 4, Section 4.3.4), may suggest that failures are clustered near waterbodies. The map highlights the possible number of features within the Brooks Range alone which remain unmapped, and unaccounted for in terms of their impacts on the wider system. Despite its simple form, the map demonstrates how the data could begin to be upscaled beyond the study region to pinpoint areas which could then form sites of further investigation.

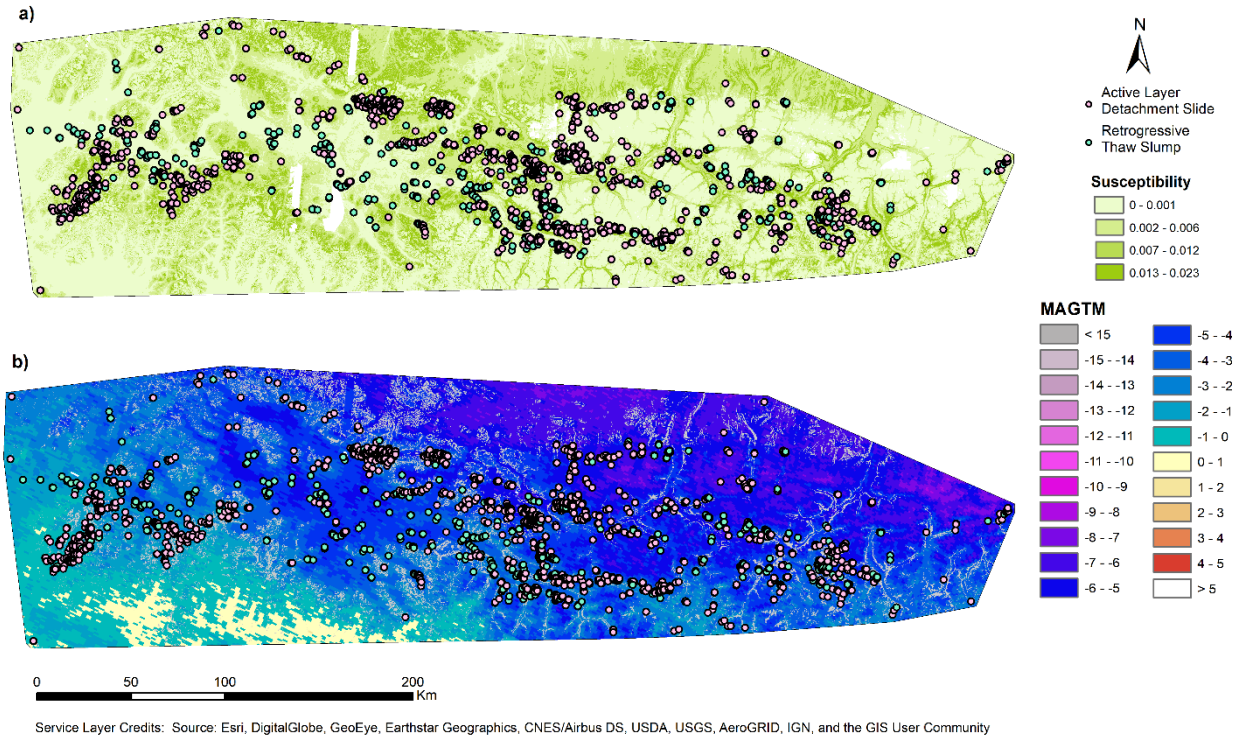

Figure 5.1: (a) Uses statistical distributions of elevation and slope data derived from ArcticDEM to predict susceptible terrain. This is based on elevations and slopes at which features are known to have occurred as mapped by Balser et al (2015). (b) High probabilities of P>0.013 are shown in white and overlaid onto mean annual ground temperatures which may further influence where features will form. ArcticDEM data provided by: Porter et al (2018); PGC (2020a).

5.2.2. Impacts on Carbon and Sediment Fluxes

Hillslope mass failures mobilise sediment during their active phases with impacts extending beyond the failure zone (Gooseff et al., 2009). Downslope mass wasting may subsequently erode channel networks and become suspended in previously clear river systems (Bowden et al., 2008; Turetsky et al., 2019). Within this study, volumetric changes calculated over the ArcticDEM difference period (2010 to 2017) at each failure site have allowed for estimations of sediment loss (Table 5.1). All sites experienced loss of volume which, except for Site 3, were greater than observed gains. Most notably all features in Site 2 experienced negative rates of volume change of -9206.82 m^3/yr. Volume lost at Site 1 is approximately comparable to the volume of soil displaced from a thermokarst feature monitored by Bowden et al (2008), which was calculated to transport sediment into the Toolik River covering 20km to 40km down to 1cm depths.

Table 5.1: Rates of change in volume calculated using mean difference in lowering within each ArcticDEM pair, multiplied by the change in surface area of each feature within each site.

Site number	% with negative volume changes	Avg. negative rate of volume change (m^3/yr)	% with positive volume changes	Avg. positive rate of volume change (m^3/yr)
Site 1	56%	-2770.56	44%	441.44
Site 2	100%	-9206.82	-	-
Site 3	8%	-361.09	92%	2146.75
Site 4	95%	-851.06	5%	1890.48

The collapse of frozen soils can destabilise a landscape over days to weeks, which has significant implications for Arctic infrastructure and communities (Turetsky et al., 2019). As permafrost thaws, abrupt ground collapse causes displacement of deep soil organic matter allowing organic carbon to be released due to microbial breakdown (Abbott and Jones, 2015; Turetsky et al., 2019). The spatiotemporal impacts of organic matter on biogeochemical cycles, once it has been exported off-site, are under monitored (Abbott et al., 2015; Abbott and Jones, 2015). Collapsing permafrost contains highly biodegradable dissolved organic carbons which often results in their mineralisation from freshwater into the atmosphere (Abbott et al., 2014). Where material is transported into aquatic ecosystems it can have significant short-term impacts such as carbon pulses and increased solute concentrations in Arctic catchments, often persisting for long enough to be transferred into marine ecosystems (Abbott et al., 2014; Abbott et al., 2015). Due to longer active phases, thaw slumps are likely to have greater impacts on surface water chemistry (Abbott et al., 2015).

Carbon storage within permafrost regions has been estimated at ~1300 Pg ± ~200 Pg and therefore modelling how much will be released is important for global warming (Hugelius et al., 2014). Abrupt thawing occurs in ~20% of frozen landscapes which is anticipated to release 60 to 100 billion tonnes of carbon by 2300 (Turetsky et al., 2019). Incorporating these estimates into carbon release projections will increase them by ~50% (Turetsky et al., 2019). However, quantities of carbon and nitrogen released from upland thermokarst morphologies are uncertain, varying by a factor of thirty (Abbott and Jones, 2015). These quantities differ based on the spatial density and geomorphological setting of features, and the duration of the active phase (Abbott et al., 2014). Furthermore, satellite detection of hillslope failures is limited and therefore carbon

released from these abrupt thaw processes are not represented in estimates of global SOC and associated climate models (Hugelius et al., 2013; Schuur et al., 2015; Turetsky et al., 2019).

Using areal changes calculated between 2010 and 2017 and data on organic carbon stocks it has been possible to approximate the quantity of carbon released at each failure site (Table 5.2). The method follows that of Abbott and Jones (2015) but uses it to calculate estimates for individual features. The results show that the region is subject to both carbon storage and release (Table 5.2). However, estimates are only an approximation since it does not account for the proportion of carbon that may be returned to the soil due to reuptake by plants (Turetsky et al., 2019). Research into both gradual and abrupt thawing of the Tibetan Plateau has shown that the rate at which permafrost carbon decomposes is dependent on the quality of the carbon and abundance of soil microbes (Wang et al., 2020). Under RCP4.5 and RCP8.5, carbon released from permafrost deeper than 3m was found to offset land carbon sinks by 2100 and is likely to reverse regions from carbon sinks to carbon sources under RCP8.5 (Wang et al., 2020).

Table 5.2: Average quantity of soil organic carbon displaced by features within each sub region of the four study sites. The area change within features was used as an approximation of the quantity of the organic layer removed. As per Abbott and Jones (2015) this was multiplied by the soil organic carbon content, taken from the National Circumpolar Soil Carbon Database version 2 (Hugelius et al., 2013).

Site Subsite Feature Type	Avg. Depth (m)	Avg. Area change (m^2)	Avg. SOCC_30 (kg/m^2)	Avg. SOCC_100 (kg/m^2)	Avg. SOCC_200 (kg/m^2)	Avg. SOCC_300 (kg/m^2)
1/1/ALDS	2.42E+00	1.20E+03	0.00E+00	0.00E+00	0.00E+00	0.00E+00
1/2/ALDS	1.24E+00	1.65E+04	1.14E+05	1.09E+06	2.08E+07	-
1/1/RTS	7.39E+00	4.08E+03	1.55E+04	8.83E+04	2.39E+06	5.84E+07
1/2/RTS	1.79E+00	1.63E+03	0.00E+00	0.00E+00	0.00E+00	-
2/1/RTS	2.53E+01	4.40E+03	1.67E+04	2.51E+04	1.19E+05	1.08E+05
2/2/RTS	8.61E+00	-1.62E+03	-6.16E+03	-9.24E+03	-4.38E+04	-3.97E+04
3/1/ALDS	1.88E+00	1.13E+03	3.62E+03	2.03E+04	2.18E+05	-
3/2/ALDS	2.44E+00	-3.40E+04	-1.84E+05	-9.93E+05	-2.61E+07	-6.55E+08
3/3/ALDS	7.00E-01	5.03E+02	1.61E+03	9.01E+03		-
3/1/RTS	2.38E+01	-1.37E+05	-7.42E+05	-5.34E+06	-1.13E+08	-2.18E+09
3/2/RTS	3.48E+00	-2.14E+03	-6.86E+03	-3.84E+04	-2.92E+05	-

Depths of the measured features within this study averaged 3m (Table 5.2) which is characteristic of Alaskan deep sediment deposits but was previously beyond measurable depths (Schuur et al., 2015). Storage of SOC extending to 3 metre depths has been estimated at a total of 1035 ± 150 Pg, with 34 ± 16 Pg C stored in thin sedimentary High Arctic soils (Hugelius et al., 2014). Soil organic carbon content (SOCC) covering 30cm to 300cm depths was obtained from the Northern Circumpolar Soil Carbon Database version 2 (NCSCDv2). This is a product of summed SOCC data from all soils and taxa (Hugelius et al., 2013).

5.3. Future Research Opportunities

This thesis has used the high-resolution ArcticDEM dataset in order to develop methods for detecting thermokarst changes. Chapter 3 used Garry Island to devise this method, which was validated through published field data. Chapter 4 demonstrated the success of applying the ArcticDEM differencing method to other regions of the Arctic, proving that the techniques were not site specific. Furthermore, it has demonstrated the ability to delineate the spatial extents of features, deriving areal and volumetric changes. Within this study, geomorphological mapping was automated to allow for frequent surveying of features. Repeating this process across the Arctic is possible using ArcticDEM and would increase the spatial extent of this data, allowing for greater understanding of rates of change in response to warming.

Future work could seek to automate more of the methodological process, incorporating DEM bias correction, control site selection and differencing techniques into a model which could pull ArcticDEM tiles for any Arctic location. This would allow for frequent collection of high-resolution data as a preliminary identification of change therefore increasing studies of hillslope thermokarst. Susceptibility maps such as that created within this study could be produced more Arctic wide using topographic parameters derived from ArcticDEM which could improve the generation of classification maps. The coverage of ArcticDEM would facilitate building upon previous hillslope classifications (e.g. Olefeldt et al., 2016) which do not cover marginal areas such as Garry Island.

More widely, there are opportunities to conduct further research of thermokarst environments. Measurements of thermokarst degradation are continually improved by advances in remote sensing techniques. For example,

high-resolution airborne optical imagery and satellite-based synthetic aperture radar have recently been applied to sources of atmospheric methane in Northern lakes (Engram et al., 2020). In High Arctic landscapes, differential interferometric synthetic aperture radar and ground-penetrating radar have been used to investigate ongoing land surface subsidence due to a relict ALDS (Paquette et al., 2020).

The availability and resolution of supporting datasets impacted the work conducted within this study and therefore means that conclusions drawn may still be underestimating the contribution of thermokarst failures to global carbon emissions. Whilst providing circumpolar coverage of permafrost carbon, the NCSCD is limited in its application due to the varying resolutions of the data used to derive individual pixels (Hugelius et al., 2013). Therefore, these pixels ultimately reflect a wider region surrounding each hillslope failure (Hugelius et al., 2013). This highlights the need to undertake greater research of periglacial landforms in order to improve spatial modelling.

Based on feature type, this chapter has estimated average amounts of SOC displaced by individual features. Estimating total carbon loss over the wider region of Alaska would be highly speculative without additional information. Sampling sites across the region, as undertaken within this study, would be required to quantify the number and type of features present, as well as their rates of areal change. This could be used to derive a susceptibility map for the wider region of Alaska, upscaling that of Figure 5.1. From this it would be possible to increase the extent of SOC losses estimated within this study.

5.4. Thesis Conclusion

This thesis has tested the ability of the high-resolution ArcticDEM dataset to detect periglacial landforms at varying spatial scales through elevation differencing. A method for correcting DEMs for bias was developed using Garry Island, Canada. Hillslope IWs were detected in the north of the island with similar subsidence rates to those measured in-situ in the NWT. However, the observed changes were at the limits of the ArcticDEM's vertical accuracy, with ridge-trough morphology difficult to distinguish. Factors such as hydrology and vegetation interact with local geomorphology and ground conditions to influence thermokarst initiation (Olefeldt et al., 2016). Hence multiple methods were applied to explain

observed positive elevation change on Garry Island. Snowbanks were the most likely cause, as evidenced by snowblow modelling. Networks of meltwater pathways indicates the hydrological impacts of increased rates of summer thaw.

The ArcticDEM differencing technique was subsequently applied to hillslope mass movement in the Brooks Range, Alaska where relief is higher and thermokarst features are of a greater magnitude. Topographic parameters were used to identify conditions under which the features formed on a broad spatial scale. Regional climate divisions were found to interact with these parameters to impact locations of initiation. Based on slope and elevation thresholds at which they are most likely to occur, a map was produced of areas which may be susceptible. Further work could reproduce this to identify vulnerable areas across the Arctic, dependant on warming of MAGTs. An automated mapping process was devised in order to quantify the changing geomorphometry of individual features. This process addressed knowledge gaps by adding quantitative information to existing databases. It was able to assess spatiotemporal changes, with different rates of change indicating different evolutionary stages from active to dormant features. Most notably, the method was able to detect new features which suggests that the area remains an active thermokarst region. Furthermore, this demonstrates that this method may be applied across the wider Arctic to remotely identify thermokarst features.

By the end of the century, the impacts of thawing permafrost could extend over 5.5×10^6 km^2 of the Arctic (Abbott and Jones, 2015). This has implications for monitoring the contributions of landform processes to: (1) hydrological cycles through the creation of hillslope water tracks which often restructure Arctic drainage networks; and (2) global carbon fluxes which are poorly understood within large-scale climate models (Rowland et al., 2010; Schuur et al., 2015). The study has highlighted that remote sensing of hillslope thermokarst features is limited, with studies previously being constrained to local-scale observations which often do not relate changes to wider processes (Rowland et al., 2010). Within this study, quantification of areal extents facilitated estimations of sediment fluxes, and volumetric changes allowed for approximations of SOCC. Using ArcticDEM has facilitated the collection of repeat data at high resolutions and employing these methods across the Arctic will provide invaluable contributions to climate models.

References

Abbott, B.W. and Jones, J.B., (2015). Permafrost collapse alters soil carbon stocks, respiration, CH 4, and N2O in upland tundra. *Global Change Biology*, *21* (12): 4570-4587.

Abbott, B.W., Jones, J.B., Godsey, S.E., Larouche, J.R. and Bowden, W.B., (2015). Patterns and persistence of hydrologic carbon and nutrient export from collapsing upland permafrost. *Biogeosciences Discussions*, *12* (3).

Abbott, B.W., Larouche, J.R., Jones Jr, J.B., Bowden, W.B. and Balser, A.W., (2014). Elevated dissolved organic carbon biodegradability from thawing and collapsing permafrost. *Journal of Geophysical Research: Biogeosciences*, *119* (10): 2049-2063.

Anisimov, O., Fitzharris, B., Hagen, J.O., Jefferies, R., Marchant, H., Nelson, F., Prowse, T. and Vaughan, D.G., (2001). Polar regions (arctic and antarctic). *Climate change*, 801-841.

Anisimov, O.A. and Nelson, F.E., (1997). Permafrost zonation and climate change in the northern hemisphere: results from transient general circulation models. *Climatic Change*, *35* (2): 241-258.

Anthony, K.W., von Deimling, T.S., Nitze, I., Frolking, S., Emond, A., Daanen, R., Anthony, P., Lindgren, P., Jones, B. and Grosse, G., (2018). 21st-century modeled permafrost carbon emissions accelerated by abrupt thaw beneath lakes. *Nature communications*, *9* (1): 1-11.

Arcone, S.A., Sellmann, P.V. and Delaney, A.J., (1982). *Radar detection of ice wedges in Alaska* (No. CRREL-82-43). COLD REGIONS RESEARCH AND ENGINEERING LAB HANOVER NH.

Assessment, A.C.I., (2004). Impacts of a warming Arctic-Arctic climate impact assessment. Impacts of a Warming Arctic-Arctic Climate Impact Assessment, by Arctic Climate Impact Assessment, pp. 144. ISBN 0521617782. Cambridge, UK: Cambridge University Press, December 2004: 144.

Balser, A., Gooseff, M.N., Jones, J. and Bowden, W.B., (2009). Thermokarst distribution and relationships to landscape characteristics in the Feniak Lake region Noatak National Preserve, Alaska; Final report to the National Park Service. *Arctic Network (ARCN) Rep., Fairbanks, AK*.

Balser, A.W., Gens, R., Mack, M. and Walker, D., (2015). *Retrogressive thaw slumps and active layer detachment slides in the Brooks Range and foothills of northern Alaska: terrain and timing*. University of Alaska Fairbanks.

Balser, A.W., Jones, J.B. and Gens, R., (2014). Timing of retrogressive thaw slump initiation in the Noatak Basin, northwest Alaska, USA. *Journal of Geophysical Research: Earth Surface*, *119* (5): 1106-1120.

Bieniek, P.A., Bhatt, U.S., Thoman, R.L., Angeloff, H., Partain, J., Papineau, J., Fritsch, F., Holloway, E., Walsh, J.E., Daly, C. and Shulski, M., (2012). Climate divisions for Alaska based on objective methods. *Journal of Applied Meteorology and Climatology*, *51* (7)1276-1289.

Black, R.F., (1982). Ice-wedge polygons of northern Alaska. In *Glacial geomorphology* (247-275). Springer, Dordrecht.

Bode, J.A., Moorman, B.J., Stevens, C.W. and Solomon, S.M., (2008), June. Estimation of ice wedge volume in the Big Lake area, Mackenzie Delta, NWT, Canada. In *Proceedings of the 9th International Conference on Permafrost, Fairbanks, Alaska* (Vol. 28: 131-136).

Bowden, W.B., (2010). Climate Change in the Arctic–Permafrost, Thermokarst, and Why They Matter to the Non-Arctic World. *Geography Compass*, *4* (10): 1553-1566.

Bowden, W.B., Gooseff, M.N., Balser, A., Green, A., Peterson, B.J. and Bradford, J., (2008). Sediment and nutrient delivery from thermokarst features in the foothills of the North Slope, Alaska: Potential impacts on headwater stream ecosystems. Journal of Geophysical Research: Biogeosciences, 113 (G2).

Bowden, W.B., Larouche, J.R., Pearce, A.R., Crosby, B.T., Krieger, K., Flinn, M.B., Kampman, J., Gooseff, M.N., Godsey, S.E., Jones, J.B. and Abbott, B.W., (2012). An integrated assessment of the influences of upland thermal-erosional features on landscape structure and function in the foothills of the Brooks Range, Alaska. In Proceedings of the Tenth International Conference on Permafrost (61-66).

Brown, J. and Romanovsky, V.E., (2008). Report from the International Permafrost Association: State of permafrost in the first decade of the 21st century. *Permafrost and Periglacial Processes*, *19*(2), pp.255-260.

Brown, R.J., (1970). *Permafrost in Canada: its influence on northern development*. University of Toronto Press.

Burn, C., (n.d.) Climate-induced thaw subsidence above ice wedges in sloping terrain, western Arctic Canada.

Burn, C.R. and Lewkowicz, A.G., (1990). Canadian landform examples-17 retrogressive thaw slumps. Canadian Geographer/Le Géographe canadien, 34 (3): 273-276.

Burn, C.R. and O'Neill, H.B., (2015). Subdivision of ice-wedge polygons, western Arctic coast. *Canadian Geotechnical Society, Quebec, QC*.

Burn, C.R., (2004). A field perspective on modelling 'single-ridge' ice-wedge polygons. *Permafrost and Periglacial Processes*, *15* (1): 59-65.

Callaghan, T.V. and Jonasson, S., (1995). Arctic terrestrial ecosystems and environmental change. *Philosophical Transactions of the Royal Society of London. Series A: Physical and Engineering Sciences*, *352* (1699): 259-276.

Callaghan, T.V., Johansson, M., Brown, R.D., Groisman, P.Y., Labba, N., Radionov, V., Bradley, R.S., Blangy, S., Bulygina, O.N., Christensen, T.R. and Colman, J.E., (2011). Multiple effects of changes in Arctic snow cover. *Ambio*, *40* (1): 32-45.

Candela, S.G., Howat, I., Noh, M.J., Porter, C.C. and Morin, P.J., (2017), December. ArcticDEM Validation and Accuracy Assessment. In *AGU Fall Meeting Abstracts*.

Cassidy, A.E., Christen, A. and Henry, G.H., (2017). Impacts of active retrogressive thaw slumps on vegetation, soil, and net ecosystem exchange of carbon dioxide in the Canadian High Arctic. *Arctic Science*, *3* (2): 179-202.

Chapin III, F.S., Trainor, S.F., Cochran, P., Huntington, H., Markon, C., McCammon, M., McGuire, A.D. and Serreze, M., (2014). Alaska. Climate Change Impacts in the United States: The Third National Climate Assessment.

Christiansen, H.H., Matsuoka, N. and Watanabe, T., (2016). Progress in understanding the dynamics, internal structure and palaeoenvironmental potential of ice wedges and sand wedges. *Permafrost and Periglacial Processes*, *27* (4): 365-376.

Circumpolar Active Layer Monitoring., (n.d). [online] Available at: <https://www2.gwu.edu/~calm/> [Accessed 9 May 2020].

Cory, R.M., Crump, B.C., Dobkowski, J.A. and Kling, G.W., (2013). Surface exposure to sunlight stimulates CO2 release from permafrost soil carbon in the Arctic. *Proceedings of the National Academy of Sciences*, *110* (9): 3429-3434.

de Klerk, P., Donner, N., Karpov, N.S., Minke, M. and Joosten, H., (2011). Short-term dynamics of a low-centred ice-wedge polygon near Chokurdakh (NE Yakutia, NE Siberia) and climate change during the last ca 1250 years. *Quaternary Science Reviews*, *30* (21-22): 3013-3031.

Dingman, S.L. and Koutz, F.R., (1974). Relations among vegetation, permafrost, and potential insolation in central Alaska. *Arctic and Alpine Research*, *6* (1): 37-47.

Douglas, M.S.V. and Smol, J.P., (2010). Freshwater diatoms as indicators of environmental change in the High Arctic. *The diatoms: applications for the environmental and earth sciences*, (Ed. 2), p.227.

Engram, M., Walter Anthony, K.M., Sachs, T., Kohnert, K., Serafimovich, A., Grosse, G. and Meyer, F.J., (2020). Remote sensing northern lake methane ebullition. *Nature Climate Change.*

Environment Canada., (2019). *Historical Data - Climate - Environment And Climate Change Canada*. [online] Available at: <https://climate.weather.gc.ca/historical_data/search_historic_data_e.html> [Accessed 2 May 2020].

Etzelmüller, B., (2000). On the quantification of surface changes using grid-based digital elevation models (DEMs). *Transactions in GIS*, *4* (2): 129-143.

European Space Agency. (2020). *Sentinel-2 - Missions - Sentinel Online*. [online] Available at: <https://sentinels.copernicus.eu/web/sentinel/missions/sentinel-2> [Accessed 2 May 2020].

Evans, I.S., (2012). Geomorphometry and landform mapping: What is a landform?. *Geomorphology*, *137* (1): 94-106.

Farquharson, L.M., Romanovsky, V.E., Cable, W.L., Walker, D.A., Kokelj, S.V. and Nicolsky, D., (2019). Climate change drives widespread and rapid thermokarst development in very cold permafrost in the Canadian High Arctic. *Geophysical Research Letters*, *46* (12): 6681-6689.

Fontana, F.M.A., Trishchenko, A.P., Luo, Y., Khlopenkov, K.V., Nussbaumer, S.U. and Wunderle, S., (2010). Perennial snow and ice variations (2000–2008) in the Arctic circumpolar land area from satellite observations. *Journal of Geophysical Research: Earth Surface*, *115* (F4).

Fortier, D., Allard, M. and Shur, Y., (2007). Observation of rapid drainage system development by thermal erosion of ice wedges on Bylot Island, Canadian Arctic Archipelago. *Permafrost and Periglacial Processes*, *18* (3): 229-243.

Fraczek, W., (2003). Mean sea level, GPS, and the geoid. *ArcUsers Online*.

Fraser, R.H., Kokelj, S.V., Lantz, T.C., McFarlane-Winchester, M., Olthof, I. and Lacelle, D., (2018). Climate sensitivity of high Arctic permafrost terrain demonstrated by widespread ice-wedge thermokarst on Banks Island. *Remote Sensing*, *10* (6): 954.

French, H.M. and Egginton, P., (1973), July. Thermokarst development, Banks Island, western Canadian Arctic. In *2nd International Conference on Permafrost* (Vol. 1: 203-212).

French, H.M., (2007). *The periglacial environment*. John Wiley & Sons.

Giles, D.P., Griffiths, J.S., Evans, D.J.A. and Murton, J.B., (2017). Geomorphological framework: glacial and periglacial sediments, structures and landforms. *Geological Society, London, Engineering Geology Special Publications*, *28* (1): 59-368.

Glennie, C., (2017). Arctic High-Resolution Elevation Models: Accuracy in Sloped and Vegetated Terrain. *Journal of Surveying Engineering*, *144* (1): 06017003.

Godin, E. and Fortier, D., (2012), June. Fine scale spatio-temporal monitoring of multiple thermo-erosion gullies development on Bylot Island, eastern canadian archipelago. In *Proceedings, Tenth International Conference on Permafrost (TICOP), Salekhard, Russia*.

Gooseff, M.N., Balser, A., Bowden, W.B. and Jones, J.B., (2009). Effects of hillslope thermokarst in northern Alaska. *Eos, Transactions American Geophysical Union*, *90* (4): 29-30.

Gooseff, M.N., Barrett, J.E. and Levy, J.S., (2013). Shallow groundwater systems in a polar desert, McMurdo Dry Valleys, Antarctica. *Hydrogeology Journal*, *21* (1): 171-183.

Government of the Northwest Territories. (2014). *13. Permafrost | Environment And Natural Resources*. [online] Available at: <https://www.enr.gov.nt.ca/en/state-environment/13-permafrost> [Accessed 2 May 2020].

Groendahl, L., Friborg, T. and Søgaard, H., (2007). Temperature and snow-melt controls on interannual variability in carbon exchange in the high Arctic. *Theoretical and Applied Climatology*, *88* (1-2): 111-125.

Grosse, G., Goetz, S., McGuire, A.D., Romanovsky, V.E. and Schuur, E.A., (2016). Changing permafrost in a warming world and feedbacks to the Earth system. *Environmental Research Letters*, *11* (4): 040201.

Grosse, G., Harden, J., Turetsky, M., McGuire, A.D., Camill, P., Tarnocai, C., Frolking, S., Schuur, E.A., Jorgenson, T., Marchenko, S. and Romanovsky, V., (2011). Vulnerability of high-latitude soil organic carbon in North America to disturbance. Journal of Geophysical Research: Biogeosciences, 116 (G4).

Guo, L., Ping, C.L. and Macdonald, R.W., (2007). Mobilization pathways of organic carbon from permafrost to arctic rivers in a changing climate. *Geophysical Research Letters*, *34* (13).

Guzzetti, F., Reichenbach, P., Cardinali, M., Galli, M. and Ardizzone, F., (2005). Probabilistic landslide hazard assessment at the basin scale. *Geomorphology*, *72* (1-4): 272-299.

Hall, D.K., (1982). A review of the utility of remote sensing in Alaskan permafrost studies. *IEEE Transactions on Geoscience and Remote Sensing*, (3): 390-394.

Hamilton, T.D., (2003). Surficial geology of the Dalton Highway (Itkillik-Sagavanirktok rivers) area, southern Arctic foothills, Alaska.

Hamilton, T.D., (2009). *Guide to surficial geology and river-bluff exposures, Noatak National Preserve, northwestern Alaska* (116). US Department, of the Interior, US Geological Survey.

Hannah, D.M., Gurnell, A.M. and McGregor, G.R., (1999). Interactions Between the Cryosphere, Climate and Greenhouse Gases.

Harris, C. and Lewkowicz, A.G., (1993). Form and internal structure of active-layer detachment slides, Fosheim Peninsula, Ellesmere Island, Northwest Territories, Canada. *Canadian Journal of Earth Sciences*, *30* (8): 1708-1714.

Harris, C., Smith, J.S., Davies, M.C. and Rea, B., (2008). An investigation of periglacial slope stability in relation to soil properties based on physical modelling in the geotechnical centrifuge. *Geomorphology*, *93* (3-4): 437-459.

Harry, D.G. and Gozdzik, J.S., (1988). Ice wedges: growth, thaw transformation, and palaeoenvironmental significance. *Journal of Quaternary Science*, *3* (1): 39-55.

Hill, P.R., Hequette, A., Ruz, M.H. and Jenner, K.A., (1990). Geological investigations of the Canadian Beaufort Sea coast. *Open File*, *2387:* 375.

Hinzman, L.D., Kane, D.L., Gieck, R.E. and Everett, K.R., (1991). Hydrologic and thermal properties of the active layer in the Alaskan Arctic. *Cold Regions Science and Technology*, *19* (2): 95-110.

Hobbie, S.E., Schimel, J.P., Trumbore, S.E. and Randerson, J.R., (2000). Controls over carbon storage and turnover in high-latitude soils. *Global Change Biology*, *6* (S1): 196-210.

Houghton, R.A., (2007). Balancing the global carbon budget. *Annu. Rev. Earth Planet. Sci.*, *35:* 313-347.

Hubbard, S.S., Gangodagamage, C., Dafflon, B., Wainwright, H., Peterson, J., Gusmeroli, A., Ulrich, C., Wu, Y., Wilson, C., Rowland, J. and Tweedie, C., (2013). Quantifying and relating land-surface and subsurface variability in permafrost environments using LiDAR and surface geophysical datasets. *Hydrogeology Journal*, *21* (1): 149-169.

Hugelius, G., Strauss, J., Zubrzycki, S., Harden, J.W., Schuur, E.A.G., Ping, C.L., Schirrmeister, L., Grosse, G., Michaelson, G.J., Koven, C.D. and O'Donnell, J.A., (2014). Estimated stocks of circumpolar permafrost carbon with quantified uncertainty ranges and identified data gaps. *Biogeosciences (Online)*, *11* (23).

Hugelius, G., Tarnocai, C., Broll, G., Canadell, J.G., Kuhry, P. and Swanson, D.K., (2013). The Northern Circumpolar Soil Carbon Database: spatially distributed datasets of soil coverage and soil carbon storage in the northern permafrost regions. *Earth System Science Data*, *5* (1): 3.

IPCC, (2013): Summary for Policymakers. In: Climate Change 2013: The Physical Science Basis. Contribution of Working Group I to the Fifth Assessment Report of the Intergovernmental Panel on Climate Change [Stocker, T.F., D. Qin, G.-K. Plattner, M. Tignor, S.K. Allen, J. Boschung, A. Nauels, Y. Xia, V. Bex and P.M. Midgley (eds.)]. Cambridge University Press, Cambridge, United Kingdom and New York, NY, USA.

Jenness, J.L., (1949). Permafrost in Canada. *Arctic*, *2* (1): 13-27.

Jolivel, M. and Allard, M., (2017). Impact of permafrost thaw on the turbidity regime of a subarctic river: the Sheldrake River, Nunavik, Quebec. *Arctic Science*, *3* (2): 451-474.

Jones, M.K.W., Pollard, W.H. and Jones, B.M., (2019). Rapid initialization of retrogressive thaw slumps in the Canadian high Arctic and their response to climate and terrain factors. *Environmental Research Letters*, *14* (5): 055006.

Jorgenson, M.T. and Grosse, G., (2016). Remote sensing of landscape change in permafrost regions. *Permafrost and periglacial processes*, *27* (4): 324-338.

Jorgenson, M.T. and Osterkamp, T.E., (2005). Response of boreal ecosystems to varying modes of permafrost degradation. *Canadian Journal of Forest Research*, *35* (9): 2100-2111.

Jorgenson, M.T., Shur, Y.L. and Pullman, E.R., (2006). Abrupt increase in permafrost degradation in Arctic Alaska. *Geophysical Research Letters*, *33* (2).

Kääb, A., (2008). Remote sensing of permafrost-related problems and hazards. *Permafrost and periglacial processes*, *19* (2): 107-136.

Kane, D.L., Hinzman, L.D. and Zarling, J.P., (1991). Thermal response of the active layer to climatic warming in a permafrost environment. *Cold Regions Science and Technology*, *19* (2): 111-122.

Kerfoot, D.E., (1969). *The geomorphology and permafrost conditions of Garry Island, NWT* (Doctoral dissertation, University of British Columbia).

Khomutov, A., Leibman, M., Dvornikov, Y., Gubarkov, A., Mullanurov, D. and Khairullin, R., (2017), May. Activation of cryogenic earth flows and formation of thermocirques on central yamal as a result of climate fluctuations. In *Workshop on World Landslide Forum* (209-216). Springer, Cham.

Kittel, T.G., Baker, B.B., Higgins, J.V. and Haney, J.C., (2011). Climate vulnerability of ecosystems and landscapes on Alaska's North Slope. *Regional Environmental Change*, *11* (1): 249-264.

Kokelj, S.V. and Burn, C.R., (2004). Tilt of spruce trees near ice wedges, Mackenzie Delta, Northwest Territories, Canada. *Arctic, Antarctic, and Alpine Research*, *36* (4): 615-623.

Kokelj, S.V. and Jorgenson, M.T., (2013). Advances in thermokarst research. *Permafrost and Periglacial Processes*, *24* (2): 108-119.

Kokelj, S.V., Lacelle, D., Lantz, T.C., Tunnicliffe, J., Malone, L., Clark, I.D. and Chin, K.S., (2013). Thawing of massive ground ice in mega slumps drives increases in stream sediment and solute flux across a range of watershed scales. *Journal of Geophysical Research: Earth Surface*, *118* (2): 681-692.

Kokelj, S.V., Lantz, T.C., Kanigan, J., Smith, S.L. and Coutts, R., (2009b). Origin and polycyclic behaviour of tundra thaw slumps, Mackenzie Delta region, Northwest Territories, Canada. *Permafrost and Periglacial Processes*, *20* (2): 173-184.

Kokelj, S.V., Lantz, T.C., Tunnicliffe, J., Segal, R. and Lacelle, D., (2017). Climate-driven thaw of permafrost preserved glacial landscapes, northwestern Canada. *Geology*, *45* (4): 371-374.

Kokelj, S.V., Lantz, T.C., Wolfe, S.A., Kanigan, J.C., Morse, P.D., Coutts, R., Molina-Giraldo, N. and Burn, C.R., (2014). Distribution and activity of ice wedges across the forest-tundra transition, western Arctic Canada. *Journal of Geophysical Research: Earth Surface*, *119* (9): 2032-2047.

Kokelj, S.V., Pisaric, M.F. and Burn, C.R., (2007). Cessation of ice-wedge development during the 20th century in spruce forests of eastern Mackenzie Delta, Northwest Territories, Canada. *Canadian Journal of Earth Sciences*, *44* (11): 1503-1515.

Kokelj, S.V., Tunnicliffe, J., Lacelle, D., Lantz, T.C., Chin, K.S. and Fraser, R., (2015). Increased precipitation drives mega slump development and destabilization of ice-rich permafrost terrain, northwestern Canada. *Global and Planetary Change*, *129:* 56-68.

Kokelj, S.V., Zajdlik, B. and Thompson, M.S., (2009a). The impacts of thawing permafrost on the chemistry of lakes across the subarctic boreal-tundra transition, Mackenzie Delta region, Canada. *Permafrost and Periglacial Processes*, *20* (2): 185-199.

Koven, C.D., Ringeval, B., Friedlingstein, P., Ciais, P., Cadule, P., Khvorostyanov, D., Krinner, G. and Tarnocai, C., (2011). Permafrost carbon-climate feedbacks accelerate global warming. *Proceedings of the National Academy of Sciences*, *108* (36): 14769-14774.

Kuhry, P., (2008). Palsa and peat plateau development in the Hudson Bay Lowlands, Canada: timing, pathways and causes. *Boreas*, *37* (2): 316-327.

Kupsch, W.O., (1962). Ice-thrust ridges in western Canada. *The Journal of Geology*, *70* (5): 582-594.

Lacelle, D., Bjornson, J. and Lauriol, B., (2010). Climatic and geomorphic factors affecting contemporary (1950–2004) activity of retrogressive thaw slumps on the Aklavik Plateau, Richardson Mountains, NWT, Canada. *Permafrost and Periglacial Processes*, *21* (1): 1-15.

Lachenbruch, A.H. and Marshall, B.V., (1986). Changing climate: geothermal evidence from permafrost in the Alaskan Arctic. Science, 234 (4777): 689-696.

Lachenbruch, A.H., (1962). *Mechanics of thermal contraction cracks and ice-wedge polygons in permafrost* (Vol. 70). Geological Society of America.

Lamoureux, S.F. and Lafrenière, M.J., (2009). Fluvial impact of extensive active layer detachments, Cape Bounty, Melville Island, Canada. *Arctic, Antarctic, and Alpine Research*, *41* (1): 59-68.

Lantuit, H. and Pollard, W.H., (2005). Temporal stereophotogrammetric analysis of retrogressive thaw slumps on Herschel Island, Yukon Territory.

Lantuit, H., Couture, N., Pollard, W.H., Haltigin, T., De Pascale, G. and Budkewitsch, P., (2005). Short-term evolution of coastal polycyclic retrogressive thaw slumps on Herschel Island, Yukon Territory. *Berichte zur Polarforschung*.

Lantuit, H., Pollard, W.H., Couture, N., Fritz, M., Schirrmeister, L., Meyer, H. and Hubberten, H.W., (2012). Modern and late Holocene retrogressive thaw slump activity on the Yukon coastal plain and Herschel Island, Yukon Territory, Canada. *Permafrost and Periglacial Processes*, *23* (1): 39-51.

Lantz, T.C. and Kokelj, S.V., (2008). Increasing rates of retrogressive thaw slump activity in the Mackenzie Delta region, NWT, Canada. Geophysical Research Letters, 35 (6).

Lawrence, D.M. and Slater, A.G., (2005). A projection of severe near-surface permafrost degradation during the 21st century. *Geophysical Research Letters*, *32* (24).

Lee, S., Choi, J. and Min, K., (2004). Probabilistic landslide hazard mapping using GIS and remote sensing data at Boun, Korea. *International Journal of Remote Sensing*, *25* (11): 2037-2052.

Leffingwell, E. de K. (1915). Ground-ice wedges; the dominant form of ground-ice on the north coast of Alaska. J OllYl/al ojGeology, *23* (7): 635- 54.

Leibman, M.O., Kizakov, A.I., Sulerzhitsky, L.D. and Zaretskaia, N.E., (2003), July. Dynamics of landslide slopes and their development on Yamal Peninsula. In *Permafrost. Proceedings of the 8th international conference on permafrost. Swets and Zeitlinger, Lisse* (651-656).

Lewkowicz, A.G. and French, H.M., (1982). The hydrology of small runoff plots in an area of continuous permafrost, Banks Island, NWT. In *Proceedings, 4th Canadian Permafrost Conf., Calgary* (151-162). Ottawa: NRC.

Lewkowicz, A.G. and Harris, C., (2005a). Morphology and geotechnique of active-layer detachment failures in discontinuous and continuous permafrost, northern Canada. *Geomorphology*, *69* (1-4): 275-297.

Lewkowicz, A.G. and Harris, C., (2005b). Frequency and magnitude of active-layer detachment failures in discontinuous and continuous permafrost, northern Canada. *Permafrost and Periglacial Processes*, *16* (1): 115-130.

Lewkowicz, A.G. and Way, R.G., (2019). Extremes of summer climate trigger thousands of thermokarst landslides in a High Arctic environment. *Nature communications*, *10* (1): 1-11.

Lewkowicz, A.G., (1987). Headwall retreat of ground-ice slumps, Banks Island, Northwest Territories. *Canadian Journal of Earth Sciences*, *24* (6): 1077-1085.

Lewkowicz, A.G., (1990), June. Morphology, frequency and magnitude of active-layer detachment slides, Fosheim Peninsula, Ellesmere Island, NWT. In *Proceedings of the 5th Canadian permafrost conference* (Vol. 54: 111-118).

Lewkowicz, A.G., (2007). Dynamics of active-layer detachment failures, Fosheim peninsula, Ellesmere Island, Nunavut, Canada. *Permafrost and Periglacial Processes*, *18* (1): 89-103.

Li, X. and Götze, H.J., (2001). Ellipsoid, geoid, gravity, geodesy, and geophysics. *Geophysics*, *66* (6): 1660-1668.

Liljedahl, A.K., Boike, J., Daanen, R.P., Fedorov, A.N., Frost, G.V., Grosse, G., Hinzman, L.D., Iijma, Y., Jorgenson, J.C., Matveyeva, N. and Necsoiu, M., (2016). Pan-Arctic ice-wedge degradation in warming permafrost and its influence on tundra hydrology. *Nature Geoscience*, *9* (4): 312-318.

Liljedahl, A.K., Hinzman, L.D. and Schulla, J., (2012), June. Ice-wedge polygon type controls low-gradient watershed-scale hydrology. In *Proceedings of the Tenth International Conference on Permafrost* (Vol. 1: 231-236). The Northern Publisher: Salekhard, Russia.

Liu, L., Schaefer, K.M., Chen, A.C., Gusmeroli, A., Zebker, H.A. and Zhang, T., (2015). Remote sensing measurements of thermokarst subsidence using InSAR. *Journal of Geophysical Research: Earth Surface*, *120* (9): 1935-1948.

Lyon, S.W., Destouni, G., Giesler, R., Humborg, C., Mörth, C.M., Seibert, J., Karlsson, J. and Troch, P.A., (2009). Estimation of permafrost thawing rates in a sub-arctic catchment using recession flow analysis. *Hydrology and Earth System Sciences*, *13* (5): 595-604.

Mackay, J., (2000). Thermally induced movements in ice-wedge polygons, western Arctic coast: a long-term study. *Géographie physique et Quaternaire*, *54* (1): 41-68.

Mackay, J.R. and Burn, C.R., (2002). The first 20 years (1978-1979 to 1998–1999) of ice-wedge growth at the Illisarvik experimental drained lake site, western Arctic coast, Canada. *Canadian Journal of Earth Sciences*, *39* (1): 95-111.

Mackay, J.R. and MacKay, D.K., (1974). Snow cover and ground temperatures, Garry Island, NWT. *Arctic*, *27* (4): 287-296.

Mackay, J.R., (1974). Ice-wedge cracks, Garry Island, Northwest Territories. *Canadian Journal of Earth Sciences*, *11* (10): 1366-1383.

Mackay, J.R., (1975). The closing of ice-wedge cracks in permafrost, Garry Island, Northwest Territories. *Canadian Journal of Earth Sciences*, *12* (9): 1668-1674.

Mackay, J.R., (1980). The origin of hummocks, western Arctic coast, Canada. *Canadian Journal of Earth Sciences*, *17* (8): 996-1006.

Mackay, J.R., (1981). Active layer slope movement in a continuous permafrost environment, Garry Island, Northwest Territories, Canada. *Canadian Journal of Earth Sciences*, *18* (11): 1666-1680.

Mackay, J.R., (1989). Ice-wedge cracks, western Arctic coast. *Canadian Geographer/Le Géographe canadien*, *33* (4): 365-368.

Mackay, J.R., (1990). Some observations on the growth and deformation of epigenetic, syngenetic and anti-syngenetic ice wedges. *Permafrost and Periglacial Processes*, *1* (1): 15-29.

Mackay, J.R., (1992). The frequency of ice-wedge cracking (1967–1987) at Garry Island, western Arctic coast, Canada. *Canadian Journal of Earth Sciences*, *29* (2): 236-248.

Mackay, J.R., (1995). Ice wedges on hillslopes and landform evolution in the late Quaternary, western Arctic coast, Canada. *Canadian Journal of Earth Sciences*, *32* (8): 1093-1105.

McRoberts, E.C. and Morgenstern, N.R., (1974). Stability of slopes in frozen soil, Mackenzie Valley, NWT. *Canadian geotechnical journal*, *11* (4): 554-573.

Merwade, V., (2012). Watershed and stream network delineation using ArcHydro Tools. *University of Purdue, School of Civil Engineering, Printed Lecture Note, USA*.

Metcalfe, D.B., Hermans, T.D., Ahlstrand, J., Becker, M., Berggren, M., Björk, R.G., Björkman, M.P., Blok, D., Chaudhary, N., Chisholm, C. and Classen, A.T., (2018). Patchy field sampling biases understanding of climate change impacts across the Arctic. *Nature ecology & evolution*, *2* (9): 1443-1448.

Miller, D. and Dixon, T.H., (2019). Evaluation of Permafrost Degradation in the North Slope Borough, Alaska, Using ArcticDEM as Time Series.

Mills, S.C., Le Brocq, A.M., Winter, K., Smith, M., Hillier, J., Ardakova, E., Boston, C.M., Sugden, D. and Woodward, J., (2019). Testing and application of a model for snow redistribution (Snow_Blow) in the Ellsworth Mountains, Antarctica. *Journal of Glaciology*, *65* (254): 957-970.

Mithan, H., (2018). *Quantifying the dynamic response of permafrost and slope stability to a changing climate* (Doctoral dissertation, Cardiff University).

Morgan, J.G., (1987). The north American datum of 1983. *The Leading Edge*, *6* (1): 27-33.

Morin, P., Porter, C., Cloutier, M., Howat, I., Noh, M.J., Willis, M., Bates, B., Willamson, C. and Peterman, K., (2016), April. ArcticDEM; a publically available, high resolution elevation model of the Arctic. In *EGU General Assembly Conference Abstracts* (Vol. 18).

Morse, P.D. and Burn, C.R., (2013). Field observations of syngenetic ice wedge polygons, outer Mackenzie Delta, western Arctic coast, Canada. *Journal of Geophysical Research: Earth Surface*, *118* (3): 1320-1332.

Morse, P.D., Burn, C.R. and Kokelj, S.V., (2012). Influence of snow on near-surface ground temperatures in upland and alluvial environments of the outer Mackenzie Delta, Northwest Territories. *Canadian Journal of Earth Sciences*, *49* (8): 895-913.

Murton, J.B., (2009). Global warming and thermokarst. In *Permafrost Soils* (185-203). Springer, Berlin, Heidelberg.

Natali, S.M., Schuur, E.A., Trucco, C., Hicks Pries, C.E., Crummer, K.G. and Baron Lopez, A.F., (2011). Effects of experimental warming of air, soil and permafrost on carbon balance in Alaskan tundra. *Global Change Biology*, *17* (3): 1394-1407.

National Oceanic and Atmospheric Administration (NOAA). (2016). National Centers for Environmental Information, NCDC IPS Climatological Data Alaska. Available at: https://www.ncdc.noaa.gov/IPS/cd/cd.html?_page=0&jsessionid=849FF6F60BE6B61CE5688F1246A34321&state=AK&_target1=Next+%3E [Accessed 28th March 2020]

Nitzbon, J., Langer, M., Westermann, S., Martin, L., Aas, K.S. and Boike, J., (2019). Pathways of ice-wedge degradation in polygonal tundra under different hydrological conditions. *The Cryosphere*, *13* (4): 1089-1123.

Nitze, I., Grosse, G., Jones, B.M., Romanovsky, V.E. and Boike, J., (2018). Remote sensing quantifies widespread abundance of permafrost region disturbances across the Arctic and Subarctic. Nature communications, 9 (1): 1-11.

Obu, J., Lantuit, H., Grosse, G., Günther, F., Sachs, T., Helm, V. and Fritz, M., (2017). Coastal erosion and mass wasting along the Canadian Beaufort Sea based on annual airborne LiDAR elevation data. *Geomorphology*, *293:* 331-346.

Obu, Jaroslav; Westermann, Sebastian; Kääb, Andreas; Bartsch, Annett (2018): Ground Temperature Map, 2000-2016, Northern Hemisphere Permafrost. Alfred Wegener Institute, Helmholtz Centre for Polar and Marine Research, Bremerhaven, PANGAEA, https://doi.org/10.1594/PANGAEA.888600

Olefeldt, D., Goswami, S., Grosse, G., Hayes, D., Hugelius, G., Kuhry, P., McGuire, A.D., Romanovsky, V.E., Sannel, A.B.K., Schuur, E.A.G. and Turetsky, M.R., (2016). Circumpolar distribution and carbon storage of thermokarst landscapes. *Nature communications*, *7* (1): 1-11.

Olefeldt, D., Goswami, S., Grosse, G., Hayes, D.J., Hugelius, G., Kuhry, P., McGuire, A.D., Romanovsky, V.E., Sannel, B., Schuur, E. and Turetsky, M.R., (2015), December. Thermokarst terrain: pan-Arctic distribution and soil carbon vulnerability. In *AGU Fall Meeting Abstracts*.

O'Loughlin, F., Paiva, R., Durand, M., Alsdorf, D. and Bates, P., (2015), April. Development of a'bare-earth'SRTM DEM product. In *EGU General Assembly Conference Abstracts* (Vol. 17).

Osterkamp, T.E., (2003), July. A thermal history of permafrost in Alaska. In Proceedings of the 8th International Conference on Permafrost (Vol. 2, pp. 863-868). AA Balkema Lisse, The Netherlands.

Osterkamp, T.E., (2005). The recent warming of permafrost in Alaska. Global and Planetary Change, 49 (3-4): 187-202.

Osterkamp, T.E., (2007). Characteristics of the recent warming of permafrost in Alaska. Journal of Geophysical Research: Earth Surface, 112 (F2).

Overland, J.E., Spillane, M.C., Percival, D.B., Wang, M. and Mofjeld, H.O., (2004). Seasonal and regional variation of pan-Arctic surface air temperature over the instrumental record. *Journal of Climate*, *17* (17): 3263-3282.

Overland, J.E., Wang, M., Walsh, J.E. and Stroeve, J.C., (2014). Future Arctic climate changes: Adaptation and mitigation time scales. *Earth's Future*, *2* (2): 68-74.

Pachauri, A.K. and Pant, M., (1992). Landslide hazard mapping based on geological attributes. *Engineering geology*, *32* (1-2): 81-100.

Paquette, M., Fortier, D. and Vincent, W.F., (2017). Water tracks in the High Arctic: a hydrological network dominated by rapid subsurface flow through patterned ground. *Arctic Science*, *3* (2): 334-353.

Paquette, M., Rudy, A.C., Fortier, D. and Lamoureux, S.F., (2020). Multi-scale site evaluation of a relict active layer detachment in a High Arctic landscape. *Geomorphology*: 107159.

Pastick, N.J., Jorgenson, M.T., Wylie, B.K., Nield, S.J., Johnson, K.D. and Finley, A.O., (2015). Distribution of near-surface permafrost in Alaska: Estimates of present and future conditions. *Remote Sensing of Environment*, *168*: 301-315.

Pautler, B.G., Simpson, A.J., Mcnally, D.J., Lamoureux, S.F. and Simpson, M.J., (2010). Arctic permafrost active layer detachments stimulate microbial activity and degradation of soil organic matter. *Environmental science & technology*, *44* (11): 4076-4082.

Peterson, R.A. and Krantz, W.B., (1998), June. A linear stability analysis for the inception of differential frost heave. In *Proceedings of the Seventh International Conference on Permafrost* (Vol. 883, p. 889).

Pike, R.J., (1988). The geometric signature: quantifying landslide-terrain types from digital elevation models. *Mathematical geology*, *20* (5): 491-511.

Polar Geospatial Center., (2020a). *Arcticdem – Polar Geospatial Center*. [online] Available at: <https://www.pgc.umn.edu/data/arcticdem/> [Accessed 2 May 2020].

Polar Geospatial Center., (2020b). *Introduction To Arcticdem – Polar Geospatial Center*. [online] Available at: <https://www.pgc.umn.edu/guides/arcticdem/introduction-to-arcticdem/> [Accessed 2 May 2020].

Polar Geospatial Center., (2020c). *Additional Information – Polar Geospatial Center*. [online] Available at: <https://www.pgc.umn.edu/guides/arcticdem/additional-information/> [Accessed 2 May 2020].

Pollard, W.H., (1990), June. The nature and origin of ground ice in the Herschel Island area, Yukon Territory. In *Proceedings, Fifth Canadian Permafrost Conference, Québec* (23-30).

Porter, Claire; Morin, Paul; Howat, Ian; Noh, Myoung-Jon; Bates, Brian; Peterman, Kenneth; Keesey, Scott; Schlenk, Matthew; Gardiner, Judith; Tomko, Karen; Willis, Michael; Kelleher, Cole; Cloutier, Michael; Husby, Eric; Foga, Steven; Nakamura, Hitomi; Platson, Melisa; Wethington, Michael, Jr.; Williamson, Cathleen; Bauer, Gregory; Enos, Jeremy; Arnold, Galen; Kramer, William; Becker, Peter; Doshi, Abhijit; D'Souza, Cristelle; Cummens, Pat; Laurier, Fabien; Bojesen, Mikkel, (2018), "ArcticDEM", https://doi.org/10.7910/DVN/OHHUKH, Harvard Dataverse, V1, [Accessed 2 May 2020].

Post, E., Alley, R.B., Christensen, T.R., Macias-Fauria, M., Forbes, B.C., Gooseff, M.N., Iler, A., Kerby, J.T., Laidre, K.L., Mann, M.E. and Olofsson, J., (2019). The polar regions in a 2° C warmer world. *Science Advances*, *5* (12), p.eaaw9883.

Potere, D., (2008). Horizontal positional accuracy of Google Earth's high-resolution imagery archive. *Sensors*, *8* (12): 7973-7981.

Purves, R.S., Mackaness, W.A. and Sugden, D.E., (1999). An approach to modelling the impact of snow drift on glaciation in the Cairngorm Mountains, Scotland. *Journal of Quaternary Science: Published for the Quaternary Research Association*, *14* (4): 313-321.

Ramage, J., (2018). *Impact of hillslope thermokarst on the nearshore carbon budget along the Yukon Coast, Canada* (Doctoral dissertation, University of Potsdam).

Riseborough, D., (2007). The effect of transient conditions on an equilibrium permafrost-climate model. *Permafrost and Periglacial Processes*, *18* (1): 21-32.

Rowland, J.C., Jones, C.E., Altmann, G., Bryan, R., Crosby, B.T., Hinzman, L.D., Kane, D.L., Lawrence, D.M., Mancino, A., Marsh, P. and McNamara, J.P., (2010). Arctic landscapes in transition: responses to thawing permafrost. *Eos, Transactions American Geophysical Union*, *91* (26): 229-230.

Rudy, A.C., Lamoureux, S.F., Treitz, P. and Van Ewijk, K.Y., (2016). Transferability of regional permafrost disturbance susceptibility modelling using generalized linear and generalized additive models. Geomorphology, 264: 95-108.

Salzmann, N., Nötzli, J., Hauck, C., Gruber, S., Hoelzle, M. and Haeberli, W., (2007). Ground surface temperature scenarios in complex high-mountain topography based on regional climate model results. *Journal of Geophysical Research: Earth Surface*, *112* (F2).

Schaefer, K., Lantuit, H., Romanovsky, V.E., Schuur, E.A. and Witt, R., (2014). The impact of the permafrost carbon feedback on global climate. Environmental Research Letters, 9 (8): 085003.

Schaefer, K., Zhang, T., Bruhwiler, L. and Barrett, A.P., (2011). Amount and timing of permafrost carbon release in response to climate warming. *Tellus B: Chemical and Physical Meteorology*, *63* (2): 168-180.

Schaphoff, S., Heyder, U., Ostberg, S., Gerten, D., Heinke, J. and Lucht, W., (2013). Contribution of permafrost soils to the global carbon budget. *Environmental Research Letters*, *8* (1): 014026.

Schutz, B.E., Zwally, H.J., Shuman, C.A., Hancock, D. and DiMarzio, J.P., (2005). Overview of the ICESat mission. *Geophysical Research Letters*, *32* (21).

Schuur, E.A., Bockheim, J., Canadell, J.G., Euskirchen, E., Field, C.B., Goryachkin, S.V., Hagemann, S., Kuhry, P., Lafleur, P.M., Lee, H. and Mazhitova, G., (2008). Vulnerability of permafrost carbon to climate change: Implications for the global carbon cycle. *BioScience*, *58* (8): 701-714.

Schuur, E.A., McGuire, A.D., Schädel, C., Grosse, G., Harden, J.W., Hayes, D.J., Hugelius, G., Koven, C.D., Kuhry, P., Lawrence, D.M. and Natali, S.M., (2015). Climate change and the permafrost carbon feedback. *Nature*, *520* (7546): 171-179.

Segal, R.A., Lantz, T.C. and Kokelj, S.V., (2016). Acceleration of thaw slump activity in glaciated landscapes of the Western Canadian Arctic. *Environmental Research Letters*, *11* (3): 034025.

Senneset, K., Phillips, M., Springman, S.M. and Arenson, L.U., (1988). *Permafrost:... International Conference, Proceedings* (Vol. 2). Tapir Publ..

Serreze, M.C., Barrett, A.P., Stroeve, J.C., Kindig, D.N. and Holland, M.M., (2009). The emergence of surface-based Arctic amplification. *The Cryosphere*, *3* (1): 11.

Shur, Y., Hinkel, K.M. and Nelson, F.E., (2005). The transient layer: implications for geocryology and climate-change science. *Permafrost and Periglacial Processes*, *16* (1): 5-17.

Shur, Y.L. and Jorgenson, M.T., (2007). Patterns of permafrost formation and degradation in relation to climate and ecosystems. Permafrost and Periglacial Processes, 18 (1): 7-19.

Siewert, M.B., Hanisch, J., Weiss, N., Kuhry, P., Maximov, T.C. and Hugelius, G., (2015). Comparing carbon storage of Siberian tundra and taiga permafrost ecosystems at very high spatial resolution. Journal of Geophysical Research: Biogeosciences, 120 (10): 1973-1994.

Simpson, J.M., Darrow, M.M., Huang, S.L., Daanen, R.P. and Hubbard, T.D., (2016). Investigating movement and characteristics of a frozen debris lobe, South-Central Brooks Range, Alaska. *Journal of Environmental & Engineering Geoscience*, *22* (3): 259-277.

Smith, M.W. and Riseborough, D.W., (2002). Climate and the limits of permafrost: a zonal analysis. *Permafrost and Periglacial Processes*, *13* (1): 1-15.

Smith, S.L., Burgess, M.M., Riseborough, D. and Mark Nixon, F., (2005). Recent trends from Canadian permafrost thermal monitoring network sites. *Permafrost and Periglacial Processes*, *16* (1): 19-30.

Sousanes, P. J., and K. Hill. (2017). Climate summary for the Arctic parks: Arctic Inventory and Monitoring Network. Natural Resource Report NPS/ARCN/NRR—2017/1574. National Park Service, Fort Collins, Colorado.

Steedman, A.E., Lantz, T.C. and Kokelj, S.V., (2017). Spatio-temporal variation in high-centre polygons and ice-wedge melt ponds, Tuktoyaktuk coastlands, Northwest Territories. *Permafrost and Periglacial Processes*, *28* (1): 66-78.

Streletskiy, D., Anisimov, O. and Vasiliev, A., (2015). Permafrost degradation. In *Snow and ice-related hazards, risks and disasters* (303-344). Academic Press.

Sturm, M., Schimel, J., Michaelson, G., Welker, J.M., Oberbauer, S.F., Liston, G.E., Fahnestock, J. and Romanovsky, V.E., (2005). Winter biological processes could help convert arctic tundra to shrubland. *Bioscience*, *55* (1): 17-26.

Süzen, M.L. and Doyuran, V., (2004). A comparison of the GIS based landslide susceptibility assessment methods: multivariate versus bivariate. *Environmental geology*, *45* (5): 665-679.

Swanson, D.K., (2012). Monitoring of retrogressive thaw slumps in the Arctic network, 2011: Three-dimensional modeling of landform change. *Natural Resource Report NPS/ARCN/NRDS—2012/247. National Park Service, Fort Collins, Colorado*, p.60.

Swanson, D.K., (2014). Mapping of erosion features related to thaw of permafrost in the NPS Arctic Inventory and Monitoring Network, Alaska. Natural Resource Data Series NPS/ARCN/NRDS–2010, 122.

Swanson, D.K., and Hill, K., (2010), Monitoring of Retrogressive Thaw Slumps in the Arctic Network, 2010 Baseline Data: Three-dimensional Modeling with Small-format Aerial Photographs, edited, p. 58, U.S. Department of the Interior, National Park Service, Natural Resource Data Series NPS/ARCN/NRDS—2010/123, Natural Resource Program Center, Fort Collins, CO.

Sweeney, J., Warner, N.H., Golombek, M.P., Kirk, R., Fergason, R.L., Pivarunas, A., Schwartz, C.H. and Hernandez, D.J., (2017), March. Constructing a semi-automated method in ArcMap to measure impact crater morphology. In *Lunar and Planetary Science Conference* (Vol. 48).

Tarnocai, C., Canadell, J.G., Schuur, E.A., Kuhry, P., Mazhitova, G. and Zimov, S., (2009). Soil organic carbon pools in the northern circumpolar permafrost region. Global Biogeochemical Cycles 23 (2)

Turetsky, M.R., Abbott, B.W., Jones, M.C., Anthony, K.W., Olefeldt, D., Schuur, E.A., Grosse, G., Kuhry, P., Hugelius, G., Koven, C. and Lawrence, D.M., (2020). Carbon release through abrupt permafrost thaw. *Nature Geoscience*, *13* (2): 138-143.

Turetsky, M.R., Abbott, B.W., Jones, M.C., Anthony, K.W., Olefeldt, D., Schuur, E.A., Koven, C., McGuire, A.D., Grosse, G., Kuhry, P. and Hugelius, G., (2019). Permafrost collapse is accelerating carbon release. *Nature*, *569* (7754): 32-35.

UNAVCO., (2019). *Geoid Height Calculator*. [online] Available at: <https://www.unavco.org/software/geodetic-utilities/geoid-height-calculator/geoid-height-calculator.html> [Accessed 2 May 2020].

USGS Earth Explorer., 2020. *Earthexplorer - Home*. [online] USGS Earth Explorer. Available at: <https://earthexplorer.usgs.gov/> [Accessed 2 May 2020].

Vincent, W.F., Lemay, M. and Allard, M., (2017). Arctic permafrost landscapes in transition: towards an integrated Earth system approach. *Arctic Science*, *3* (2): 39-64.

Vonk, J.E. and Gustafsson, Ö., (2013). Permafrost-carbon complexities. *Nature Geoscience*, *6* (9): 675-676.

Wahren, C.H., Walker, M.D. and Bret-Harte, M.S., (2005). Vegetation responses in Alaskan arctic tundra after 8 years of a summer warming and winter snow manipulation experiment. *Global Change Biology*, *11* (4): 537-552.

Walker, D.A., Gould, W.A., Maier, H.A. and Raynolds, M.K., (2002). The Circumpolar Arctic Vegetation Map: AVHRR-derived base maps, environmental controls, and integrated mapping procedures. *International Journal of Remote Sensing*, *23* (21): 4551-4570.

Walker, D.A., Raynolds, M.K., Daniëls, F.J., Einarsson, E., Elvebakk, A., Gould, W.A., Katenin, A.E., Kholod, S.S., Markon, C.J., Melnikov, E.S. and Moskalenko, N.G., (2005). The circumpolar Arctic vegetation map. *Journal of Vegetation Science*, *16* (3): 267-282.

Wang, T., Yang, D., Yang, Y., Piao, S., Li, X., Cheng, G. and Fu, B., (2020). Permafrost thawing puts the frozen carbon at risk over the Tibetan Plateau. *Science Advances*, *6* (19): p.eaaz3513.

Wendler, G., Ishikawa, N. and Streten, N., (1974). The climate of the McCall Glacier, Brooks Range, Alaska, in relation to its geographical setting. *Arctic and Alpine Research*, *6* (3): 307-318.

Wendler, G., Moore, B. and Galloway, K., (2014). Strong temperature increase and shrinking sea ice in Arctic Alaska. *The Open Atmospheric Science Journal*, *8* (1).

Westermann, S., Duguay, C.R., Grosse, G. and Kääb, A., (2015). Remote sensing of permafrost and frozen ground. In *Remote Sensing of the Cryosphere*, 307-344.

Williams, R., (2012). DEMs of difference. *Geomorphological Techniques*, *2* (3.2).

Wolfe, S.A., Nixon, F.M. and Kotler, E., (2000). Recent warming impacts in the Mackenzie Delta, Northwest Territories, and northern Yukon Territory coastal areas.

Woo, M.K. and Steer, P., (1982). Occurrence of surface flow on arctic slopes, southwestern Cornwallis Island. *Canadian Journal of Earth Sciences*, *19* (12): 2368-2377.

Woo, M.K. and Young, K.L., (2014). Disappearing semi-permanent snow in the High Arctic and its consequences. *Journal of Glaciology*, *60* (219): 192-200.

Wright, N., Quinton, W.L. and Hayashi, M., (2008). Hillslope runoff from an ice-cored peat plateau in a discontinuous permafrost basin, Northwest Territories, Canada. *Hydrological Processes: An International Journal*, *22* (15): 2816-2828.

Young, K.L., Assini, J., Abnizova, A. and Miller, E.A., (2013). Snowcover and melt characteristics of upland/lowland terrain: Polar Bear Pass, Bathurst Island, Nunavut, Canada. *Hydrology Research*, *44* (1): 2-20.

Zhang, T., Barry, R.G., Knowles, K., Heginbottom, J.A. and Brown, J., (1999). Statistics and characteristics of permafrost and ground-ice distribution in the Northern Hemisphere. *Polar Geography*, *23* (2): 132-154.

Zilkoski, D.B., D'Onofrio, J.D. and Frakes, S.J., (1997). Guidelines for establishing GPS-derived ellipsoid heights (Standards: 2 cm and 5 cm) version 4.3.

Zimov, S.A., Schuur, E.A. and Chapin III, F.S., (2006). Permafrost and the global carbon budget. *Science (Washington)*, *312* (5780): 1612-1613.

Appendices

Appendix A: ArcticDEM tiles used in the analysis of Garry Island in Chapter 3. Counts represent the proportion of Garry Island (69.4884° N, 135.7082° W) covered by each file. Strip files follow the naming convention: SENSOR_DATE_STEREOIMAGE1_STEREOIMAGE2_SEGMENT_RESOLUTION_VERSION_FILETYPE.

Strip ArcticDEM Files	Counts
SETSM_WV02_20110913_103001000DC88500_103001000D43A900_seg2_2m_v3.0_dem.tif	4656271
SETSM_WV02_20120623_10300100186B3300_1030010019746D00_seg2_2m_v3.0_dem.tif	4071329
SETSM_WV02_20121006_103001001CCAF200_103001001C073B00_seg3_2m_v3.0_dem.tif	4904985
SETSM_WV01_20130413_1020010021A80100_1020010020028100_seg1_2m_v3.0_dem.tif	4957220
SETSM_WV01_20131107_1020010028DA3600_1020010026455500_seg1_2m_v3.0_dem.tif	4882912
SETSM_WV02_20150307_103001003E2C4D00_103001003E5D9A00_seg1_2m_v3.0_dem.tif	4957220
SETSM_WV03_20150311_10400100085D0000_104001000927DC00_seg1_2m_v3.0_dem.tif	4957220
SETSM_WV01_20160714_1020010050A00300_102001005302E900_seg3_2m_v3.0_dem.tif	4789495
SETSM_WV01_20160909_10200100571BD500_1020010055E59E00_seg3_2m_v3.0_dem.tif	3806005
SETSM_WV03_20170516_104001002D200D00_104001002D365400_seg1_2m_v3.0_dem.tif	4035759

Appendix B: ArcticDEM tiles used in the analysis of the Alaskan Brooks Range in Chapter 4. Counts represent file coverage per subregion within each site. Strip files follow the naming convention:
SENSOR_DATE_STEREOIMAGE1_STEREOIMAGE2_SEGMENT_RESOLUTION_VERSION_FILETYPE

Site Subsite Feature	Strip ArcticDEM File 1	Counts	Strip ArcticDEM File 2	Counts	Latitude Longitude
1/1/RTS	SETSM_W1W1_20100630_102001000D5CF600_102001000E9E4700_seg1_2m_v3.0_dem.tif	106134	SETSM_WV01_20170502_1020010062589E00_102001005E0F4600_seg1_2m_v3.0_dem.tif	208570	68º13’54’’N 158º20’15’’W
1/2/RTS	SETSM_WV02_20131002_10300100278DDA00_1030010027C3A200_seg1_2m_v3.0_dem.tif	136012	SETSM_WV02_20161002_103001005D02DE00_103001005BC76D00_seg7_2m_v3.0_dem.tif	191679	68º16’24’’N 157º53’01’’W
1/1/ALDS	SETSM_WV02_20130525_10300100233B3E00_10300100023A3B800_seg3_2m_v3.0_dem.tif	190707	SETSM_WV02_20161002_103001005D02DE00_103001005BC76D00_seg7_2m_v3.0_dem.tif	230650	68º18’57’’N 157º55’39’’W
1/2/ALDS	SETSM_WV03_20150413_104001000AB45800_104001000A4E2C00_seg1_2m_v3.0_dem.tif	779256	SETSM_WV01_20170502_1020010062589E00_102001005E0F4600_seg1_2m_v3.0_dem.tif	779256	68º14’39’’N 158º06’07’’W
2/1/RTS	SETSM_WV01_20150424_102001003CBD7A00_102001003D825100_seg1_2m_v3.0_dem.tif	70067	SETSM_WV01_20170502_1020010062589E00_102001005E0F4600_seg1_2m_v3.0_dem.tif	70067	68º05’16’’N 158º38’22’’W
2/2/RTS	SETSM_WV02_20150622_10300100444E4000_103001004438F000_seg5_2m_v3.0_dem.tif	728691	SETSM_WV02_20161024_103001005E885400_103001005D8BEC00_seg1_2m_v3.0_dem.tif	180238	67º58’18’’N 158º30’57’’W
3/1/ALDS	SETSM_W1W1_20100704_102001000D022300_102001000D8D8A00_seg2_2m_v3.0_dem.tif	828896	SETSM_WV03_20170512_104001002D679F00_104001002C672000_seg1_2m_v3.0_dem.tif	828896	67º55’31’’N 161º25’31’’W
3/2/ALDS	SETSM_WV01_20130620_1020010022BA9500_1020010021B94400_seg1_2m_v3.0_dem.tif	1328950	SETSM_WV02_20161026_103001005C4C7C00_103001005D9C7700_seg7_2m_v3.0_dem.tif	1292017	67º35’18’’N 161º43’43’’W
3/3/ALDS	SETSM_WV01_20130831_1020010023E6C100_10200100251F2300_seg1_2m_v3.0_dem.tif	317291	SETSM_WV03_20170512_104001002D679F00_104001002C672000_seg1_2m_v3.0_dem.tif	244414	67º52’06’’N 161º14’34’’W
3/1/RTS	SETSM_WV01_20130831_1020010023E6C100_10200100251F2300_seg1_2m_v3.0_dem.tif	1280014	SETSM_WV01_20170419_1020010060AF2400_1020010060EA6D00_seg1_2m_v3.0_dem.tif	1383308	67º56’50’’N 161º05’28’’W
3/2/RTS	SETSM_WV01_20130620_1020010022BA9500_1020010021B94400_seg1_2m_v3.0_dem.tif	177718	SETSM_WV03_20161026_10400100239A3E00_10400100231BF300_seg4_2m_v3.0_dem.tif	181902	67º33’41’’N 161º46’23’’W
3/3/RTS	SETSM_WV01_20130619_10200100235E1700_102001002015700_seg1_2m_v3.0_dem.tif	529831	SETSM_WV01_20170307_102001005E864400_102001005E89EE00_seg1_2m_v3.0_dem.tif	529831	67º44’06’’N 161º18’52’’W
4/1/ALDS	SETSM_W1W1_20100920_102001000F31A300_102001000FE86200_seg1_2m_v3.0_dem.tif	1175850	SETSM_WV03_20160627_104001001E441B00_104001001E732D00_seg1_2m_v3.0_dem.tif	1197528	68º02’34’’N 155º58’26’’W
	SETSM_W1W1_20100920_102001000F31A300_102001000FE86200_seg1_2m_v3.0_dem.tif	3237598	SETSM_WV03_20160627_104001001E441B00_104001001E732D00_seg1_2m_v3.0_dem.tif	3237598	68º00’57’’N 155º51’10’’W
4/3/ALDS	SETSM_WV01_20120208_10200100187DD800_1020010019E55000_seg1_2m_v3.0_dem.tif	349569	SETSM_WV02_20170319_1030010067347900_1030010068B10600_seg1_2m_v3.0_dem.tif	349569	67º50’48’’N 155º45’33’’W